

A NUCLEAR SQUEEZE: THE ROLE OF THE NUCLEUS IN CONFINED  
CANCER CELL MIGRATION

A Dissertation

Presented to the Faculty of the Graduate School  
of Cornell University

In Partial Fulfillment of the Requirements for the Degree of  
Doctor of Philosophy in Biomedical Engineering

by

Alexandra Lynn McGregor

December 2018

© 2018 Alexandra Lynn McGregor

A NUCLEAR SQUEEZE: THE ROLE OF THE NUCLEUS IN CONFINED  
CANCER CELL MIGRATION

Alexandra Lynn McGregor, Ph.D.

Cornell University 2018

Metastasis is the leading cause of breast cancer deaths worldwide. During cancer metastasis, cells must squeeze through small spaces in the basement membrane, interstitium, and endothelium. A major determinant of a cell's ability to squeeze through confined spaces is nuclear stiffness, which is governed by lamin expression and chromatin condensation. Although the cell cytoplasm is able to squeeze through submicron obstacles, the cell nucleus has difficulty passing through pore sizes smaller than 5-10  $\mu\text{m}$ . As the largest and stiffest organelle in the cell, the nucleus is a rate-limiting step in cell migration.

To better understand the role the nucleus plays in confined migration, we used microfluidic devices with constrictions similar in size to interstitial spaces. We first examined whether lamin A/C expression correlates with increased metastatic potential using a large panel of human and mouse breast cancer cell lines. Highly metastatic cancer cell lines had significantly lower levels of lamins A and C than less aggressive cancer cell lines and normal breast epithelial cells, and they were more successful at

squeezing through confined microenvironments. This finding suggests that the expression of lamin A/C may play a role in cells' ability to metastasize.

Our results also showed that tight spaces pose a substantial mechanical challenge to the integrity of the nucleus, often resulting in a transient loss of nuclear envelope (NE) integrity—NE rupture. During NE rupture, a temporary exchange of nuclear and cytoplasmic content occurs. The consequences of nuclear deformation and NE rupture include nuclear fragmentation, chromatin herniation, organelle displacement, and DNA damage. To study whether NE rupture is related to metastatic potential, we created an analysis program to automate the detection and recording of NE rupture events *in vitro*. Using a panel of breast cancer cell lines, we found that NE rupture rate and duration are independent of metastatic potential. Although the incidence and duration of NE rupture did not vary between cell lines, long-term selection studies using isogenic clonal cell lines indicated that the effect of NE rupture might vary between individual clones from the same parent population.

This thesis investigates the role of the NE during confined cell migration and the downstream consequences of NE rupture. We postulate that nuclear deformation and rupture during confined cell migration could promote metastatic progression in cancer cells through the accumulation genomic alterations, including DNA damage, aneuploidy, and genomic rearrangements. Confined migration may represent a novel mechanism by which the physical properties of cells and tissues contribute to breast cancer progression.

## BIOGRAPHICAL SKETCH

Alexandra McGregor was born in Pontiac, Michigan. She graduated from Waterford Kettering High School and attended Rensselaer Polytechnic Institute, where she graduated Summa Cum Laude with bachelor's degrees in both biomedical engineering and biology. As an undergraduate, Alex was a member of Dr. Deanna Thompson's lab and the Cancer Cell Biology group, which was led by George Edick. Alex spent two summers and a winter break working at Janelia Research Campus in the laboratories of Drs. Louis Scheffer and Vivek Jayarman. During this time, Alex became interested in bridging engineering and biology, and she decided to pursue a graduate degree in biomedical engineering at Cornell University.

At Cornell, Alex joined the Physical Sciences in Oncology Center while working with Dr. Cynthia Reinhart-King's lab. In her third year, Alex began a project with Dr. Jan Lammerding, who became her primary research advisor. Dr. Lammerding's lab was the perfect environment for Alex, as Dr. Lammerding was dually appointed in both the Weill Institute for Cell and Molecular Biology and the Meinig School of Biomedical Engineering. Throughout her PhD, Alex was a leader in a partnership with the Cancer Center of the Finger Lakes. Alex plans to continue bridging her engineering and biology background to study cancer in the future.

## ACKNOWLEDGEMENTS

I would like to thank my advisor, Dr. Jan Lammerding, for his steadfast support throughout my time at Cornell. I am grateful for the opportunity to be in a lab that truly brings together engineering and biology at the forefront of cancer research. I also acknowledge my committee members, Dr. Matthew Paszek and Dr. Robert Weiss, for their generous support and advice throughout my PhD.

My family, friends, and community provided the love and encouragement that allowed me to reach this incredible milestone. I am profoundly thankful for the unwavering support of my parents Robin and Rudie, my sister Elizabeth, my partner Peter, and my best friend Riley. Their unconditional support got me through many long-nights, weekends, and holidays in lab.

I am grateful to all former and current members of the Lammerding lab, including Dr. Emily Bell, Frank Chang, Dr. Patricia Davidson, Dr. Celine Denais, Ashley Earle, Dr. Gregory Fedorchak, Rachel Gilbert, Jeremiah Hsia, Philipp Isermann, Dr. Laith Kadem, Jeremy Keys, Dr. Tyler Kirby, Joseph Long, Melanie Maurer, Pragya Shah, Aaron Windsor, and Dr. Noam Zuela-Sopilniak. The atmosphere in our lab was amazing, and I already miss coming to work every day.

I am incredibly thankful to have mentored three stellar undergraduate students: Joshua Elacqua, Jay Jun, and Jerry Sarubbe. My three very tall, J-named undergraduates helped my project flourish. I am particularly thankful for both Josh and Jerry, who really came through during the

most trying times of my graduate school experience. Wherever they go in life, they will do amazing things. I am glad that they were part of my time at Cornell.

Countless members of the Cancer Resource Center and the patient-researcher partnership have supported me on this journey. Special thanks to Peter DelNero, Jason Hungerford, Bob Riter, and Bob Weiss for being incredible teammates in the development of our partnership. The members of the Young Adult Support Group became like a family to me, including Beth Brunelle, Kristina and Allan Burke, Lael Eisman, Julia Gil, Adam Goodwin, Jason Hungerford, John Hohm, Cheryl Jewell, Daryl Pace, Megan and John Pillar, Megan Russo, Shiv Shah, Monica Vakiner, Abby Van Wassen, and Emily Virkler. I would also like to acknowledge Laura Austen, Jackie Creque, Rosemary Lang, Fran Manzella, Sharon Nelson, Janet and David Pierce, Sarah Ross, Jackie Wakula, and Rociio Zepp. Your love, support, and confidence in me means the world.

My success at Cornell was influenced by my wonderful mentors and colleagues from Rensselaer Polytechnic Institute, Janelia Research Campus, and Waterford Kettering High School. The people who helped me begin my training in science and engineering include Mr. George Edick, Mr. Frenkel, Kristen Jakobowski, Dr. Vivek Jayarman, Dr. Eric Ledet, Mr. Nicholson, Dr. Krista Parran, Dr. George Plopper, Dr. Louis Scheffer, Mr. Scheutz, Dr. Deanna Thompson, and Dr. Angela Welch. Your unwavering support in my abilities pushed me to new heights.

Lastly, I would like to thank all my funding sources during my time at Cornell: the Douglas fellowship, the National Science Foundation GRFP fellowship (DGE-1144153), the CTSC TL1

Translational Medicine Fellowship (UL1-TR000457). I also acknowledge my advisor's funding sources that contributed to my work: NIH (R01 HL082792 and R01 NS059348); Department of Defense Breast Cancer Research Program (BC102152 and BC150580); NSF (CBET-1254846); National Cancer Institute through the Cornell Center on the Microenvironment and Metastasis (U54 CA143876). Without the support of these fellowships and grants, I would not have been able to perform this important work.

“Science and everyday life cannot and should not be separated.” –Rosalind Franklin

This dissertation is dedicated to every person that has helped me through the long,  
winding road that is a Ph.D.

## TABLE OF CONTENTS

BIOGRAPHICAL SKETCH.....	iii
ACKNOWLEDGEMENTS .....	iv
CHAPTER 1: INTRODUCTION.....	1
CHAPTER 2: CHARACTERIZATION OF NUCLEAR ENVELOPE RUPTURE IN 3-D CONFINED CELL MIGRATION .....	14
CHAPTER 3: THE DEVELOPMENT OF TOOLS TO STUDY CELL MIGRATION, AND THE ROLE OF THE NUCLEUS IN CELL MIGRATION .....	29
CHAPTER 4: THE ROLE OF LAMIN A/C IN CONFINED CANCER CELL MIGRATION AND BREAST CANCER PROGRESSION.....	51
CHAPTER 5: THE ROLE OF NUCLEAR ENVELOPE RUPTURE IN BREAST CANCER PROGRESSION .....	85
CHAPTER 6: LONG-TERM CONSEQUENCES OF CONFINED CELL MIGRATION ON THE CANCER CELL GENOME .....	107
CHAPTER 7: FROM PATIENTS TO PARTNERS: THE DEVELOPMENT OF A PARTNERSHIP BETWEEN CANCER SURVIVORS AND CANCER SCIENTISTS .....	143
BIBLIOGRAPHY .....	146
APPENDIX .....	162

## CHAPTER 1: INTRODUCTION<sup>1</sup>

### **Abstract**

From embryonic development to cancer metastasis, cell migration plays a central role in health and disease. It is increasingly becoming apparent that cells migrating in three-dimensional (3-D) environments exhibit some striking differences compared with their well-established 2-D counterparts. One key finding is the significant role the nucleus plays during 3-D migration: when cells move in confined spaces, the cell body and nucleus must deform to squeeze through available spaces, and the deformability of the large and relatively rigid nucleus can become rate-limiting. In this review, we highlight recent findings regarding the role of nuclear mechanics in 3-D migration, including factors that govern nuclear deformability, and emerging mechanisms by which cells apply cytoskeletal forces to the nucleus to facilitate nuclear translocation. Intriguingly, the ‘physical barrier’ imposed by the nucleus also impacts cytoplasmic dynamics that affect cell migration and signaling, and changes in nuclear structure resulting from the mechanical forces acting on the nucleus during 3-D migration could further alter cellular function. These findings have broad relevance to the migration of both normal and cancerous cells inside living tissues, and motivate further research into the molecular details by which cells move their nuclei, as well as the consequences of the mechanical stress on the nucleus.

---

<sup>1</sup> Portions of this work have been included in the following publication:

McGregor, A.L. †, Hsia, C. †, Lammerding, J. (2016). Squish and squeeze – the nucleus as a physical barrier during migration in confining environments, *Current Opinion in Cell Biology* 40, 32-40. †, authors contributed equally.

## Introduction

In multicellular organisms, cell migration is essential in the development, maintenance and repair of various tissues (Munjal and Lecuit 2014); it also enables immune cells to survey tissues and to respond to local challenges (Weninger et al. 2014). At the same time, cell migration drives the tissue invasion and metastasis of cancer cells, which is responsible for the vast majority of cancer deaths (Chaffer and Weinberg 2011). While much of our current knowledge regarding the molecular and biophysical principles of cell migration stems from studying cells moving on 2-D substrates (Gardel et al. 2010), it is now becoming evident that cells migrating in 3-D environments encounter distinct physical challenges. During *in vivo* migration/invasion, cells must navigate many microstructural obstacles, including extracellular matrix (ECM) networks and neighboring cells. The pore sizes encountered in the interstitial space range from 0.1 to 30  $\mu\text{m}$  in diameter, i.e., comparable to or significantly smaller than the size of the migrating cell (Doerschuk et al. 1993; Stoitzner et al. 2002; Weigel et al. 2012). Cells have two strategies to penetrate such confining environments: (i) expanding the openings via physical remodeling and/or proteolytic degradation of the ECM (Stetler-Stevenson et al. 1993), or (ii) contorting their shape to accommodate the available spaces (Wolf et al. 2003). The cell membrane and cytoplasm are able to quickly deform and remodel to penetrate openings less than 1  $\mu\text{m}$  in diameter (Wolf et al. 2013). In contrast, deformation of the nucleus, the largest and stiffest organelle, presents a more formidable challenge. Here we discuss emerging insights into the intracellular biomechanics and molecular processes involved in translocating the nucleus through

tight spaces, including implications on migration efficiency and other biological functions.

### **The Size and Rigidity of the Nucleus: A Physical Barrier for Cell Migration**

The nucleus is the largest organelle in the cell, with a diameter between 3-15  $\mu\text{m}$  (Lammerding 2011; Martins et al. 2012), making it substantially larger than many pores encountered during migration in physiological tissues. Furthermore, biophysical measurements of isolated nuclei and intact cells reveal that the nucleus is typically 2- to 10-times stiffer than the surrounding cytoplasm (Lammerding 2011). This combination of large size and relative rigidity of the nucleus led to the hypothesis that the nucleus can impact the cells' ability to migrate (Friedl et al. 2011). Early support for this hypothesis came from work on tumor cells migrating through microfabricated channels with precisely defined constrictions (Balzer et al. 2012; Fu et al. 2012; Tong et al. 2012).

While moderate confinement results in increased migration speed by allowing cells to employ faster migration modes (e.g., 'amoeboid migration' and 'chimneying') than during 2-D migration (Berre et al. 2015), constrictions below approximately 5  $\mu\text{m}$  in diameter require substantial nuclear deformation and result in reduced migration speeds (Balzer et al. 2012; Davidson et al. 2014, 2015; Fu et al. 2012; Lautscham et al. 2015; Tong et al. 2012). A seminal study by Friedl, Wolf, and colleagues (Wolf et al. 2013) using a range of cell types demonstrated that nuclear deformability presents a physical limit for the migration through collagen matrices with varying pore sizes. When inhibiting matrix metalloprotease (MMP) activity required to degrade ECM, migration

speed declined with decreasing pore size as nuclei had to undergo increasing deformation (Wolf et al. 2013). At pore sizes smaller than 10% of the non-deformed cross-section of the nucleus, cells reached a ‘nuclear deformation limit’ resulting in complete migration arrest, despite continued protrusion of the cytoplasm (Wolf et al. 2013). Subsequent studies using a variety of cell lines and experimental assays ranging from microfluidic devices, membranes with defined pores, ECM matrices, and *in vivo* xenografts have painted a similar picture, in which the deformability of the nucleus limits the cell’s ability to pass through tight spaces, reducing or even stalling migration as the pore size decreases below the cross-section of the nucleus (Booth-Gauthier et al. 2013; Davidson et al. 2014, 2015; Greiner et al. 2014; Guzman et al. 2014; Lautscham et al. 2015; Mak et al. 2013; Malboubi et al. 2015; Rowat et al. 2013). Assessing the role of specific physical factors on cell migration in confined environments, Lautscham and colleagues found that increased nuclear (but not cytoplasmic) volume, increased nuclear stiffness, reduced cell adhesion and lower cell contractility impaired migration through microfluidic constrictions (Lautscham et al. 2015). While the above findings prove common to a large variety of cell lines, including neutrophils, fibroblasts, and tumor cells, the exact degree of confinement necessary to elicit such effects, and the magnitude of the effect, varies with cell type. These differences indicate that variation in nuclear deformability, or the cytoskeletal forces applied to the nucleus, may be important modulators of the ‘nuclear barrier’ effect.

*Lamins determine Nuclear Deformability and Migration through Confined Environments:*

The deformability of the nucleus is largely determined by two components, the nuclear lamin network and chromatin (Fig. 1.1, Dahl et al. 2004, 2005). Lamins are type V nuclear intermediate filaments that can be divided into two sub-types, A-type (A, C, C2) and B-type (B1-3) lamins (Fisher et al. 1986; Furukawa et al. 1994; Lin and Worman 1993, 1995; Machiels et al. 1996; McKeon et al. 1986; Peter et al. 1989; Vorburger et al. 1989). The different lamin subtypes form separate but interdigitating fibrillar networks at the nuclear periphery (T. Shimi et al. 2015; Takeshi Shimi et al. 2008). In addition to regulating nuclear shape and stiffness (Dahl et al. 2004; Lammerding et al. 2004, 2006; Schäpe et al. 2009; Swift et al. 2013), they play important roles in chromatin organization, DNA damage repair, and transcriptional regulation (Ho and Lammerding 2012; Takeshi Shimi et al. 2008; Solovei et al. 2013). Cell-stretching and micropipette aspiration experiments indicate that A-type lamins have a larger impact on nuclear stiffness than B-type lamins—nuclear stiffness strongly scales with expression of lamins A/C (Lammerding et al. 2004, 2006; Schäpe et al. 2009; Swift et al. 2013), although increased expression of lamin B1 can also increase nuclear rigidity (Ferrera et al. 2014). Consistent with the ‘nuclear barrier’ hypothesis, recent studies found that cells with reduced levels of lamins A/C have more deformable nuclei and migrate faster through tight spaces than control cells with normal lamin A/C levels (Davidson et al. 2014; Harada et al. 2014). Conversely, increased expression of lamin A, or expression of a mutant lamin (progerin) that increases nuclear stiffness, impaired transit through narrow constrictions (Booth-Gauthier et al. 2013; Rowat et al. 2013). Loss of lamin A/C promotes cell migration through small constrictions by allowing larger nuclear deformation, rather than increased nuclear compression, as the nuclear volume does not

decrease during nuclear translocation (Davidson et al. 2015). These findings have direct physiological and clinical relevance, since downregulation of lamins A/C during granulopoiesis is critical for the ability of neutrophils to pass through micron-sized constrictions (Rowat et al. 2013), and misregulation of lamins is common to many cancers (Hutchison 2014). Less is known about the role of B-type lamins in 3-D migration. Loss of B-type lamins impairs migration of neurons, which lack A-type lamins, in the developing brain, and this effect is thought to be caused by defects connecting the nuclear interior and cytoplasm (Coffinier et al. 2010; Young et al. 2014). Given recent reports that lamin A/C levels and organization can vary in response to substrate stiffness and cytoskeletal tension (Buxboim et al. 2014; Ihalainen et al. 2015; Swift et al. 2013), it is intriguing to speculate that cells could also dynamically adjust their nuclear stiffness during migration.

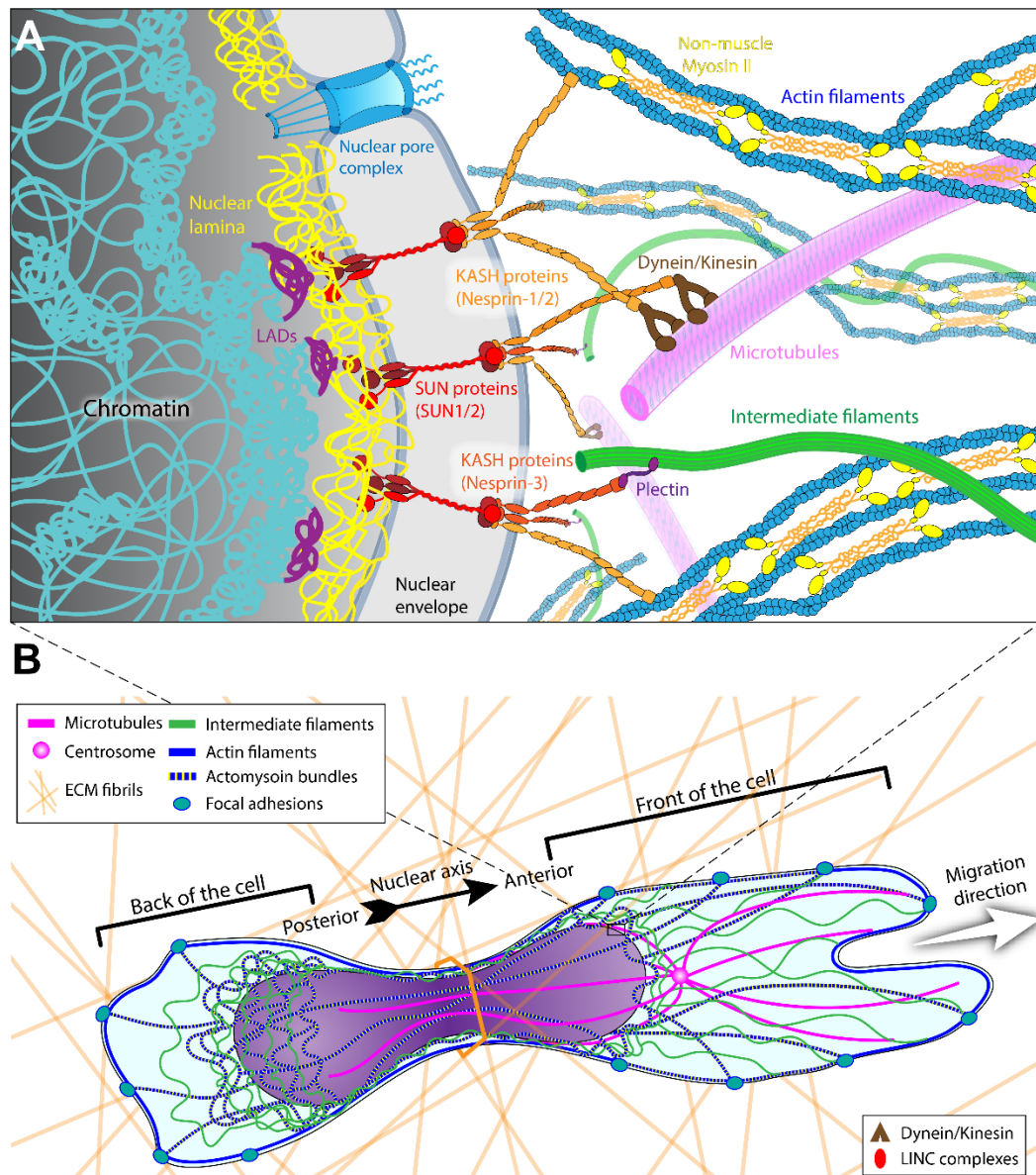


**Figure 1.1. Schematic overview of the physical connections between the nucleus and cytoskeleton, and their roles in moving the nucleus through confined spaces.**

(A) At the nuclear periphery, chromatin interacts with lamins at lamina-associated domains (LADs). SUN domain proteins (SUN1 and SUN2) are anchored to the nuclear lamina and other components of the nuclear interior by their C-terminus. The N-terminal luminal long stalks and SUN domains of SUN1/2 form trimers that interact with KASH

domain proteins located in the outer nuclear membrane (nesprin-1/-2/-3, along with the cell-type specific nesprin-4 and KASH5), forming the LINC complex (Sosa et al. 2012). The strong interaction between SUN domain trimers and the KASH domains provide the basis to mechanically couple the nuclear interior with the cytoskeleton—nesprins interact directly with actomyosin bundles, or indirectly with microtubules and intermediate filaments via intermediary proteins (such as kinesin, dynein, plectin) (Gundersen and Worman 2013). Mechanical force transmission via nucleo-cytoskeletal coupling may also trigger mechanotransduction events, ranging from the recruitment of lamins to the LINC complex to changes in chromatin organization and gene expression, which may further modulate cell migration processes. (B) Cytoskeletal organization and dynamics during migration in confined 3-D environments Figure taken from McGregor et al. 2016.

*The Role of Chromatin in Nuclear Deformability and Migration:*

Chromatin, consisting of DNA wrapped around histone octamers, occupies most of the nuclear interior and contributes to the viscoelastic response of nuclear deformation (Dahl et al. 2005; Pajerowski et al. 2007). Chromatin exists in two configurations: (i) open ‘euchromatin’, which is typically transcriptionally active, and (ii) closed, more compact ‘heterochromatin’, which is associated with inactive genes (Eissenberg and Elgin 2001). Promoting euchromatin over heterochromatin organization, for example by treatment with the deacetylase inhibitor trichostatin A (TSA), results in softer and more deformable nuclei (Pajerowski et al. 2007). Interestingly, treatment with 5'-deoxy-5'-methylthioadenosine (MTA), a methyltransferase inhibitor that cause de-

condensation of chromatin, impairs the migration of the cells through microchannels (Fu et al. 2012). It remains unclear whether this counterintuitive effect was due to the increase in nuclear size resulting from chromatin de-condensation, which may counteract reduced nuclear stiffness (Lautscham et al. 2015), or due to altered transcriptional regulation, motivating future research on the role of chromatin organization in cell migration through confining constrictions.

### **Biological Consequences of Nuclear Deformation during 3-D Cell Migration**

The nucleus is not only a passive mechanical element, but also houses the cell's genomic information and is the site of DNA replication, transcription, and RNA processing. Thus, the substantial mechanical forces and deformation incurred during migration through tight spaces may have severe biological consequences that affect cellular function and viability.

#### *Influences on Cell Survival and Genomic Stability:*

Recent studies have produced conflicting results on the effect of cell migration through tight spaces on cell viability. Whereas one study found increased apoptosis after migration through small (3  $\mu\text{m}$ ) pores, particularly in lamin A/C-deficient cells (Harada et al. 2014), others reported no noticeable increase in cell death during confinement (Davidson et al. 2014, 2015; Liu et al. 2015; Rowat et al. 2013). These apparent differences may reflect differences in cell type or mechanical confinement (e.g., porous membranes vs. microfluidic devices and collagen matrices). Interestingly, pharmacological inhibition of the heat shock protein 90 (HSP90), which facilitates DNA

damage repair (Dote et al. 2006), results in increased cell death after passage through 3- $\mu\text{m}$  diameter pores, suggesting that cells may have suffered DNA damage during migration that causes apoptosis when not adequately repaired (Harada et al. 2014). Mechanical stress alone can induce DNA damage (Mayr et al. 2002), but it remains to be seen whether the mechanical stress incurred during 3-D cell migration is sufficient to cause DNA damage.

*Influences on Mechanotransduction Signaling and Gene Expression:*

Mechanical stress on the nucleus during migration may also trigger non-lethal changes, which could further affect cell migration and cellular function. Recent studies in which isolated nuclei were subjected to mechanical stress suggest that the nucleus itself can act as a mechanosensitive element. Force application via the LINC complex induces rapid phosphorylation of the inner nuclear membrane protein emerin, leading to recruitment of lamin A/C to the nuclear envelope and nuclear stiffening (Guilluy et al. 2014). Shearing isolated nuclei causes partial unfolding of lamin A/C, exposing cryptic binding sites that could initiate mechanotransduction events (Swift et al. 2013). Furthermore, changes in the mechanical microenvironment and force application to intact cells can induce chromatin remodeling (Iyer et al. 2012; Li et al. 2011) and dissociation of nuclear protein complexes (Poh et al. 2012), which could affect both nuclear deformability and gene expression (see Kaminski et al. 2014 and Guilluy and Burridge 2015) for a detailed discussion of nuclear mechanotransduction). While these reports suggest that nuclear deformation during 3-D migration could affect nuclear

organization, chromatin remodeling, and gene expression, direct experimental evidence for this hypothesis is still missing.

### **Clinical Significance of Lamins in Disease**

Mutations in lamins cause a large spectrum of human diseases, ranging from muscular dystrophy and dilated cardiomyopathy to premature aging (Davidson and Lammerding 2014; Schreiber and Kennedy 2013). Increasing reports indicate that altered lamin expression (rather than mutations) is found in many cancers, and often correlates with negative clinical outcomes (Denais and Lammerding 2014; Hutchison 2014; Krause and Wolf 2015). For example, reduced expression of lamin A/C has been reported in breast (Capo-chichi et al. 2011; Wazir et al. 2013) and cervical cancer (Capo-chichi et al. 2015), and is correlated with an increased recurrence of stage II and III colon cancer (Belt et al. 2011) and reduced disease free survival in breast cancer (Wazir et al. 2013). However, in other cases, increased A-type lamin expression is associated with disease progression, specifically in prostate, colon and ovarian cancers (Chow et al. 2012a; Willis et al. 2008). Given the multiple function of lamins, changes in their expression are expected to have pleiotropic effects, affecting not only nuclear stiffness but also proliferation, survival, and gene expression (Chow et al. 2012b; Denais and Lammerding 2014; Hutchison 2014; Krause and Wolf 2015; Mitchell et al. 2015). Nonetheless, it is intriguing that more invasive breast cancer cell lines such as Hs578T and MDA-MB-231 are capable of more extensive nuclear deformation than normal and non-malignant controls (Chiotaki et al. 2014), and move faster through migration devices designed to mimic tight spaces inside the body (Fu et al. 2012). Future studies

should be directed at characterizing the effects of altered lamin levels on cell migration, as well as other cellular functions, in more detail.

### **Conclusions and Outlook**

The nucleus has long been recognized as a central hub for genomic information and its processing. Work published over the last few years makes it clear that one also has to consider the physical impact of the nucleus on cellular function, particularly during migration in 3-D environments. The nucleus, with its large volume and relative rigidity, acts as physical barrier when cells encounter pore sizes smaller than the nuclear diameter, resulting in reduced migration efficiency or even complete migration arrest. The extent of this nuclear barrier effect is largely driven by the nuclear size and stiffness, which is governed by the levels of the nuclear envelope proteins lamin A/C and chromatin organization. These findings are particularly relevant to immune cells and to invading cancer cells, which move through tissues with pore sizes smaller than the size of the nucleus and often have altered expression of lamins and other nuclear envelope proteins. Despite recent advances, many open questions remain. For example, can cells dynamically adjust their nuclear stiffness to facilitate cell migration through tight spaces, possibly by phosphorylation and/or degradation of nuclear lamins? Are some cells particularly well suited for 3-D migration, either by having more deformable nuclei or by pulling/pushing harder on the nucleus? What are the precise molecular mechanisms by which cells translocate the nucleus through tight constrictions? And what are the biological consequences resulting from the large nuclear deformations, which could include changes in chromatin organization, DNA damage, and altered gene

expression? Such mechanically induced events could not only affect migration itself, e.g., by altering nuclear stiffness and cytoskeletal dynamics, but also modulate various other cellular functions and even viability. To drive new discoveries, it will be crucial to combine new imaging tools, such as fluorescence resonance energy transfer (FRET)-based intracellular force probes (Cost et al. 2015), with microfabricated environments that mimic physiological environments while providing defined geometries and enhanced live-cell imaging conditions, as well as single cell based assays to measure cell viability, gene expression, and epigenetic modification. Further insights into the role of the nucleus in 3-D migration will not only improve our understanding of the physical constraints during migration in physiological environments, but may ultimately lead to new strategies to better target invasive cancer cells and to reduce or eliminate metastatic spreading.

## CHAPTER 2: CHARACTERIZATION OF NUCLEAR ENVELOPE RUPTURE IN 3-D CONFINED CELL MIGRATION<sup>2</sup>

### **Abstract**

During cancer metastasis, cells must squeeze through tight interstitial spaces, requiring extensive deformation of the cell and its nucleus. Although the cell cytoplasm can easily squeeze through such small spaces, larger organelles such as the nucleus are often bigger than the size of these openings, and must undergo major deformation. We predicted that the extreme nuclear deformation necessary for successful transit through tight spaces may pose a substantial mechanical challenge to the integrity of the nucleus. To study such cell migration, we used microfluidic devices with constrictions similar in size to *in vivo* interstitial spaces. We found that when cells transited through confined microenvironments, their nuclei exhibited a transient loss of NE integrity—NE rupture. During NE rupture, a temporary exchange of nuclear and cytoplasmic content occurs. NE rupture was also associated with herniation of chromatin across the NE. Cells were able to repair the NE damage, and remain viable. Such phenomenon was identified in

---

<sup>2</sup> Segments of the text and figures are reproduced from the following publications:

Denais, C.M. †, Gilbert, R.M. †, Isermann, P. †, **McGregor, A.L.**, Lindert, M., Weigelin, B., Davidson, P., Friedl, P., Wolf, K., Lammerding, J. (2016). Nuclear envelope rupture and repair during cancer cell migration in confining microenvironments, *Science* 352(6283), 353-8. †, authors contributed equally.

Carey, S.P, Starchenko, A., **McGregor, A.L.**, Reinhart-King, C.A. (2013). Leading Malignant Cells Initiate Collective Epithelial Cell Invasion in a Three-Dimensional Heterotypic Tumor Spheroid Model, *Clinical and Experimental Metastasis* 30(5), 615-30.

Author contributions: CD, RG, and PI identified NE rupture in MDA-MB-231 and HT1080 cells. ALM identified and characterized NE rupture in SV40 fibroblasts. ALM, CD, RG, and PI characterized NE rupture in various cell lines in microfluidic devices. ALM and KW identified and characterized NE rupture in MDA-MB-231 and SV40 cells in collagen scaffolds.

multiple cell lines, and correlated with increasingly confined spaces both in *in vitro* assays, and *in vivo*-like collagen assays. Our findings illustrate that the integrity of the NE is challenged during confined cell migration, which could promote drivers of increased metastatic potential such as DNA damage, aneuploidy, and genomic rearrangements.

## **Introduction**

In breast cancer, the 5-year survival rate decreases substantially in tumors that have metastasized to secondary organs (National Cancer Institute, 2018). In metastasis, cancer cells must successfully invade into surrounding tissues, enter the blood or lymphatic vessels, and extravasate out of the vessels to form secondary tumors (Chaffer and Weinberg 2011; Hanahan and Weinberg 2011). During such metastasis, cells must often migrate through spaces smaller than their nucleus (Doerschuk et al. 1993; Stoitzner et al. 2002; Weigelin et al. 2012), the largest and stiffest organelle in the cell. Such migration requires the deformation of both the cytoplasm and nucleus. Nuclear stiffness, determined by lamin expression and chromatin condensation, is the major determinant in a cell's ability to squeeze through confined spaces (Dahl et al. 2004, 2005; Friedl et al. 2011).

To study the role of nuclear deformation in cancer cell migration, our laboratory designed microfluidic devices that mimic *in vivo* spacing, and allows for long-term, high resolution imaging and visualization of cells migrating in 3D (Davidson et al. 2015). We also used collagen matrix assays to observe the nucleus during confined migration,

in a more *in vivo*-like assay (Fig. 2.1; Carey et al. 2013) Observation of cell migration revealed a phenomenon called NE rupture—where the NE loses integrity, and there is an exchange of nuclear and cytoplasmic contents (Denais et al. 2016; Raab et al. 2016).

NE rupture as a phenomenon was initially described in the 1960s when mitochondria were observed in cell nuclei (Brandes et al. 1965). NE rupture had also been observed in cancer cells with improperly formed nuclear lamina (Vargas et al. 2012). However, the presence of NE rupture during cell migration, and in increasingly more confined microenvironments was not known. Using novel assays to enable high-resolution imaging in real-time, we observed that NE rupture correlated with an increase in confinement—both in the microfluidic devices and collagen assays. Our studies also illustrated an increase in nuclear fragmentation following confined migration, another indicator of NE damage. Significantly, our laboratory found that NE rupture in cancer cells migrating through confined spaces occurred at a rate 10-20 times greater than NE rupture in cells on 2D substrates previously described in the literature (Denais et al. 2016), revealing that NE rupture likely plays a significant role in cancer cell migration.

## **Materials and Methods**

### *Cell Culture Techniques:*

MDA-MB-231, HT-1080, and SV40 human fibroblasts were obtained from the American Type Culture Collection (ATCC) and Coriell Institute (SV40 human fibroblasts). All cells were grown in DMEM (Gibco) supplemented with L-glutamine,

10% FBS (VWR), and 1% Pen/Strep (Gibco). All cells were cultured at 37° C and 5% CO<sub>2</sub>.

*Generation of Fluorescently Labelled Cell Lines:*

All cell lines were stably modified with lentiviral vectors to express the NE rupture reporter NLS-GFP (pCDH-CMV-NLS-copGFP-EF1-blastiS). Cells were virally transformed using pseudoviral particles. In brief, 293-TN cells (SBI) were co-transfected with the lentiviral plasmid and lentiviral helper plasmids (psPAX2 and pMD2.G, gifts from Didier Trono) using PureFection (SBI), following manufactures protocol. Lentivirus-containing supernatants were collected at 48 hours and 72 hours after transfection, and filtered through a 0.45 µm filter. Cells were seeded into 6-well plates so that they reached 50-60% confluency on the day of infection and transduced at most three consecutive days with the viral stock in the presence of 8 µg/mL polybrene (Sigma-Aldrich). The viral solution was replaced with fresh culture medium, and cells were cultured for 24 hours before selection with 10 µg/mL of blasticidine S for 10 days.

*Microfluidic Device Preparation:*

Microfluidic devices fabricated via 2-layer SU-8 photolithography were used to create polydimethylsiloxane (PDMS, Dow-Corning) replicates. Nanofabrication techniques to create the silicon wafer for the devices were used as described previously (Davidson et al. 2015). PDMS stamps of microfluidic devices were covalently attached to glass coverslips via plasma cleaning (Harrick Plasma), and covalent bonds were enhanced via a short 5-minute heat incubation. Devices were washed 1× with 70% ethanol and 2×

with water, then coated with 20  $\mu$ g fibronectin (Invitrogen) diluted in 1 $\times$  PBS, either at 37 $^{\circ}$  C for two hours, or overnight at 4 $^{\circ}$ C. Following fibronectin coating, the devices were rinsed 1 $\times$  with complete media to remove any excess fibronectin.

Cells were seeded into the microfluidic devices the evening before imaging at a density of 30,000 cells/device. The following morning media was removed, and a 0 to 10% FBS gradient was established across the migration channels. Prior to beginning overnight imaging cell media was changed to phenol-red free medium (Gibco) to reduce background fluorescence.

#### *Collagen Matrix Migration Assays:*

Experiments studying cell migration in collagen matrices were performed either using spheroid invasion assays (human skin fibroblasts) or single cells in collagen matrices (HT1080 cells and human skin fibroblasts) as described below.

#### *Spheroid Invasion Assay:*

For the spheroid invasion assay, we followed previously established procedures (Carey et al. 2013). In brief, cells from confluent cultures were used to generate multicellular spheroids in 96-well round-bottom plates (Costar). For each spheroid, 50,000 cells were combined with a solution of 0.25% MethoCult (Stem Cell Technologies) and complete medium, spun down in round-bottom wells at 1,000 rpm for 5 minutes, and allowed to condense for 48 hours. Individual, well-formed spheroids were then selected for embedding into collagen matrices prepared from type I rat-tail collagen (Corning) at

various densities (1.5 mg/mL to 3 mg/mL). Collagen solutions were reconstituted in complete DMEM and then neutralized with 1 N NaOH. Cells or cell spheroids were added to the collagen solution prior to polymerization, which was then allowed to polymerize at 37° C for 30 minutes before adding complete medium. For some experiments, medium was supplemented with the broad MMP inhibitor GM6001 (EMD Millipore, 20 µM; Carey et al. 2012). Imaging was carried out 24-48 hours after embedding the spheroid in the collagen matrix (Fig. 2.1).

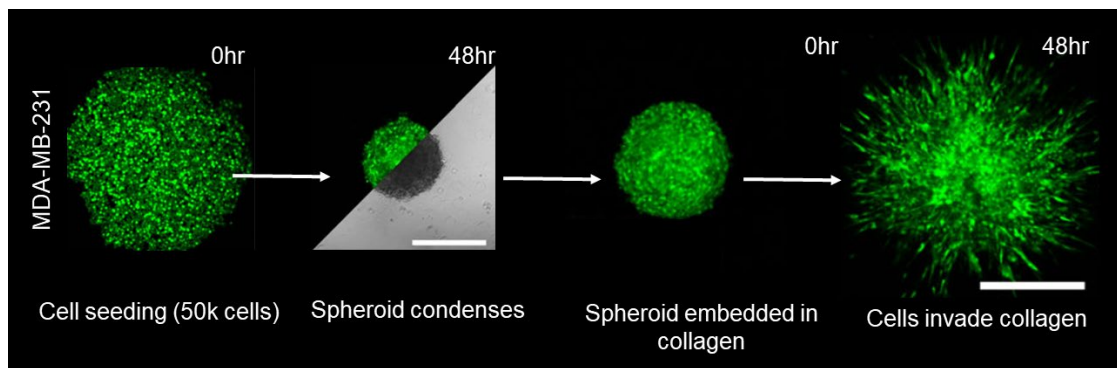


**Fig 2.1: Multicellular spheroid assay.** At 0 hours, cells were seeded into round-bottom 96-well plates with Methocult media. Spheroids were allowed to condense for 48 hours, and embedded into collagen matrices with collagen concentrations of 1.5 mg/mL to 3 mg/mL. Cells were allowed to invade into the collagen, and imaged using a confocal microscope. Spheroids shown here embedded in collagen are maximum intensity projections of multiple z-stack images of cells invading collagen. Scale bars: 500µm. Figure adapted from Carey et al. 2013.

*Single Cell Invasion Assays:*

For the analysis of nuclear fragmentation, 40,000 cells/condition were added into collagen matrices of different densities (1.5 mg/mL to 2.5 mg/mL) with or without GM6001. Cells were allowed to migrate through the collagen for 5 days, before z-stacks of the cells were taken with a laser scanning confocal microscope (LSM 700, Zeiss). Maximum intensity projection images of the unfixed cells were used to quantify the number of cells that had normal, ruptured, or fragment nuclei.

*Time-Lapse Microscopy:*

Microfluidic device migration experiments were acquired overnight using time-lapse imaging on a laser scanning microscope (LSM 700, Zeiss) taken at 20× magnification (NA 0.8 air objective) with a CCD CoolSNAP EZ camera (Photometrics). Samples were placed on temperature-controlled stage set at 37° C and imaged every 10 minutes for 17 hours. Collagen matrix samples were acquired similarly, using a 40× (NA 0.8 water-immersion) objective to acquire Z-stacks 1-3 μm deep in order to capture cells as they migrated through different planes of the collagen. Following completion of the experiment, maximum projection images were computed using the ZEN Black (Zeiss) software.

*Image Analysis:*

NE rupture presence and duration was quantified based on spillage of nuclear localization sequence (NLS)-copGFP from the nucleus into the cytoplasm. NE rupture was visually analyzed to indicate when the event began and ended, and if the cell was migrating through a constriction. Results were recorded using Microsoft Excel. Nuclear

rupture was detected by an increase in cytoplasmic NLS-GFP signal, and was considered complete following NLS-GFP repackaging into the nucleus. Cells that did not undergo NE rupture, but still successfully migrated through constrictions were also recorded in order to quantify NE rupture rates per cell line. This process was performed for both microfluidic devices and collagen matrices.

To quantify the frequency of chromatin protrusions and nuclear fragmentation in cells in collagen matrices, maximum intensity projections were computed from the 3-D image stacks for a total of four areas per sample. Cells within each maximum projection image were then classified as having intact nuclei, chromatin protrusions, or fragmented nuclei based on the morphology of the fluorescently labeled nuclei.

#### *Statistics:*

Statistics were calculated using GRAPHPad Prism software. Distributions of both transit time and NE rupture duration were tested for Gaussian distribution, and means were then compared using the appropriate statistical test. If distributions were considered Gaussian, a one-way ANOVA was performed with a Tukey's multiple comparison post-test. Samples that were not normally distributed were compared using a one-way ANOVA with Dunn's multiple comparison post-test. Western Blot differences were calculated, and differences were determined via a one-way ANOVA.

## **Results**

### *Nuclear Envelope Rupture Occurs in Various Cell Lines:*

Although NE rupture had been previously reported in cells, it had never been studied in cells migrating through confined spaces. When observing nuclear deformation during migration through variable confined spaces, we noticed that NLS-GFP spilled out of the nucleus and into the cell cytoplasm. Within 90-120 minutes, on average, the NLS-GFP was repackaged into the nucleus, and the cells were able to continue migrating and dividing. Intriguingly, cell death was rare in cells undergoing NE rupture, even though nuclear blebbing, fragmentation, and chromatin herniation were often observed following a NE rupture event.

This phenomenon was observed in various migratory cell lines including, but not limited to, MDA-MB-231 triple-negative breast cancer cells, HT-1080 fibrosarcoma cells, and SV40 human skin fibroblasts (Fig. 2.2A,B). Importantly, not all cells migrating through constrictions experienced NE rupture (Fig. 2.2C), although there was no clear differentiating factor between cells that experienced NE rupture during confined migration, and those that did not.

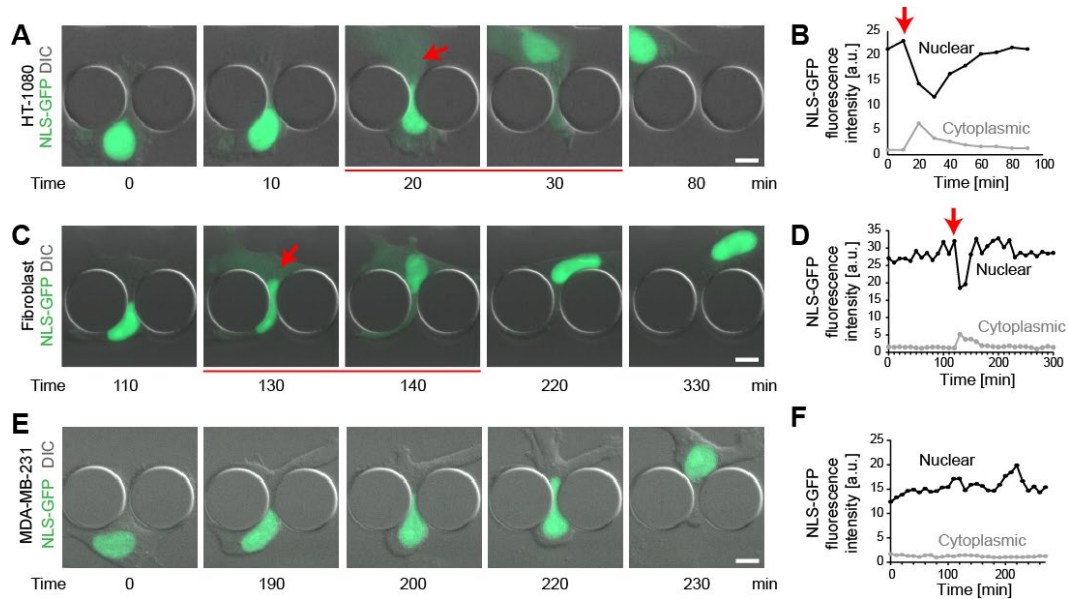


**Figure 2.2: NE rupture of cell migrating through confinement.** NLS-GFP is labeled in green. (A, C) HT-1080 fibrosarcoma cell and SV40-transformed skin fibroblast, respectively, undergoing NE rupture while migrating through  $2 \times 5 \mu\text{m}^2$  constriction. (E) MDA-MB-231 metastatic breast cancer cell migrating through  $2 \times 5 \mu\text{m}^2$  constriction without NE rupture. Red arrow indicates time of NE rupture, and the red line indicates the duration of rupture. Scale bars:  $10 \mu\text{m}$ . (B, D, F) Fluorescence intensity in arbitrary units in the nucleus (black) and cytoplasm (gray) vs. time in minutes. Red arrow indicates the time of NE rupture, as seen by the drop in nuclear fluorescent intensity, and concomitant increase in cytoplasm fluorescence intensity. Figure adapted from Denais et al. 2016.

*Nuclear Envelope Rupture Occurs in Collagen Matrices:*

While the observance of NE rupture in controlled, microfluidic migration devices was novel, it was essential to illustrate that NE rupture also occurred in assays that more

closely recapitulated the *in vivo* cell microenvironment. Using collagen matrix assays, single-cells and tumor spheroids were embedded into variable collagen densities with and without a broad-spectrum MMP inhibitor, GM6001, and were allowed to migrate for 24-48 hours. During this time, collagen scaffolds were imaged in multiple Z-planes and positions to observe cell migration and nuclear deformation, allowing us to observe NE rupture in cells as they invaded out of tumor spheroids, and into dense collagen (Fig. 2.3). However, initial work was not able to capture the resealing of the NE following rupture, due to cells migrating out of the z-stack and/or plane of view.

To overcome such issues, single-cells were embedded into collagen matrices, and imaged similarly to the embedded tumor spheroids. Single-cell migration provided many additional opportunities to visualize NE rupture, and quickly revealed multiple examples of cells experiencing NE rupture in collagen, repackaging, and continuing to migrate and divide.

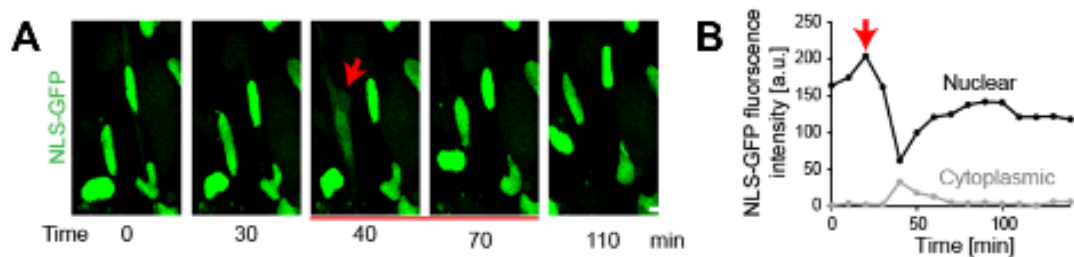


**Figure 2.3: NE rupture in collagen matrices.** (A) Maximum intensity projection of SV40-transformed human fibroblasts migrating in 3.0 mg/ml collagen matrix. Cell nuclei were labeled with NLS-GFP. Red arrow indicates rupturing cell, and red line

represents the duration of NE rupture. (B) Fluorescence intensity in arbitrary units in the nucleus (black) and cytoplasm (gray) vs. time in minutes. Red arrow indicates the time of rupture, visibly by a drop in green nuclear fluorescent intensity, and an increase in cytoplasm fluorescence intensity. Adapted from Denais et al. 2016.

*Nuclear Envelope Rupture Rate Increases with Cell Confinement:*

Initial indications of NE rupture occurring during cell migration was observed in cells migrating through confined spaces much smaller than the size of the cells' nucleus ( $1 \times 5 \mu\text{m}^2$  and  $2 \times 5 \mu\text{m}^2$  constrictions; Fig. 2.4A). When observing cells migrating through constrictions much larger than the size of the nucleus ( $15 \times 5 \mu\text{m}^2$ ), NE rupture occurred much less frequently (Fig.2.4A). This observation was consistent across various cell lines migrating through microfluidic devices and collagen matrices (Fig. 2.4C). Similarly, experiments with collagen matrices revealed that when cells were embedded in denser collagen matrices, nuclei were much more likely to experience NE fragmentation, which can be an indicator of NE deformation and rupture (Fig. 2.4B).

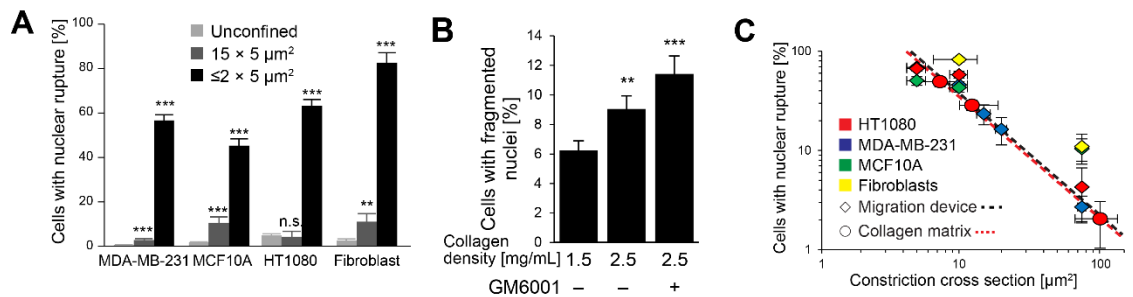


**Fig 2.4: Incidence of NE rupture and nuclear fragmentation in various cell lines in 2D cultures, microfluidic devices, and collagen matrices. (A) Incidence of NE**

rupture for a variety of human cell lines migrating through  $2 \times 5 \mu\text{m}^2$  constrictions. Measurements of cells inside the same device migrating in unconfined 2-D regions and in  $15 \times 5 \mu\text{m}^2$  large channels, which require only minimal nuclear deformation, serve as comparison.  $n = 69\text{--}2256$  cells per condition, comparison relative to unconfined condition. (B) Percent of SV40-transformed human skin fibroblasts with nuclear fragmentation in increasing collagen density and MMP inhibition. 2D represents unconfined migration on glass slides.  $n = 50\text{--}146$  cells per condition. (C) Incidence of NE rupture as function of constriction sizes in collagen matrices (slope =  $-1.224$ ;  $R^2 = 0.999$ ) and microfluidic devices during  $\approx 12$  hour period (slope =  $-1.219$ ;  $R^2 = 0.974$ ). Regression based on HT1080 and MDA-MB-231 cells;  $n = 55\text{--}445$  cells per condition. \*\* denotes  $p \leq 0.01$ , and \*\*\* denotes  $p \leq 0.001$ . Error bars represent the standard error of the mean. Figure adapted from Denais et al. 2016.

## Discussion

Using microfluidic devices and collagen matrices to observe the nucleus during confined migration, we frequently noted NE deformation resulting in the temporary loss of NE integrity—NE rupture (Fig. 2.2 and Fig. 2.3). Similar work in bone-marrow derived mouse dendritic cells also observed the presence of NE rupture during confined migration (Raab et al. 2016). Previously, NE rupture had been implicated in 2-dimensional (2D) cell migration (Vargas et al. 2012), but not in 3-dimensional (3D) cell migration assays.

In our experiments, we observed that with decreasing pore size, there was an

exponential increase in the presence of NE rupture and nuclear fragmentation (Fig. 2.4). This provided further evidence that the nuclear deformability is a rate-limiting step during confined cell migration (Davidson et al. 2014; Harada et al. 2014; Wolf et al. 2013). As such, our study demonstrates that cell migration through small spaces can challenge the integrity of the NE and DNA content, which could promote DNA damage, aneuploidy, and genetic instability, and—in the absence of efficient repair—cell death (Denais et al, 2016; Raab et al. 2016).

### **Future Work**

One of the primary determinants of nuclear deformability is the expression of lamins A and C proteins that form the nuclear lamina, a dense protein network underlying the inner nuclear membrane (Lammerding et al. 2006; Stephens et al. 2017). Intriguingly, expression of lamin A/C is decreased in many cancers (Bell and Lammerding 2016; Irianto et al. 2016; Matsumoto et al. 2015; Wazir et al. 2013), which could contribute to increased metastatic potential of tumor cells by facilitating both invasion and intra- and extravasation. Specifically, in breast cancer, previous studies have shown that more aggressive tissue samples express lower levels of lamins A and C, and that lower levels of lamin A expression are correlated with lower rates of disease-free survival (Capo-chichi et al. 2011; Wazir et al. 2013). Taken together, our results and previous studies provide a strong reason to (i) further elucidate how NE rupture varies amongst cell lines of different metastatic potential, and (ii) long-term impact of DNA damage, chromatin herniation, and nuclear fragmentation on cell proliferation, cell cycle arrest, and cell senescence in these various cell lines (Fig. 2.5).

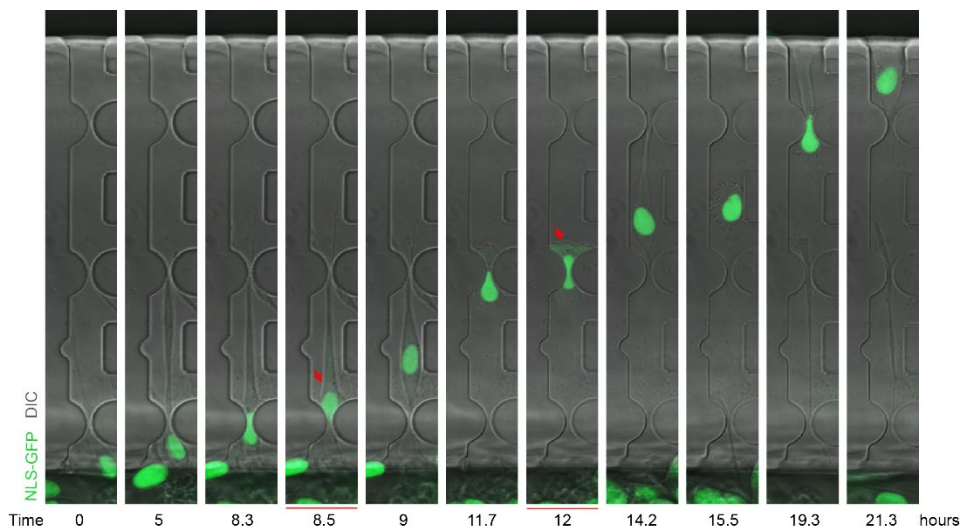


**Figure 2.5: Long-term confined cell migration of TGF- $\beta$  treated Flox3-PyMT cells.**

Cell migrating through constrictions during long-term time-lapse experiment. NLS-GFP is labeled in green. Time 0 is relative to the cell of interest entering the constriction area. The total experiment time was 72 hours, and the cell depicted here crossed all three constrictions in under 22 hours. Red arrows indicate NE ruptures.

However, analysis of NE rupture and migration requires extensive manual input, and is susceptible to variability between analyzers. Time-lapse experiments are often longer than 12 hours, with multi-color images acquired every ten minutes—resulting in large, multidimensional data sets that take several days to weeks to analyze manually. Such low throughput image analysis provides a substantial challenge when studying large sets of experimental conditions, thereby requiring automated image analysis to achieve sufficiently high throughput. The development of an automated analysis tool would enable complete studies of breast cancer cell line panels, providing a clearer

understanding of how NE rupture may vary with metastatic potential. This work is described in the following chapter.

## CHAPTER 3: THE DEVELOPMENT OF TOOLS TO STUDY THE ROLE OF NUCLEAR DEFORMATION AND RUPTURE IN CELL MIGRATION<sup>3</sup>

### **Abstract**

Recent *in vitro* and *in vivo* studies have highlighted the importance of the cell nucleus in governing migration through confined environments. Microfluidic devices that mimic the narrow interstitial spaces of tissues have emerged as important tools to study cellular dynamics during confined migration, including the consequences of nuclear deformation and rupture. However, while image acquisition can be readily automated on motorized microscopes, the analysis of the corresponding time-lapse sequences for nuclear transit times and events such as nuclear NE rupture requires extensive manual input. In addition to being highly time-consuming, such manual analysis is susceptible to person-to-person variability. Studies that compare large numbers of cell types or conditions thereby require automated image analysis to achieve sufficiently high

---

<sup>3</sup> Segments of the text and figures are produced from the following published manuscript:

Elacqua, J.J.,McGregor, A.L., Lammerding, J. (2018). Automated Analysis of Cell Migration and Nuclear Envelope Rupture in Confined Environments. PLOS One 13(4) e0195664.

Author contributions: ALM created and tested a two-fluorophore retrovirus for identifying cells undergoing NE rupture, and stably modified all cell lines used, enabling automated tracking and analysis of nuclear migration and NE rupture. ALM, JJE, and JL conceptualized the function, methodology, and format for automated analysis program—including, but not limited to inputs necessary for proper automation, desired outputs, and the methods used to achieve sophisticated results. JJE implemented automation using MATLAB for software development. Software was validated and tested by ALM and JJE. Emily Bell, Gregory Fedorchak, Philipp Isermann, Jay Jun, Jineet Patel, and Pragya Shah provided additional, blinded manual analysis comparisons in which to compare software analysis success. Troubleshooting and iterations of the program were performed by ALM and JJE, with input for changes from the Lammerding lab members. ALM mentored JJE as an undergraduate student in the lab, initially enabling JJE to understand how manual analysis was performed, and working with JJE daily to establish methods to create an automated analysis program. ALM, JJE, and JL wrote, reviewed, and edited manuscript. ALM and JJE created figures.

throughput. Here, we present an automated image analysis program to register microfluidic constrictions and perform image segmentation to detect individual cell nuclei. The MATLAB program tracks nuclear migration over time and records constriction-transit events, transit times, transit success rates, and nuclear envelope rupture. Such automation reduces the time required to analyze migration experiments from weeks to hours, and removes the variability that arises from different human analysts. Comparison with manual analysis confirmed that both constriction transit and nuclear envelope rupture were detected correctly and reliably, and the automated analysis results closely matched a manual analysis gold standard. The program thus presents a versatile tool for the study of confined migration and its effect on the cell nucleus.

## **Introduction**

Cell migration is necessary for a number of important physiological and pathological processes, including immune response, wound healing, and cancer metastasis. For cancer cells to metastasize, they must first migrate away from the site of the primary tumor (invasion), enter blood or lymphatic vessels (intravasation), exit the vessels (extravasation), and then migrate to new sites, where they may grow into secondary tumors (Chaffer and Weinberg 2011; Poste and Fidler 1980). Preventing or reducing cancer cell migration could significantly improve cancer patient outcomes, and present a key step in reducing metastasis-related mortality.

During the processes of tissue invasion and intra- and extravasation, cancer cells have

to squeeze through small spaces between other cells and within the ECM. Recent findings point to an important role of the cell nucleus in the migration of cells through such confined environments (Krause and Wolf 2015). Deformation of the nucleus, which is the largest and stiffest cellular organelle, determines the ability of cells to pass through constrictions smaller than the nuclear cross-section (Friedl et al. 2011; Krause and Wolf 2015; Wolf et al. 2013). Cells with less deformable nuclei take longer to pass through microscopic pores than cells with more deformable nuclei (Davidson et al. 2014; Harada et al. 2014; Rowat et al. 2013). One of the primary determinants of nuclear deformability is the expression of lamins A and C, intermediate filament proteins that form a dense protein network (nuclear lamina) underneath the inner nuclear membrane (Lammerding et al. 2006; Stephens et al. 2017). Intriguingly, expression of lamin A/C is decreased in many cancers (Bell and Lammerding 2016; Irianto et al. 2016; Matsumoto et al. 2015; Wazir et al. 2013), which could contribute to increased metastatic potential of tumor cells by facilitating both invasion and intra- and extravasation.

In addition to modulating transit efficiency through confined environments, migration through tight spaces places substantial physical stresses on the nucleus, which can lead to a transient loss of NE integrity during interphase, referred to as NE rupture (Denais et al. 2016; Raab et al. 2016). NE rupture, which allows uncontrolled exchange of cytoplasmic and nuclear proteins, along with protrusion of chromatin into the cytoplasm, could result in increased genomic instability and promote cancer progression (Shah et al. 2017). Cells can restore NE integrity using components of the endosomal

sorting complexes required for transport-III (ESCRT-III) machinery (Denais et al. 2016; Raab et al. 2016). Inhibiting NE repair, when combined with inhibition of DNA damage repair pathways, results in substantially increased cell death after NE rupture (Denais et al. 2016; Raab et al. 2016), pointing to potential treatment approaches to specifically target metastatic cancer cells.

These findings have motivated a rapidly growing interest in studying nuclear deformation and NE rupture, particularly during confined migration (Davidson et al. 2015; Lim et al. 2016; McGregor et al. 2016; Raab et al. 2016; Shah et al. 2017; Stephens et al. 2017; Takaki et al. 2017). Microfluidic devices with precisely defined constrictions that mimic interstitial spaces *in vivo* have emerged as powerful tools to study the role of nuclear deformation and NE rupture in cell migration (Davidson et al. 2014, 2015; Denais et al. 2016; Fu et al. 2012; Lautscham et al. 2015; Malboubi et al. 2015; Mekhdjian et al. 2017; Raab et al. 2016; Thomas et al. 2015). Although the walls of such devices are more rigid than the *in vivo* spaces through which cells migrate, confined migration and NE rupture results obtained in these microfluidic devices closely match those obtained in collagen matrices and from intravital imaging studies (Denais et al. 2016; Raab et al. 2016), and the devices enable time-lapse imaging of single-cell migration under precisely defined conditions. In such experiments, nuclei are often identified by fluorescently labeled DNA (e.g., staining with Hoechst 33342) or histones (e.g., expression of H2B-tdTomato). NE rupture events can be detected by monitoring the intracellular localization of NLS-GFP (Denais et al. 2016; Raab et al. 2016). NLS-GFP is normally contained within the nucleus but spills into the cytoplasm during NE

rupture and is gradually re-imported into the nucleus upon NE repair (Fig. 3.1).

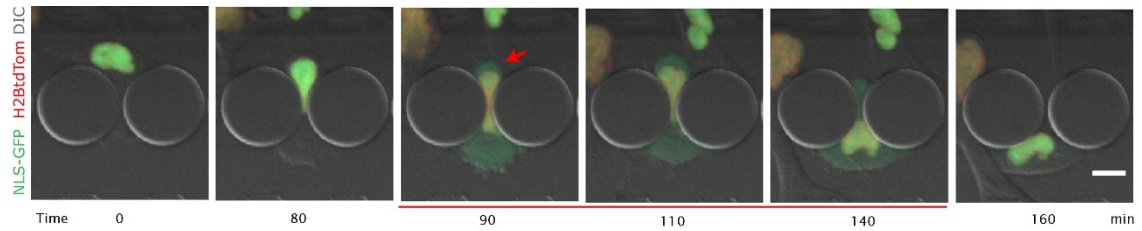


**Figure 3.1 Representative example of MDA-MB-231 cell experiencing NE rupture during migration through 2  $\mu\text{m}$  constriction.** NLS-GFP is shown in green, and histone H2B is shown in red. Red arrow indicates initial NE rupture frame, and red line below frames indicates duration of NE rupture. Scale bar: 20  $\mu\text{m}$ .

Time-lapse experiments using cancer cells typically cover 6 to 24 hours, with multi-color (fluorescence and transmitted light) images acquired every 2 to 10 minutes, resulting in large (> 40 GB per experiment), multidimensional data sets that take several days to weeks to manually analyze. Such low throughput image analysis provides a substantial challenge when studying large sets of experimental conditions. Furthermore, manual analysis by different observers can add substantial variability to the experimental data (Fig. 3.2).

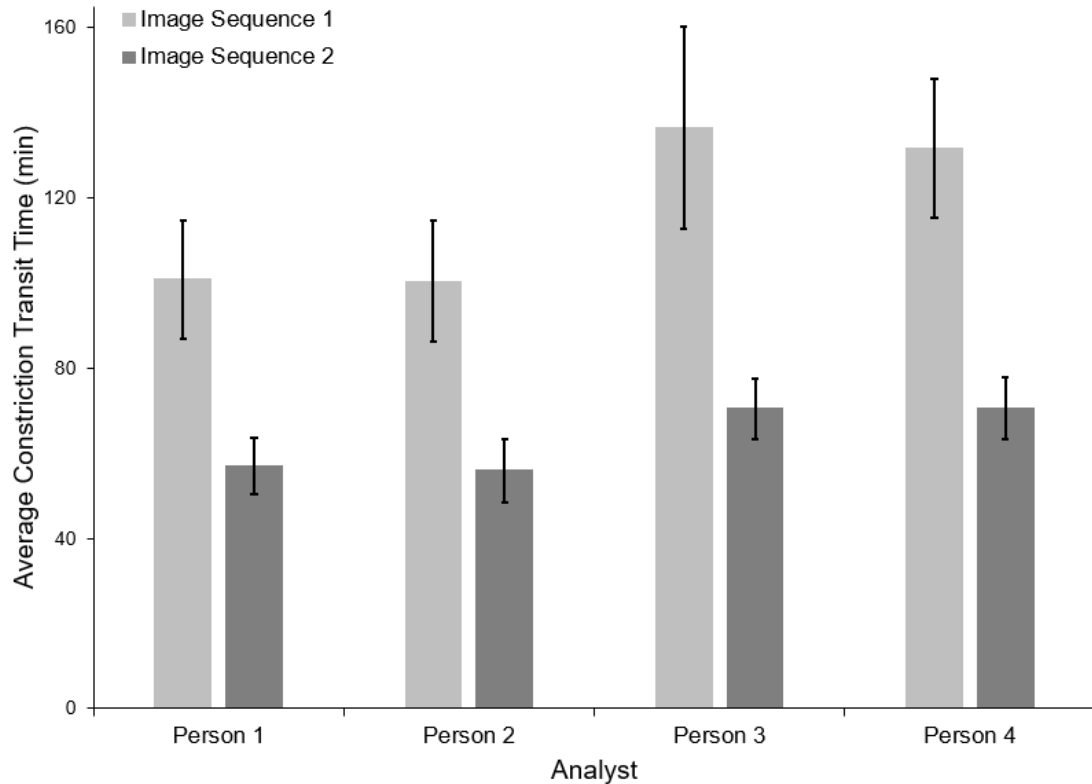


**Figure 3.2: Comparison of transit time analysis results from multiple independent analysts.** Constriction transit times (mean  $\pm$  s.e.m.) determined by four manual analysts for BT-549 breast cancer cells either overexpressing lamin A (Image sequence 1) or an empty vector (Image sequence 2). Overexpression of lamin A results in less deformable nuclei and longer transit times through narrow constrictions (\*,  $p < 0.05$ ; \*\*,  $p < 0.001$  as calculated by ANOVA followed by Tukey's multiple comparison test;  $n = 23 \pm 26$  and  $20 \pm 24$  (depending on the analyst), respectively). Figure adapted from Elacqua et al. 2018.

To address these issues, we developed a MATLAB program to perform the image analysis in an automated, reproducible, and robust process. The program is capable of

tracking individual cells/nuclei as they migrate through microfluidic constriction channels and compute transit times for individual constrictions. While primarily intended to study cell migration in confined environments, the program can also be used to study cells migrating on unconfined 2-D substrates. The program can also reliably detect NE rupture events and their duration. The program automatically recognizes dividing cells, resulting in increased robustness and accuracy comparable to expert manual analysis, but with substantially increased efficiency.

## **Materials and Methods**

### *Generation of Fluorescently Labelled Cell Lines:*

Cell lines were stably modified with a retroviral vector to express both the NE rupture reporter NLS-GFP, and histone marker H2B-tdTomato (pQCXIP-NLS-copGFP-P2A-H2B-tdTomato-IRES-puro, System Biosciences; Fig. 3.3). The retroviral vector was generated in two steps. LifeAct-GFP was digested out of the pQCXIP-LifeAct-GFP-P2A-H2B-tdTomato vector, and NLS-copGFP was ligated into the vector. NLS-copGFP was obtained from a lentiviral vector (pCDH-CMVNLS-copGFP-EF1-blastiS) via digestion. The product was then amplified via touchdown PCR, introducing the NotI and AgeI restriction sites, using the following forward and reverse primers, respectively: 5'-CAAGCGGCCGCACCATGACTGCTCCAAAGAAGAAGCG-3' and 5'-GCAACCGGTGCGAGATCCGGTGGAGCCGG-3'. Retroviral particles were produced via 293-GPG cell transfection with the plasmid and Lipofectamine 2000 (Invitrogen) following the manufacturer's protocol. Retrovirus-containing supernatants were collected once every 24 hours for 5 days following transfection and strained

through a 0.22  $\mu\text{m}$  filter. Cells were seeded into 6-well plates to reach 50-60% confluency on the day of infection, and were transduced with viral stock in the presence of 8  $\mu\text{g}/\text{mL}$  polybrene (Sigma-Aldrich) every 24 hours for three days. On the fourth day, the viral solution was replaced with fresh culture medium, and cells were cultured for three days before selection with puromycin. After selection, cells were sorted on a BD FACSAria Fusion fluorescence activated cell sorter (Cornell University Biotechnology Resource Center), and used for experiments or frozen down.

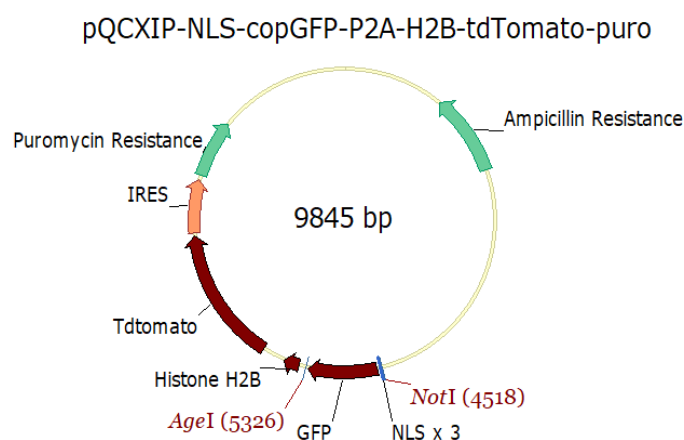


**Figure 3.3: Vector map of pQCXIP-NLS-copGFP-P2A-H2B-tdTomato-IRES-puro.** Plasmid map indicating location of selected markers and locations throughout retrovirus. The full plasmid sequence can be found in the appendix. Plasmid map created using Vector NTI<sup>®</sup> (Invitrogen).

*Automated Image Analysis Program:*

Automated image analysis begins by locating the constrictions in the first image (Fig. 3.4). The image is then processed to reduce noise and to detect fluorescently labeled

nuclei. For each subsequent image in the sequence, image stabilization is performed to account for small shifts in the field of view during image acquisition. Each image is then subject to the same processing as above to reduce noise and detect nuclei. Identified nuclei are tracked from the previous image to the current one. All nuclei are then observed for incidences of constriction passage and NE rupture. After the full sequence has been analyzed, the tracking results are exported to a spreadsheet and presented to the user for manual validation. The program was implemented in MATLAB 2016a and runs on all MATLAB supported platforms, version 2016a and newer. It can be downloaded at the following URL: <https://github.com/Lammerding/MATLAB-Cell-Tracking>.

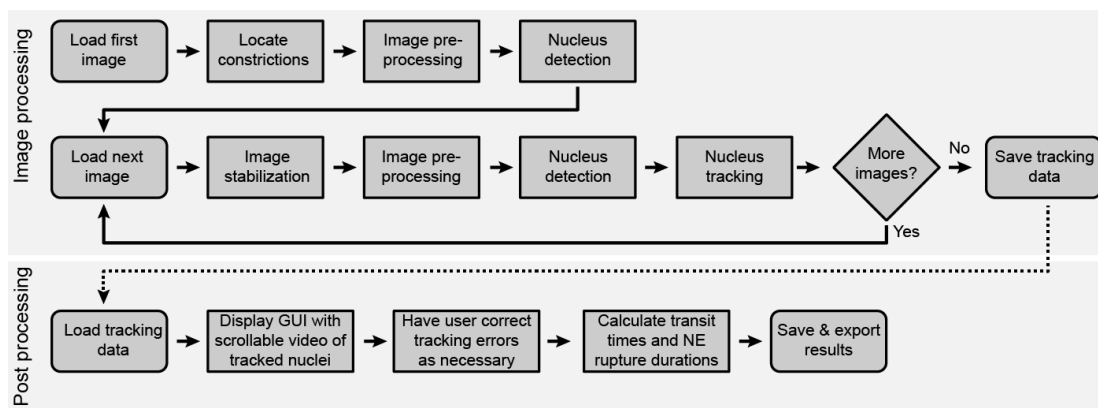


**Figure 3.4: Flowchart detailing steps program takes when analyzing an image sequence, including image processing (top) and post-processing (bottom).** Adapted from Elacqua et al. 2018.

*Locating Constrictions:*

Constriction location is performed by identifying the round pillars in the microfluidic

devices that form the three rows of constrictions (Fig. 3.5B). This is accomplished by applying a circular Hough transform to a transmitted light image of the device. All images are then rotated to align the rows of constrictions horizontally (Fig. 3.5C). Virtual boundaries are defined at a specific distance above and below the constriction centerline to determine nucleus entry and exit for each row of constrictions. (Fig. 3.5D). This approach can be adjusted for devices with different designs.

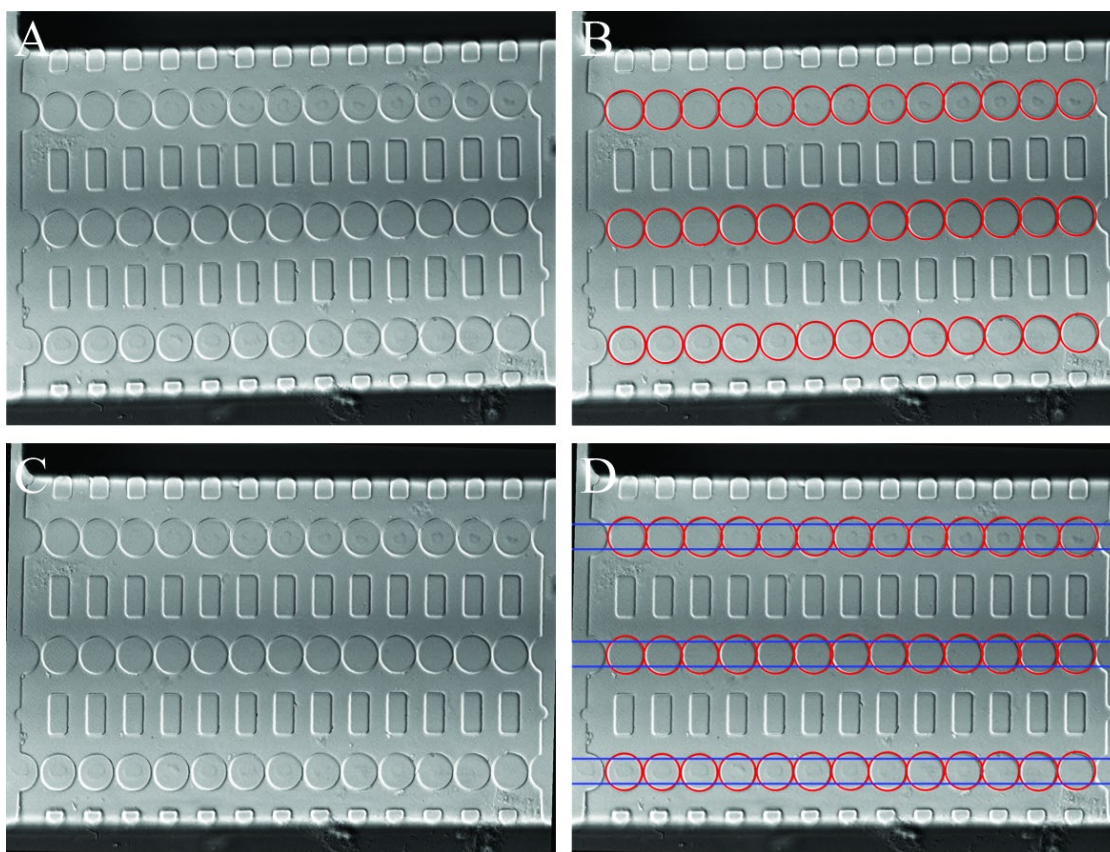


**Figure 3.5: Locating constrictions.** (A) Raw image of microfluidic device constrictions. (B) Constrictions are recognized using a circular Hough transform (red circles), and used to rotate the image to align the constrictions horizontally (C). (D) Boundaries (blue lines) for each row are identified using the recognized circles. When

a cell touches or crosses the blue line, it is recorded as ‘within the constrictions’. The cell remains ‘within the constrictions’ until it has crossed the top blue line identifying a row of constrictions. Figure adapted from Elacqua et al. 2018.

#### *Image Pre-Processing and Stabilization:*

To reduce the noise in the fluorescence images and enhance the contrast between the nuclear signals and the background, a  $10 \times 10$  pixel Gaussian filter is applied to the images of the fluorescence channels. Image stabilization is then performed via normalized 2D cross-correlation between an image and its predecessor. The obtained spatial offset values are applied to the transmitted light as well as the fluorescence image channels.

#### *Nucleus Detection:*

Nuclei are identified by binarizing images with a locally adaptive threshold based on their H2B-tdTomato signal and applying connected component analysis. Local thresholding, while more computationally expensive, provides better results than global thresholding, especially for unevenly illuminated images. To separate touching nuclei into distinct objects, further segmentation is necessary. Since nuclei are generally oval-shaped, the program uses watershed segmentation based on the distance transform of the identified nuclei. An H-minima transform is applied to the distance transform to prevent over-segmentation. Nuclei inside of constrictions are excluded from this segmentation since they take on a dumbbell shape, and otherwise may be incorrectly split into two objects. After image segmentation, identified objects are deleted if their properties, such

as size and circularity, suggest they are not nuclei (Fig. 3.6A, B).



**Figure 3.6: Nuclear identification and tracking.** (A) Merged image of the transmitted light and tdTomato channels. Nuclei (red) can be seen in the migration device. (B) Binarized version of red channel of image A. Each nucleus is identified as a separate object (white). (C) Example of tracking results. Nuclei (red) have been identified, and their centroid positions during migration are shown as yellow tracks. For clarity, tracks displayed here are limited to data for the last six hours only. Scale bar: 50  $\mu\text{m}$ . Figure adapted from Elacqua et al. 2018.

#### *Nucleus Tracking:*

After nuclei have been identified, they are tracked over time by recording their centroid position at each time point. The following error function is applied to every possible pairing of a nucleus in one image and a nucleus in the following image:

$$E = distance^2 + 2 \times |\Delta fluorescent\ intensity| + 2 \times |\Delta area|$$

This error function is related to the likelihood that two objects are the same nucleus and is based on the square of the distance between the centroids of the two objects. Since

comparing only the distances between objects produces inaccurate results when multiple nuclei are in close proximity, the error function also includes the change in each object's area and its average H2B-tdTomato fluorescent intensity. These values are expected to remain relatively constant over time for individual nuclei, but vary between different nuclei. The object from the previous time point and the object in the current time point that together have the lowest error function value are paired with one another and marked as unavailable for other pairings. Pairs can only be made if the centroids of the objects are within 40  $\mu\text{m}$  of one another, which is the maximum distance a cell typically travels within the chosen time interval. If necessary, the user can later correct this during the manual validation and editing stage, but we found that such instances are rare. Object pairing and marking availability status continues until no further object pairings are available. Upon completion, time-resolved data for each identified nucleus include centroid position, bounding box, area, and fluorescence intensity, which can be displayed for each nucleus (Fig. 3.6C) and used for further analysis.

*Detection of Transit through Constriction:*

The passage of nuclei through constrictions is evaluated as follows: if the top of a nucleus' bounding box is above the lower boundary of a constriction and the bottom of the nucleus' bounding box is below the upper boundary of the constriction, the nucleus is considered to be attempting to pass through the constriction. When an attempting nucleus moves completely above the upper bounding box, it is recorded as having successfully passed the constriction. A nucleus that is attempting to traverse a constriction but then moves back out of the boundary of the constriction is recorded as

failing to pass through the constriction. Nuclei that only briefly (1-time frame) attempt to enter a constriction are excluded from the analysis. Such instances can occur when a cell moves parallel to the row of constrictions and a part of the nucleus crosses the boundary of the constriction, without the cell attempting to pass through the constriction.

*NE Rupture Detection:*

NE rupture is detected by monitoring the inverse ratio of the nuclear NLS-GFP signal to the H2B-tdTomato signal. Since the total amount of NLS-GFP per cell stays approximately constant over time, and NLS-GFP spills into the cytoplasm during NE rupture, the average NLS-GFP nuclear intensity decreases during NE rupture. In contrast, the H2B-tdTomato signal remains nearly constant, allowing for normalization to the H2B-tdTomato signal. The normalization accounts for variations due to photobleaching and other image acquisition effects. The ratio of average H2B-tdTomato signal to average nuclear NLS-GFP signal [ $H2B/NLS$ ] is measured for each nucleus at every time point. If the difference in ratio between two consecutive time points [ $\Delta(H2B/NLS)$ ] exceeds 20% of the previous time point's ratio, or if the  $H2B/NLS$  ratio increases continuously over the course of at least 5 consecutive time points, then NE rupture is determined to have begun (Fig. 3.6A, red arrow). As the NE is repaired, NLS-GFP is re-entering the nucleus and  $\Delta(H2B/NLS)$  becomes negative. The NE rupture event is completed when the  $H2B/NLS$  ratio returns close to its pre-rupture value and  $\Delta(H2B/NLS)$  returns to zero (Fig. 3.7D).

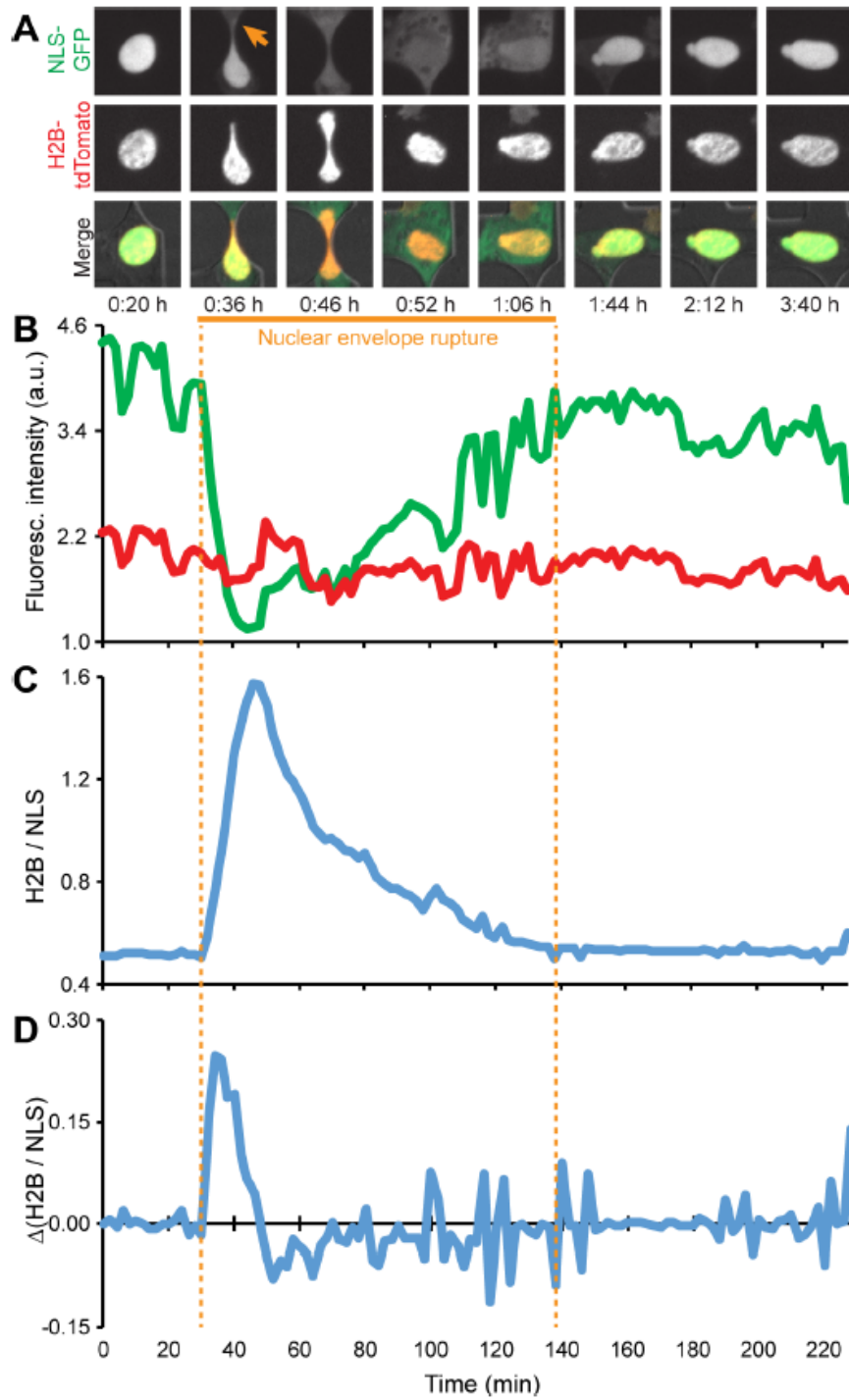


**Figure 3.7: Automated detection of NE rupture.** (A) During NE rupture (arrow), NLS-GFP (green) spreads throughout the cytoplasm, causing the nuclear NLS-GFP signal to lose intensity. In contrast, the H2B-tdTomato signal (red) remains

approximately constant. (B) Normalizing these two signals against one another (H2B/NLS) significantly reduces the effects of noise and allows for more accurate NE rupture detection. (C) Steep increases in the H2B/NLS ratio, which correspond to high values of  $\Delta(\text{H2B/NLS})$ , plotted in (D), indicate the start of a NE rupture event. The data shown here are for a representative cell. Figure adapted from Elacqua et al. 2018.

Since NE breakdown also occurs during mitosis, it is important to distinguish loss of nuclear NLS-GFP signals between mitotic cells and those exhibiting interphase NE rupture, in order to avoid false positive detection of NE rupture. Mitosis and NE rupture both begin with NLS-GFP spreading into the cytoplasm and are initially indistinguishable from one another. However, during mitosis, two daughter nuclei form from one initial nucleus. Thus, if a nucleus is detected as undergoing NE rupture, and a new nucleus appears in its vicinity in the next time point, the event is reclassified as mitosis, and not NE rupture.

#### *Manual Verification:*

Automated data analysis can misidentify events; therefore, a video for manual verification is generated for every image sequence analyzed. The video is displayed on a graphical user interface (GUI), and the user can manually select individual nuclei and events to make corrections as necessary. Recorded data is exported to a file after manual validation.

## **Results**

*Comparison of Automated and Manual Analysis:*

To assess the accuracy of the program, we acquired two image sequences of BT-549 breast cancer cells migrating through a microfluidic device with 2- $\mu\text{m}$  wide constrictions. The two image sequences were manually analyzed by four trained observers, recording constriction entry and exit times for each nucleus. One image sequence was used to “train” the automated image analysis program in order to define the boundaries that mark entry and exit of the nucleus in the constrictions. The program analyzed the video for six conditions, with constriction boundary lines placed either 5, 6, 7, 8, 9, or 10  $\mu\text{m}$  from the constriction centerline. Comparing the program’s results with the manual results revealed that placing the boundaries 7  $\mu\text{m}$  above and below the center produced the best agreement with the manual analysis.

The other image sequence was used to “test” the program and the 7  $\mu\text{m}$  constriction boundaries (Fig. 3.5). Comparison of the constriction transit times of individual cells determined by the program and four expert observers showed excellent agreement between the program and the manual gold-standard (Fig. 3.8). Similarly, the average constriction transit times computed by the program for each of the image sequences closely matched the data of the manual observers. Importantly, the program and all four observers correctly identified that cells overexpressing lamin A (less deformable nuclei) in the first image sequence had significantly ( $p < 0.05$ ) longer transit times than that of control lamin A cells in the second image sequence (Fig. 3.2).

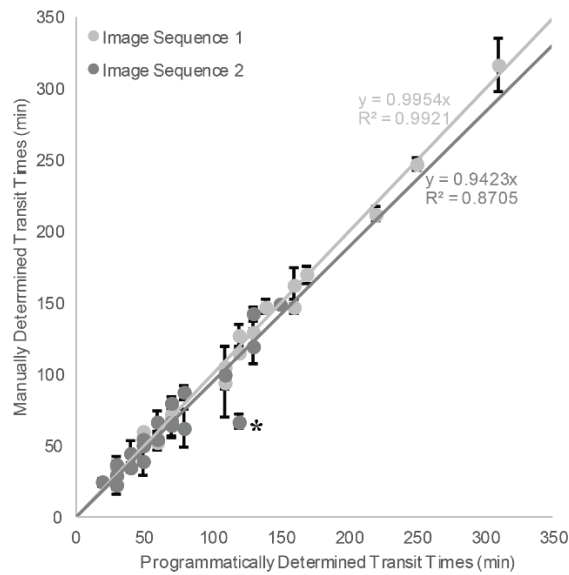


**Figure 3.8: Linear correlation of manual analysis and automated analysis.**

Automated analysis results plotted against manual analysis results (mean  $\pm$  s.e.m. from four analyst) for individual cells in two separate image sequences, each of which corresponds to a single section of a microfluidic device. For perfect agreement, the regression line plotted through these points would have a slope of one. Only one automated-analysis result substantially deviated from the manual reference, indicated by an asterisk. The manual analysis determined the nucleus to make two attempts to pass through the constriction, failing the first but succeeding the second time. The program identified this as a single, longer attempt. Figure adapted from Elacqua et al. 2018.

*Automated NE Rupture Analysis matches Median of Analyst Results:*

As seen in Figure 3.8, NE rupture duration varied substantially by analyst (gray bars). Interestingly, some cells experiencing NE rupture were not recognized and recorded by

all analyst (Fig. 3.9, red arrow). The variability present between individual analysts illustrates the lack of consistency, and provides evidence to that an automated platform providing reliable results would be necessary in order to analyze larger data sets.

Results of the automated NE rupture duration analysis (Fig. 3.9, black bars) recorded durations often in between the results of individual analyst, providing a consistent median value for NE rupture duration across recorded cells. Automated analysis also recognized NE rupture events that individual analyst missed, perhaps providing a more complete analysis of each experiment.

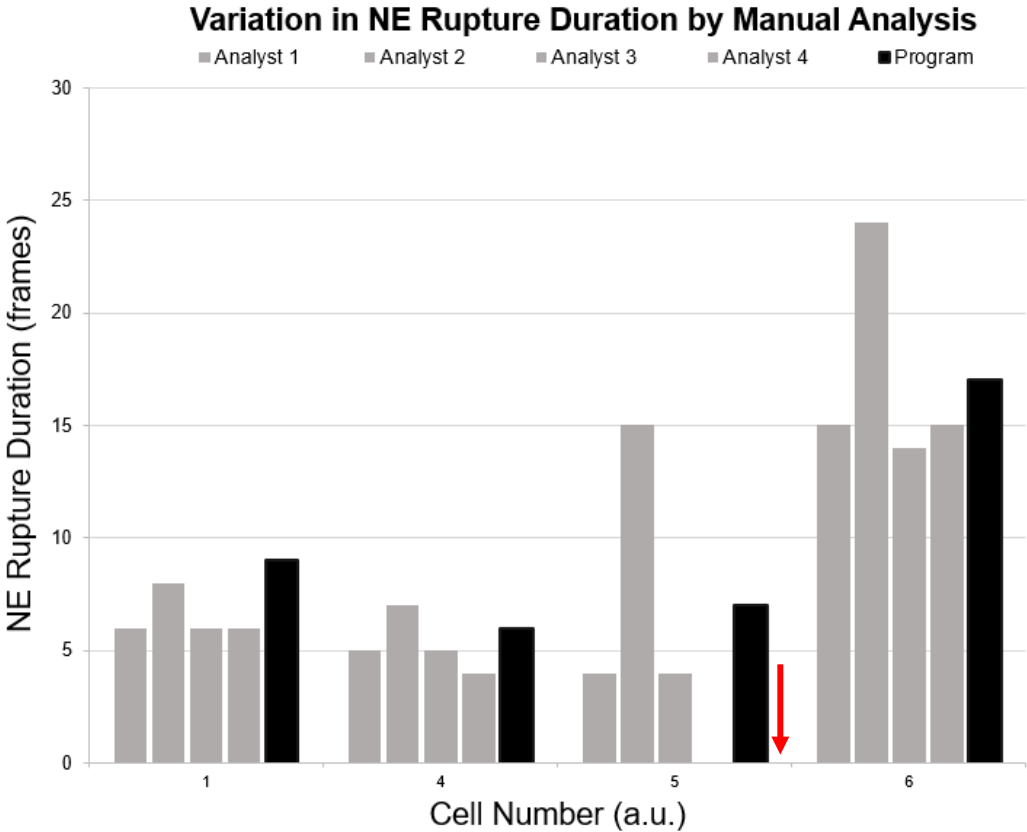


Figure 3.9: NE rupture duration manual analysis compared to automated analysis.

The manual recording of NE rupture duration often reveals differences between analysts. On occasion, manual analyst can miss a NE rupture event all together (red arrow). When using the automated analysis program, NE rupture duration measurements fall within the manual measured NE rupture duration variation, and eliminates person-to-person error that is found in manual analysis.

### **Discussion**

We have developed and validated a MATLAB program for the automated and robust analysis of nuclear activity as cells migrate through microfluidic devices. This automation reduces the amount of time required to analyze an image sequence from multiple days/weeks to ~5 hours for a time-lapse experiment with 24 positions/experimental conditions and over 100 frames per position. Before the development of our program, manual analysis was time-consuming and tedious, often leading to missed events (Fig. 3.9, red arrow) and variable measurements (Fig. 3.2 and 3.9). While manual analysis of nuclear transit time was relatively consistent across analysts, manual analysis of NE rupture varied substantially amongst analysts. When compared to manual analysis results, automated analysis values were consistent and precise, providing a new gold-standard for migration analysis (Fig. 3.8).

The program is suitable for a broad range of applications that use microfluidic devices to study the migration of cells through confined environments, including analysis of transit times through pores of different size, or incidence of NE rupture. Previously, collecting data on a large number of cell lines, patient samples, or treatment conditions

would have been impractical due to the substantial amount of time required to analyze the image sequences.

While the results presented here are based on a specific microfluidic migration device design, the modular nature of the program can be easily adapted to different design geometries, making it useful for a broad user base. Notably, the implemented automatic alignment and recognition of constrictions is independent of the constriction size and position.

The automated analysis is precise and robust enough to reach reliable conclusions concerning a population of cells' constriction transit times and NE rupture durations with only minimal user supervision. Furthermore, the program can generate and collect data that would be challenging to obtain through manual analysis. For example, the ability to collect pixel intensity values in specific areas of interest allows the program to monitor the intensity of fluorescence in every nucleus over time. This allows the actual time course of NE repair to be observed, recorded, and compared across populations of cells. In contrast, while manual analysis can record the duration of NE rupture events, it lacks the accuracy required to analyze the extent of repair at earlier time points.

This nucleus tracking program is currently used only to monitor constriction transit times and NE rupture events, but could readily be expanded to a broader array of applications. For example, measurements of nuclear migration persistence, i.e., the

tendency of the nucleus to move in a constant direction, could be recorded, since nucleus centroids are determined for each time point. Such an analysis would be extremely tedious and highly time-consuming if done manually. The automated analysis could also be expanded to include cell death detection, for example, based on the permanent loss of NLS-GFP intensity and unmatched nuclei after cell death. Automated cell death analysis could be useful for screening of drugs that target metastatic cancer cells. Additionally, the object identification and tracking elements of the program could be applied to any other set of time-lapse images, for example, to cells migrating on 2-D substrates or contact-printed micropatterns.

## CHAPTER 4: THE ROLE OF LAMIN A/C IN CONFINED CANCER CELL MIGRATION AND BREAST CANCER PROGRESSION<sup>4</sup>

### **Abstract**

Lamin A expression mediates nuclear deformability and migratory behavior (Davidson et al. 2014). Previous studies using human breast cancer tissue samples have shown that more aggressive samples express lower levels of lamins A and C (Capo-chichi et al. 2011; Wazir et al. 2013). Here, we examined whether lamin A/C expression correlates with increased migration potential and disease progression in breast cancer cell lines. Using a large panel of human and mouse breast cancer cell lines, we characterized the cells' lamin A/C expression and invasion capacity using Western blots and microfluidic migration device assays. Highly metastatic cancer cell lines had significantly lower levels of lamins A and C than less aggressive cancer cell lines and normal breast epithelial cells. Highly metastatic cell lines were also more successful at squeezing through confined microenvironments, indicating that the expression of lamin A/C may

---

<sup>4</sup> Portions of this work have been reproduced from the following publication:

Mekhdjian, A.J. †, Rubashkin, M.G. †, Kai, F., Prahl, L.P., **McGregor, A.L.**, Bell, E.S., Przybyla L.M., Barnes, M.J., Dufort, C.C., Ou, G., Chang, A.C., Cassereau, L., Tan, S.J., Pickup, M.W., Lakins, J.N., Yex, X., Davidson, M.W., Lammerding, J., Odde, D.J., Dunn, A.R., Weaver, V.M. (2017). Integrin-mediated traction force enhances paxillin molecular associations and adhesion dynamics that increase the invasiveness of tumor cells into a three-dimensional extracellular matrix, *Molecular Biology of the Cell* 28(11), 1467-88. † contributed equally.

Author contributions: ALM characterized migratory behavior of PyMT and Met1 cells in publication. EB ran Western blot to determine lamin expression in cell lines. ALM and EB carried out initial characterizations of cell lines. EB performed lamin A/C western blot and immunofluorescence and IF analysis on the human breast cancer panel, MCF10A progression series, and PyMT cells, while ALM performed lamin A/C WB analysis on the 4T1 progression series. All remaining work in chapter was performed by ALM.

play a role in the cells ability to metastasize. Providing additional evidence that lamin expression plays a major role in a cancer cells' invasiveness and metastatic potential.

## **Introduction**

In cancer cell metastasis, tumor cells break through the basement membrane, intravasate into the blood stream, extravasate out of the blood stream, and invade into a secondary site (Hanahan and Weinberg 2011). During invasion, cancer cells must squeeze through interstitial spaces ranging from 0.1 to 30- $\mu\text{m}$  in diameter, which is often significantly smaller than the size of the cell (Doerschuk et al. 1993; Stoitzner et al. 2002; Weigel, Bakker, and Friedl 2012). Cells have two strategies to penetrate confined environments: *(i)* expanding the openings via physical remodeling and/or proteolytic degradation of the ECM (Stetler-Stevenson et al. 1993), or *(ii)* contorting their shape to accommodate the available spaces (Wolf et al. 2003). When cells contort themselves to squeeze through available space, their ability to migrate is dependent on the nucleus (Davidson et al. 2014; Friedl et al. 2011; Harada et al. 2014; Wolf et al. 2013). As the largest and stiffest organelle in the cell, the nucleus is considered to be the rate-limiting step in cell migration (Balzer et al. 2012; Friedl et al. 2011; Fu et al. 2012; Lammerding 2011; Martins et al. 2012; Tong et al. 2012; Wolf et al. 2013). Spaces smaller than 5  $\mu\text{m}$  in diameter require substantial nuclear deformation for successful migration (Balzer et al. 2012; Davidson et al. 2014, 2015; Fu et al. 2012; Lautscham et al. 2015; Tong et al. 2012).

Nuclear stiffness is largely determined by lamin protein expression, with lamin A/C and not lamin B1, responsible for determining nuclear stiffness (Dahl et al. 2004, 2005; Lammerding et al. 2004, 2006). Recent reports indicate that altered lamin expression (rather than mutations) is found in many cancers, and often correlates with negative clinical outcomes as reviewed in Denais and Lammerding 2014; Hutchison 2014; Krause and Wolf 2015. Altered expression of lamins is considered a risk factor in cancer development of gastric, cervical, colon, and prostate cancers (Belt et al. 2011; Capochichi et al. 2015; Hutchison 2014; Khan et al. 2018; Moss et al. 1999; Willis et al. 2008). Reduced lamin A/C expression has been reported in breast cancer, and has been implicated in reduced disease free survival (Capochichi et al. 2011; Wazir et al. 2013). In contrast, increased A-type lamin expression is associated with disease progression in prostate, colon and ovarian cancers (Mitchell et al. 2015; Willis et al. 2008). Given the multiple functions of lamins, changes in their expression are expected to have pleiotropic effects, affecting not only nuclear stiffness (Chow et al. 2012a; Denais and Lammerding 2014; Hutchison 2014; Krause and Wolf 2015; Mitchell et al. 2015) but also regulator pathways involving cell adhesion proteins, extracellular matrix proteins, and cell metabolism.

Motivated by the knowledge that lamin A/C expression is often misregulated in many cancers, and is the major determinant of nuclear deformability, we examined whether variable lamin A/C expression correlated with increased migration potential and disease progression in breast cancer. Using a large panel of human and mouse breast cancer cell

lines, we characterized both the cells' lamin A/C expression and invasion capacity. Highly metastatic cancer cell lines had significantly lower levels of lamins A and C than less aggressive cancer cell lines, and normal breast epithelial cells. Of note, the highly metastatic cell lines were also more successful at squeezing through confined microenvironments.

## **Materials and Methods**

### *Breast Cancer Models:*

Four different cell line models of breast cancer progression were used throughout this study to assess differences in cell migration across cell lines with different metastatic potential—which is defined throughout this text as a cell that is capable of reaching a secondary site. These models were chosen based on their ability to represent cancer progression within the human body, and to represent a wide-array of the most common sub-types of breast cancer (Dai et al. 2017).

### *Polyoma Middle T Oncoprotein Mouse Breast Cancer Model:*

Transgenic mice carrying the mouse Polyoma Middle T antigen (PyMT) under the control of a mouse mammary tumor virus promotor have been shown to induce primary mammary tumors, as well as secondary, metastatic tumors (Guy et al. 1992). In our studies we used two cell lines extracted from transgenic PyMT mice. The control, tumorigenic PyMT cell line represents cells from the primary mammary tumor of a

PyMT transgenic mouse, whereas, the Met1 cell lines are a PyMT variant that has shown propensity to metastasize to secondary sites (Guy et al.1992; Lin et al. 2003).

*4T1 Mouse Isogenic Breast Cancer Progression Series:*

The 4T1 mouse model was isolated from a single, spontaneous mammary tumor in a BALB/cfC3H mouse (Dexter et al. 1978). Using a variety of separation and cell culture methods, four cell lines of variable metastatic capacity were established from a single mouse tumor. The 67NR cell line is unable to leave the primary tumor site when injected into BALB/c mice. The 168 FARN cell line is regularly found in lymph nodes, but rarely in the blood. 4T07 cells are regularly found in the lungs, but fail to proliferate, and are therefore not considered ‘metastatic’ due to their inability to form secondary tumors. The fourth cell line in the series, 4T1, consistently forms secondary lung and liver tumors (Aslakson et al. 1992). In addition to the cell lines established in this model, we used a normal mouse breast epithelial cell line, nMUNG, as a control.

	nMUNG	67NR	168FARN	4T07	4T1
Normal Epithelial Cells	+				
Primary Tumor		+	+	+	+
Lymph $\mu$ -metastases			+	+	+
Lung $\mu$ -metastases				+	+
Lung Large metastases					+

**Figure 4.2: 4T1 isogenic mouse breast cancer cell line model.** Four cell lines of variable metastatic capacity—67NR, 168 FARN, 4T07, and 4T1—were established from a spontaneous tumor in a BALB/cfC3H mouse. 67NR, 168 FARN, and 4T07 cell lines are considered nonmetastatic (unable to form secondary tumors), while the 4T1 cell line consistently forms secondary lung and liver tumors (Aslakson et al. 1992). nMUNG normal mouse breast epithelial cells are used as a control cell line not originating from the BALB/cfC3H mouse.

*MCF10A Human Isogenic Breast Cancer Progression Series:*

MCF10A cells were initially isolated from a female fibrocystic breast via mastectomy, extracted from the tissue via digestion, and then cultured following sedimentation (Soule et al. 1990). The MCF10A cells were then transfected with the *T24 c-Ha-ras* oncogene, and stably transformed to establish a new, pre-malignant cell line,

MCF10AT. MCF10AT cells were subcutaneously injected into immunocompromised mice, and formed squamous carcinomas. Cells isolated from these nodules were subcultured to create the MCF10AT1 cell line (Dawson et al. 1996). This process was repeated multiple times to create more aggressive tumors within the mice. Cells were isolated following the formation of new tumors, and established into cell lines—ultimately creating cell lines such as MCF10.CA1a and MCF10.CA1d that consistently form metastases, mimicking cancer progression *in vivo* (Fig. 4.1; Santner et al. 2001).

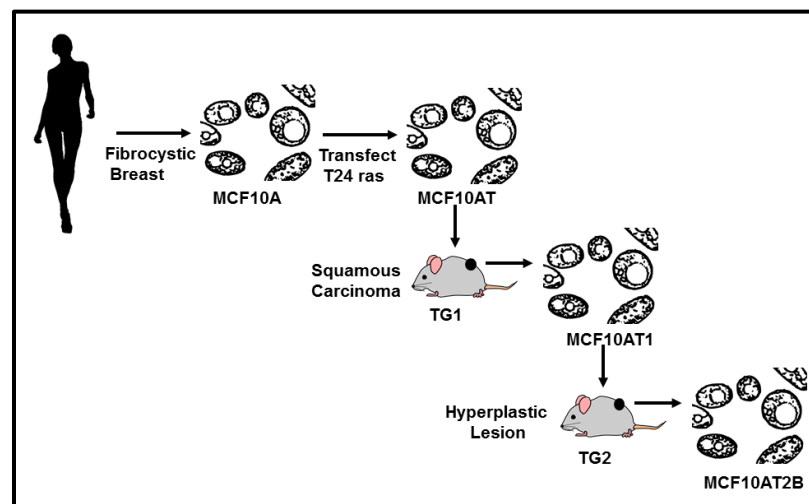


**Figure 4.1: MCF10A human isogenic breast cancer progression series.** Schematic illustrating the development of the MCF10A human isogenic breast cancer progression series from the tissue of a human fibrocystic breast sample into metastatic, aggressive cell lines. Adapted from Dawson et al., 1996.

*Human Breast Cancer Panel:*

While isogenic breast cancer cell line series provide models of cancer progression from cell that all share the same genetic origin, not all types of invasive and/or metastatic cells are represented by these models. Therefore, a panel of cell lines from four of the most common breast cancer subtypes was used to study and better understand how confined migration differs in cell lines representing an array of breast cancer subtypes.

Breast cancer is most often categorized based on the of expression and mutation state of estrogen receptor (ER), progesterone receptor (PR), and human epidermal growth factor receptor 2 (HER2). The presence or absence of each of these markers is an indicator of a tumor's genetic makeup, and enables physicians to identify how to treat each tumor most successfully. It can also be used to identify how aggressive a tumor is, or will become without treatment. Typically a tumor that does not express ER, PR, or HER2 is considered to have a poor prognosis, and is considered 'triple- negative.'

Luminal A breast cancer tumors are often identified before they have metastasized out of the breast, and make up 30-70 percent of breast cancer diagnoses (Annunzio 2012; Fan et al. 2006; Howlader et al. 2014; Voduc et al. 2010). Although luminal A tumors are the most common breast cancer diagnosed, these tumors tend to have the best prognosis and rarely recur after treatment (Arvold et al. 2011; Howlader et al. 2014; McGuire et al. 2017; Metzger-Filho et al. 2013; Voduc et al. 2010). Luminal A tumor cells express both ER and PR markers, but are HER2 negative. For the human breast

cancer panel, cell lines T47d and MCF7 were chosen to represent the luminal A sub-type of breast cancer.

HER2-positive (HER2+) breast cancer sub-type represents tumors that are ER and PR negative, but HER2 positive. These tumors tend to be more aggressive than luminal A and B subtypes, due to the overexpression of HER2, which causes increased cell proliferation, but less aggressive than basal-like and triple-negative subtypes (Dai et al. 2017; Metzger-Filho et al. 2013; Voduc et al. 2010). This sub-type is often treated with drugs such as Herceptin (Genentech), which were created specifically to target HER2+ cells. SK-BR-3 and BT474 cell lines were chosen to represent the HER2+ sub-type in the human breast cancer panel.

The basal-like breast cancer sub-type is defined by cells that are similar to outer basal cells surrounding the mammary duct. Basal-like tumors often do not express ER, PR, and HER2; although this is not always the case—causing the classification of basal-like tumors to occasionally vary. Cells in a basal-like tumor may also include expression of one or more basal cytokeratins such as CK5/6, CK14, and CK17 (Badve et al. 2011). Basal-like tumors are often found in younger women, and African-American women, and have a poor prognosis (Kohler et al. 2015; Partridge et al. 2016; Sineshaw et al. 2014). MDA-MB-468 and HCC70 were chosen as the cell lines to represent the basal-like sub-type in the human breast cancer panel.

Similar to the basal-like subgroup classification, claudin-low tumors are considered a distinct breast cancer sub-type, although the precise definition still varies. The claudin-low sub-type is defined by tumor cells that express low levels of claudins, which are important proteins that make up tight junctions expressed between epithelial cells (Herschkowitz et al. 2007). These tumors are known to lack claudin 3, 4, and 7—and even E-cadherin (Dias et al. 2017). Claudin-low tumors are typically triple-negative, but not always, and are often invasive (Dias et al. 2017). MDA-MB-231 and BT-549 cell lines were used to represent the claudin-low breast cancer sub-type in the human breast cancer panel model.

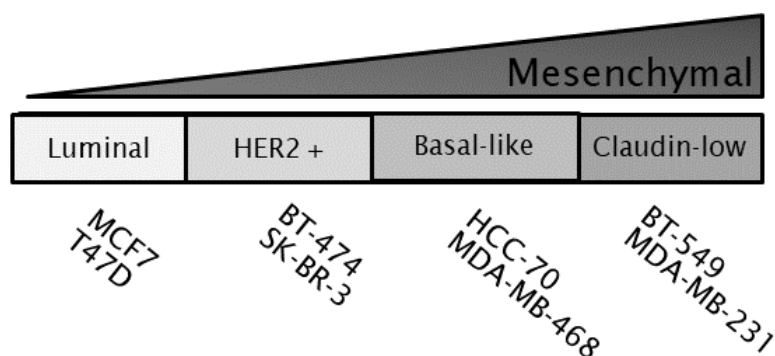


**Figure 4.3: Human breast cancer cell line panel.** Eight cell lines representing four of the most common human breast cancer sub-types were used to characterize the role of lamins in various human breast cancer tumors. Luminal A breast cancer sub-types were represented using cell lines MCF7 and T47D. HER2-positive cell lines, BT-474 and SK-BR-3, represent a more aggressive form of breast cancer than luminal A and B sub-types. HCC-70 and MDA-MB-468 cell lines were chosen to represent the basal-like breast cancer sub-type, while BT-549 and MDA-MB-231 were chosen to represent the

claudin-low sub-type of breast cancer. Both basal-like and claudin-low sub-types tend to be triple-negative tumors that are more aggressive and have a poor prognosis.

*Cell Culture Techniques:*

Polyoma Middle T Oncoprotein Mouse Breast Cancer Model cell lines PyMT and Met1 were a generous gift from Dr. Valerie Weaver (UCSF Helen Diller Comprehensive Cancer Center, University of California, San Francisco, San Francisco, CA). Cells were maintained in Dulbecco's Modified Eagle's Medium: Nutrient Mixture F-12 (DMEM/F12; Gibco) media supplemented with 10% FBS (VWR), and 1% Pen/Strep (Gibco).

4T1 mouse isogenic breast cancer series cell lines, nMUNG, 67NR, 168 FARN, 4T07, and 4T1, were a generous gift from Dr. Peter Friedl (St. Radboud University Nijmegen Medical Centre, University of Nijmegen, The Netherlands and MD Anderson Cancer Center, Houston, TX, USA). nMUNG, 67NR, 168 FARN, 4T07, and 4T1 cell lines were maintained in Roswell Park Memorial Institute medium (RPMI, Gibco) supplemented with L-glutamine (Gibco), sodium pyruvate, 10% FBS (VWR), and 1% Pen/Strep (Gibco).

MCF10A human isogenic breast cancer progression series cell lines were a generous gift from Dr. Valerie Weaver (UCSF Helen Diller Comprehensive Cancer Center,

University of California, San Francisco, San Francisco, CA). MCF10A and MCF10AT cell lines were maintained in DMEM/F12 (Gibco) media supplemented with 5% horse serum (HS; VWR), 1% Pen/Strep (Gibco), 20 ng/ml EGF (Goldbio), 0.5mg/ml hydrocortisone (Sigma Aldrich), 100ng/ml cholera toxin (Sigma Aldrich), and 10ug/ml insulin (Gemini Bio Products). MCF10A.CA1a and MCF10A.CA1d cell lines were maintained in DMEM/F12 (Gibco) media supplemented with 5% HS (VWR), 1% Pen/Strep (Gibco), 1.05 mM CaCl<sub>2</sub> (Sigma), and 1mM HEPES (Gibco).

Human breast cancer panel cell lines MDA-MB-231, MDA-MB-468, MCF7, SK-BR-3 were obtained from the American Type Culture Collection (ATCC), and grown in DMEM (Gibco) supplemented with L-glutamine, 10% FBS (VWR), and 1% Pen/Strep (Gibco). Human breast cancer cell lines BT-549, BT-474, and T47D were obtained from ATCC, and grown in RPMI (Gibco) medium supplemented with L-glutamine, 10% FBS (VWR), and 1% Pen/Strep (Gibco).

All cells were cultured at 37° C, and 5% CO<sub>2</sub>.

#### *Generation of Fluorescently Labelled Cell Lines:*

Retroviral vector (pQCXIP-NLS-copGFP-P2A-H2B-tdTomato-IRES-puro, System Biosciences) was used to stably modify cells to co-express both NLS-GFP and H2B-tdTomato as described previously (Elacqua et al. 2018, see Chapter 3 of this thesis). In

brief, fluorophores attached to proteins and sequences of interest were ligated into the digested pQCXIP vector backbone. Colonies of interest were collected and sequenced. Retroviral particles were produced in 293-GPG cells from successful clones, and collected and purified every 24 hours for 5 days following transfection. Cells were transduced with viral stock and 8  $\mu\text{g}/\text{mL}$  polybrene (Sigma Aldrich) every 24 hours for three days. Cells underwent selection with puromycin 3 days following viral transduction, and sorted using a BD FACSARIA FUSION fluorescence activated cell sorter (Cornell University Biotechnology Resource Center), for cells that expressed both fluorophores.

*Microfluidic Device Preparation:*

Microfluidic devices fabricated via 2-layer SU-8 photolithography were used to create PDMS (Dow-Corning) replicates as described previously (Davidson et al., 2015). PDMS stamps of microfluidic devices were covalently attached to glass coverslips via plasma cleaning (Harrick Plasma), and covalent bonds were enhanced via a short 5-minute heat incubation. Devices were washed with 70% ethanol and water, coated with 50  $\mu\text{g}/\text{mL}$  rat tail collagen type I (Corning) diluted in 0.02 M glacial acetic acid (Sigma), and incubated overnight at 4°C.

*Cell Seeding in Migration Devices:*

All cell lines were seeded 7-8 hours before imaging at a density of at 30,000 cells/device in 6  $\mu$ l of media. SK-BR-3 cells were seeded 24 hours before imaging at a density of 30,000 cells/device due to their slow attachment. After two hours of cell attachment, media was removed and an FBS gradient was established (0 to 10%).

*Time-Lapse Imaging:*

Immediately before imaging, media was changed to phenol-red free or Fluorobrite medium (Gibco) supplemented with 25 mM HEPES (Gibco) at a 0 to 10% FBS (VWR) gradient. Migration devices were sealed with a coverslip, and loaded into a custom-made holder on a laser scanning confocal microscope (LSM 700, Zeiss). Cells were maintained on a temperature-controlled stage at 37°C overnight, and images were acquired at 20 $\times$  magnification (NA 0.8 air objective) every 10 minutes with a CoolSNAP EZ CCD camera (Photometrics) until at least 100 time points had been acquired. Zen software (Zeiss) was used to automate image acquisition, Images of the migration device and cells were acquired with differential interference contrast (DIC); fluorescence microscopy was used to capture the NLS-GFP signal (excitation with 450-490 nm light, collection of emission at 500-550 nm; exposure time of 75 ms), and the H2B-tdTomato signal (excitation by 550-580 nm light, collection of 590-650 nm light; exposure time of 400 ms). All images were saved in the Carl Zeiss Image (.czi) format.

*Transit Time Analysis:*

Overnight time-lapse migration experiments were analyzed using an automated migration analysis program in MATLAB described in detail in Chapter 2 (Elacqua et al. 2018). From the data acquired, transit success rate (in percent) was determined by dividing the number of cells that successfully migrated through a constriction by the total number of cells that attempted to migrate through the constrictions. Transit times were calculated by averaging the total time of successful transits per constriction size or each cell line.

#### *Western Blot:*

Western blots were performed using cell lysates to quantify lamin A/C protein levels. Samples were prepared from confluent 6 well-plates, and were lysed in high salt (750 mM) RIPA buffer supplemented with cOmplete, EDTA-Free proteinase inhibitor (1 $\times$ ; Roche). Lysed samples were vortexed, boiled, and centrifuged. Protein content was measured using standard Bradford assay techniques. For each sample, 25  $\mu$ g of total protein were run on 4-10% Bis-Tris NuPage gels (Gibco) with MOPS buffer at a voltage of 175 V for 45 minutes. Following gel electrophoresis, Immobilon-FL transfer membranes (Gibco) were activated in methanol for 1 minute, neutralized in transfer buffer along with blotting paper and the gel, and were assembled into a transfer sandwich. Transfers were performed on a trans-blot SD semi-dry transfer cell (Bio-Rad) for 1 hour at 16 V. Membranes were then blocked in 3% BSA in TBST for one hour. Primary antibodies (anti-lamin A/C clone E-1, Santa Cruz, dilution 1:1000; anti-histone H3, Cell Signaling, dilution 1:5000; anti- $\beta$ -tubulin, Sigma, dilution 1:4000; anti-Actin,

Santa Cruz, dilution 1:5000) were diluted in 3% BSA in TBST and incubated overnight at 4° C. Secondary antibodies (donkey anti-mouse 680 and donkey anti-rabbit 800, Licor, dilution 1:1000) were diluted in 3% BSA in TBST and incubated for one hour at room temperature. All membranes were imaged using the LI-COR Odyssey CLx.

#### *Statistical Analysis:*

Transit times from individual cells were combined for all experiments, and a non-parametric one-way ANOVA with Dunn's multiple comparison post-test was performed to determine statistical significance. Transit success rates were determined by taking the mean of the average success rate of each experiment), and a non-parametric one-way ANOVA with Dunn's multiple comparison post-test was performed to determine any statistical significance. All data are based on at least three independent experiments.

Protein expression in Western blots was quantified, and normalized in respect to a protein control. Differences between cell line protein expression were expressed relative to a control cell line, and differences were determined via a one-way ANOVA. All data are based on at least three independent experiments.

## **Results**

*Lamin A and C Expression in Mouse and Human Breast Cancer Models Varies with Metastatic Potential:*

Previous work using human breast cancer tissue samples has shown that more aggressive samples express lower levels of lamins A and C (Capo-chichi et al. 2011; Wazir et al. 2013). We examined whether variable lamin A/C expression correlated with increased migration potential and disease progression in breast cancer cell lines by probing for lamin A and C expression using Western blots.

When comparing noninvasive PyMT and metastatic Met1 cell lines from the PyMT isogenic mouse breast cancer model, noninvasive PyMT cells had significantly higher expression of both lamin A and C protein than its Met1 metastatic counterpart (Fig. 4.4). Similarly, the 4T1 mouse isogenic breast cancer progression series displayed a decrease in lamin A expression with an increase in metastatic potential (Fig. 4.5). Specifically, nonmetastatic, 67NR cells had at least three-times higher lamin A expression than 168 FARN ( $3.2\times$ ;  $p < 0.01$ ), 4T07 ( $4.1\times$ ,  $p < 0.001$ ), and 4T1 ( $6.4\times$ ;  $p < 0.001$ ) cell lines. Control nMUNG epithelial cells also had significantly higher lamin A expression than both the 4T07 and 4T1 cell lines ( $p < 0.05$ ). While lamin A expression varied with metastatic potential, lamin C expression did not significantly vary amongst the 4T1 mouse isogenic breast cancer progression series cell lines (Fig. 4.5A).

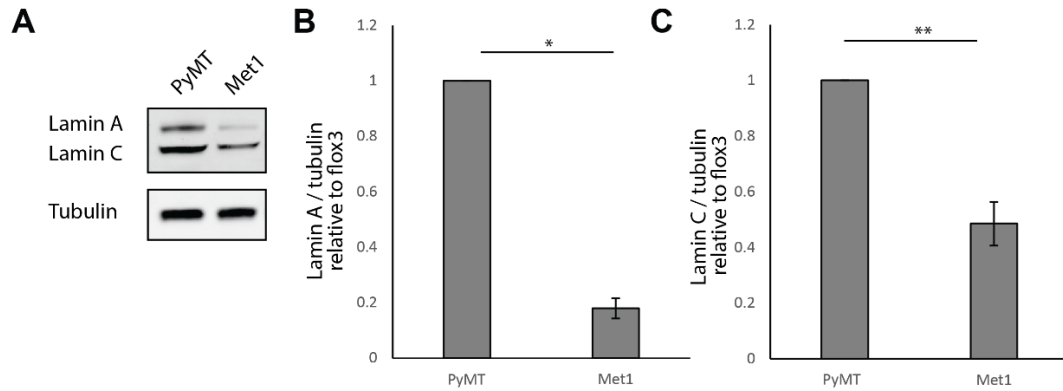


**Figure 4.4: Lamin A and C levels in highly-aggressive Met1 mouse cells, and their non-aggressive, tumorigenic predecessor PyMT mouse cells.** (A) Representative image of Western blot of lamin A and C protein lysates in PyMT and Met1 cells. Visual inspection reveals lower lamin A/C expression in Met1 invasive cells as compared to the PyMT control cells. (B) Quantification of lamin A levels, normalized to tubulin loading control. (C) Quantification of lamin C levels, normalized to tubulin loading control. Error bars reflect standard error of the mean. (\*,  $p < 0.05$ ; \*\*,  $p < 0.01$ , by *t*-test from four independent blots.) Data provided by Emily Bell.

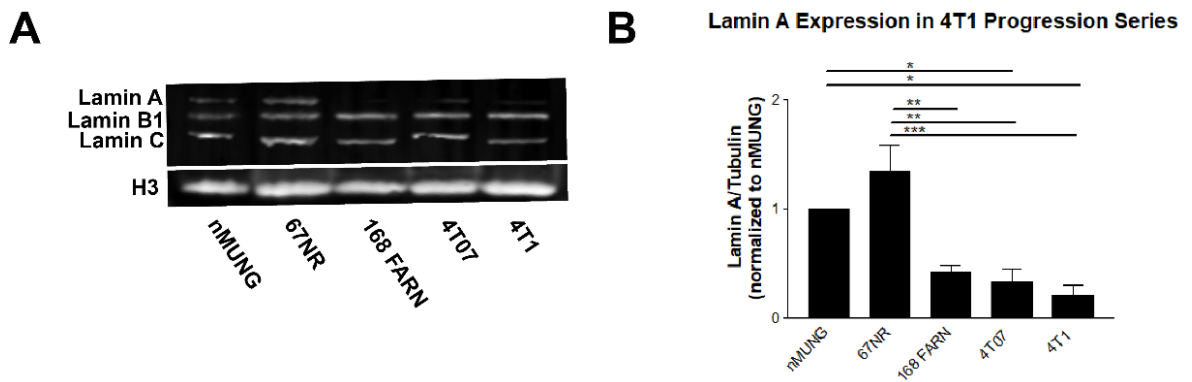


**Figure 4.5: Lamin A/C and B1 expression in the 4T1 mouse breast cancer progression series.** (A) Representative Western blot for lamin A/C and lamin B1 in 4T1 mouse model cell lines, with histone H3 used as loading control. (B) Quantitative analysis of Lamin A Western blot results, normalized to histone H3 loading control, and relative to nMUNG control breast epithelial cell line. Mean  $\pm$  standard error of the mean from three independent blots (\*,  $p < 0.05$ ; \*\*,  $p < 0.01$ , \*\*\*,  $p < 0.001$ , by one-way Anova with Tukey's Multiple Comparison post-test.)

To confirm our findings in human breast cancer cell lines, we examined lamin A/C levels in the the MCF10A human isogenic progression series. In this model, we did not observe any significant differences in lamin A/C expression (Fig. 4.6). This unexpected finding may be associated with the development of the cell line model. MCF10A cells were initially transformed with the *T24 c-Ha-ras* mutation. This is an uncommon driver mutation in breast cancer progression, and is not representative of a spontaneously arising, or common, mutation found in breast cancer, perhaps explaining the lack of lamin A/C variation in this model.

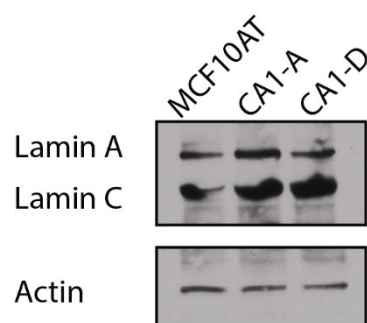


**Figure 4.6: Lamin A/C expression in the MCF10A isogenic breast cancer progression series.** (A) Representative Western blot for lamin A/C in MCF10A cell lines, with Actin used as a loading control. Blot courtesy of Emily Bell.

In contrast to the MCF10A model, in the human breast cancer cell line model lamin A expression followed a similar trend as in the 4T1 progression model, with the most metastatic cell lines having the lowest expression of lamin A (Fig. 4.7B and Fig.4.7D, MDA-231 and BT-549). One exception to this trend was seen in the basal-like sub-type cell lines, HCC70 and MDA-MB-468. Although these cells are considered moderately aggressive, they expressed the highest levels of lamin A in the human breast cancer panel (Fig. 4.7B). While the reason for this is not clear, it is possible that the basal-like cell lines, which express cytokeratins, use different mechanisms during migration and invasion (Badve et al. 2011). Differences in lamin C expression in the human breast cancer panel were not statistically significant across the cell lines, though it followed similar expression trends to that of lamin A expression (Fig. 4.7C).

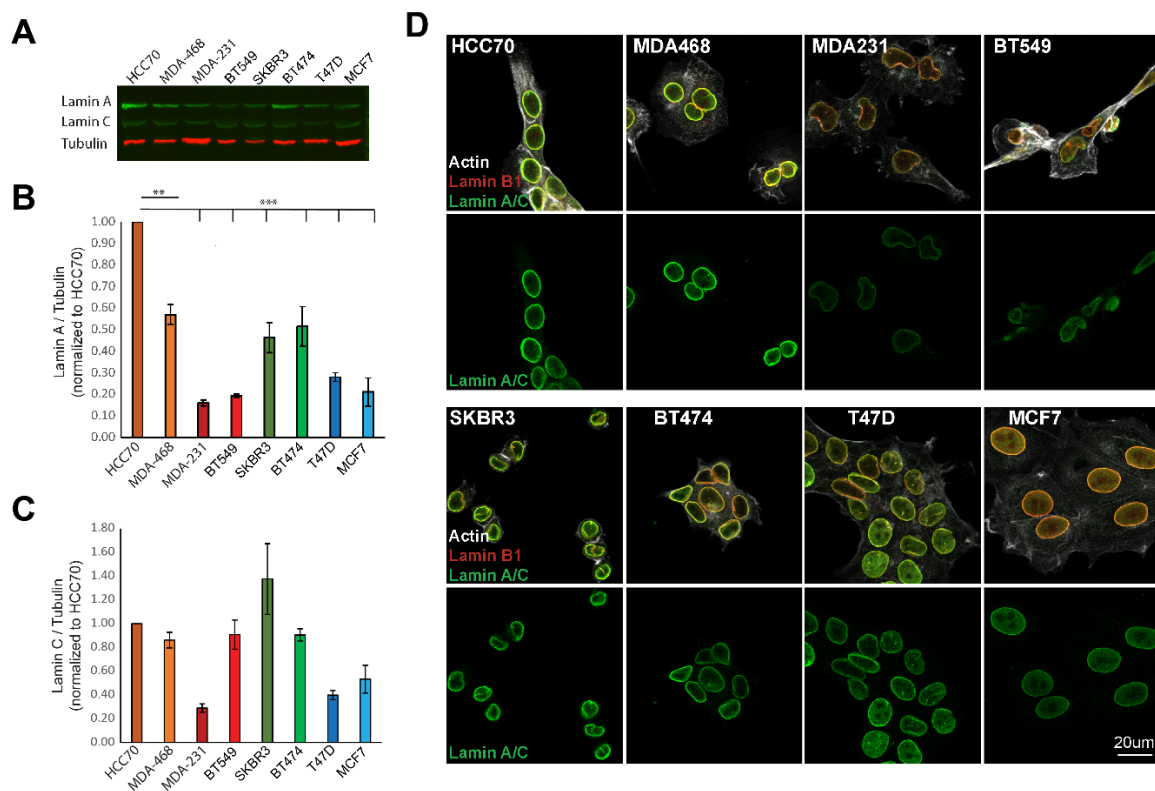


**Figure 4.7: Lamin A and C levels in human breast cancer panel cell lines.** (A) Representative lamin A/C Western blot for human breast cancer panel cell lines, with tubulin as loading control. (B) Analysis of Lamin A Western blot results, normalized to tubulin loading control. Lamin A expression is shown relative to HCC70 cell line, which had the highest expression of lamin A. (C) Analysis of Lamin C Western blot results, normalized to tubulin loading control. Lamin C expression is shown relative to HCC70 cell line. (D) Immunofluorescence images of human breast cancer panel cell lines, illustrating cell line lamin A/C expression variability. Images courtesy of Emily Bell. Mean  $\pm$  standard error of the mean from three independent blots (\*\*,  $p < 0.01$ ; \*\*\*,  $p < 0.001$ , based on one-way ANOVA with Tukey's Multiple Comparison post-test.)

*Cells with lower Lamin A/C Expression Migrate Through Confined Spaces Quicker Than Cells With Higher Lamin A/C Expression:*

During non-proteolytic cell migration, cancer cells must squeeze through spaces smaller than the nucleus (Krause and Wolf 2015; Katarina Wolf et al. 2013). Nuclear rigidity plays a role in the cells ability to squeeze through confined spaces, and is governed by nuclear stiffness, which in turn is determined by lamin expression and chromatin condensation (Dahl et al. 2004, 2005; Friedl et al. 2011). Previous studies in mouse fibroblasts have identified lamin expression as a rate-limiting step in cell migration (Davidson et al. 2014). Such trends in breast cancer progression are not yet well understood. We hypothesized that more metastatic cells with lower lamin expression, and thus more deformable nuclei, would migrate through the confined spaces of our microfluidic devices quicker and more successfully.

In the PyMT mouse breast cancer model, lamin A/C expression in PyMT cells was much higher than that of its Met1 metastatic counterpart (Fig. 4.1). When observing cell migration through confined microenvironments ( $\leq 2 \times 5 \mu\text{m}^2$  constrictions), PyMT cells migrated through the constrictions significantly slower than their more aggressive Met1 counterpart (Fig. 4.8A-C). One possible explanation may be that nuclei of PyMT cells are less deformable than those of Met1 cells, due to their higher lamin A/C expression, thus resulting in slower migration through tight spaces.

Similarly, when comparing transit success rate (i.e., the ability for cells to migrate past the first set of microconstrictions within migration devices), Met1 cells successfully crossed the first constriction almost twice as often as control PyMT cells (Fig. 4.8D).

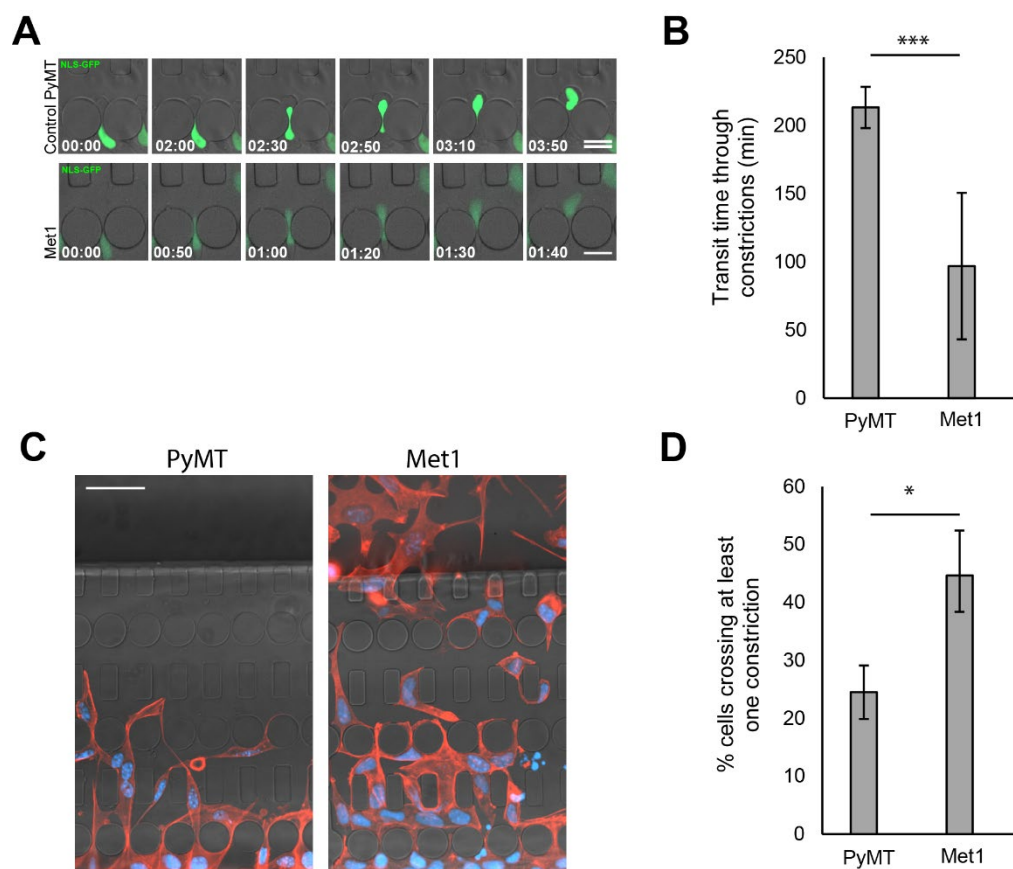


**Figure 4.8: Met1 cells display enhanced migration through microconstrictions.** (A) Representative time-lapse image sequences of PyMT cells and Met1 cells migrating through a  $1 \times 5 \mu\text{m}^2$  constriction inside microfluidic device. Cells expressed NLS-GFP to visualize the nucleus. Time displayed as hours:minutes. Scale bar:  $20 \mu\text{m}$ . (B) Transit times for cell passage through constrictions  $\leq 10 \mu\text{m}^2$  in cross-sectional area, illustrating that Met1 cells migrated faster through small constrictions. Mean  $\pm$  SEM (\*,  $p < 0.05$ ; \*\*\*,  $p < 0.001$ , by Kruskal–Wallis test with Dunn’s multiple comparisons;  $n > 70$  cells

from three independent experiments). (C) Representative images of cells inside the microfluidic devices after 48 h of confined migration. Fixed cells were stained for F-actin (phalloidin) and DNA (Hoechst 33342). Scale bar: 50  $\mu\text{m}$ . (D) Incidence of cells successfully migrating through the first row of constrictions within 36 hours of seeding, relative to the total number of cells inside the microfluidic channels. Error bars represent standard error of the binomial distribution (\*,  $p < 0.05$ ; \*\*\*,  $p < 0.001$ ;  $n > 500$  cells by Fisher's exact test with Bonferroni correction). Image adapted from Mekhdjian et al. 2017.

Although intriguing, it was important to confirm the mouse polyoma middle T findings in a more expansive set of human cell lines. Using cell lines from the human breast cancer panel, we observed cell migration through microfluidic devices. (Of note: the HCC70 cell line was not included in these experiments following multiple failed attempts to transform cells with NLS-GFP or/and H2B-tdTomato using both lenti- and retrovirus.)

Luminal A and HER2<sup>+</sup> cell lines had difficulty transiting through migration devices, particularly the confined constrictions. Successful transit across a confined constriction only occurred 16 times *combined* between the T47D, SK-BR-3, and BT474 cell lines, making the data difficult to interpret. Similarly, small numbers were observed for control cell migration (15  $\mu\text{m}$  wide constrictions that do not require nuclear deformation) in these cell lines. This lack of cell migration may be due to both Luminal

A and HER2+ breast cancer sub-types having higher levels of lamin A expression, being low-risk tumors on average, and representing more epithelial cell morphology.

One luminal A cell line, MCF7, migrated substantially slower through 1- and 2- $\mu$ m wide confined constrictions than its more metastatic counterpart, BT-549 ( $149.4 \pm 22.5$  minutes vs.  $76.41 \pm 6.2$  minutes; Fig. 4.9A), though lamin A expression was not statistically different between the two cell lines. While not often successful at migrating, the T47D cells that successfully squeezed through 1- and 2- $\mu$ m constrictions did so at a transit time not significantly different than either claudin-low cell line ( $81.4 \pm 15.2$  minutes vs.  $76.41 \pm 6.2$  minutes and  $101.2 \pm 6.6$  minutes, respectively; Fig. 4.9A). Since these cells had a very low ( $2.439\% \pm 2.439\%$ ) migration success rate in confined spaces, the transit time of these select T47D cells that did migrate through the constrictions may be indicative of a small sub-population of migratory cells within the overall population.

Claudin-low and basal-like breast cancers are considered highly metastatic. Claudin-low cells expressed the lowest levels of lamin A in the human breast cancer panel (Fig. 4.7B, red), while basal-like cells expressed the highest levels of lamin A (Fig. 4.7B, orange). As expected, the BT-549 cells with low lamin A expression migrated significantly faster than high expressing MDA-MB-468 cells ( $76.41 \pm 6.2$  minutes vs.  $118.2 \pm 9.5$  minutes, respectively; Fig. 4.9A).

In unconfined, i.e.,  $15 \times 5 \mu\text{m}^2$  large constrictions, cell migration, transit rates were variable across cell lines. While some migration transit times were significantly different, these differences appeared independent of lamin A expression, and metastatic potential. MCF7 cells migrated significantly slower than the four other cells lines, including both claudin-low cell lines and a luminal A cell line, which all had similar lamin A expression. MCF7s were also slower at migrating through the 15- $\mu\text{m}$  wide control channels than basal-like cell line, MDA-MB-468, which had the highest lamin A expression of all cell lines in the panel (Fig. 4.9B).

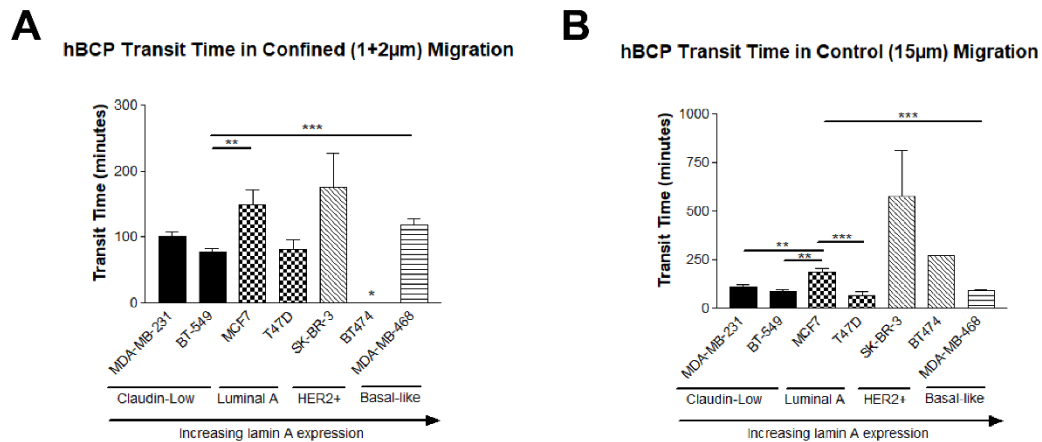


**Figure 4.9: Transit time for human breast cancer panel cell lines in confined and control constrictions.** Cell lines arranged in order of increasing lamin A expression. Filled black bars represent claudin-low, highly metastatic cell lines. Checker filled bars represent breast cancer luminal A sub-type cell lines, diagonal filled bars represent HER2+ cell lines, and horizontal filled bars represent basal-like cell lines. (A) Average transit time for successful migration through confined constriction (1 + 2  $\mu\text{m}$  width). Mean  $\pm$  SEM (\*\*,  $p < 0.01$ ; \*\*\*,  $p < 0.001$ , by one-way ANOVA with Dunn’s multiple

comparison test;  $n = 234$  for MDA-MB-231 cells;  $n =$  for 142 BT-549 cells;  $n = 35$  for MCF7 cells;  $n = 11$  for T47D cells;  $n = 5$  for SK-BR-3 cells;  $*n = 0$  for BT474 cells;  $n = 160$  for MDA-MB-468 cells; from at least three independent experiments per cell line ( $N = 5$  for MDA-MB-231;  $N = 3$  for BT-549;  $N = 3$  for MCF7;  $N = 3$  for T47D (additional experiments had no successful cell migration through constrictions);  $N = 7$  for SK-BR-3;  $N = 6$  for BT474 (additional experiments had no successful cell migration through constrictions);  $N = 5$  for MDA-MB-468). (B) Average transit time for successful migration through control constriction ( $15 \mu\text{m}$ ). (\*\*,  $p < 0.01$ ; \*\*\*,  $p < 0.001$ , by one-way ANOVA with Dunn's multiple comparison test;  $n = 102$  for MDA-MB-231 cells;  $n = 75$  for BT-549 cells;  $n =$  for 35 MCF7 cells;  $n = 13$  for T47D cells;  $n = 2$  for SK-BR-3 cells;  $n = 1$  for BT474 cells;  $n = 101$  for MDA-MB-468 cells; from at least three independent experiments per cell line ( $N = 5$  for MDA-MB-231;  $N = 3$  for BT-549;  $N = 3$  for MCF7;  $N = 3$  for T47D (additional experiments had no successful cell migration through constrictions);  $N = 7$  for SK-BR-3;  $N = 6$  for BT474 (additional experiments had no successful cell migration through constrictions);  $N = 5$  for MDA-MB-468).

When observing the success rate of cells migrating through confined constrictions, differences between sub-types of different metastatic potential were quite substantial (Fig. 4.10). The claudin-low cell lines were at least 4-times more successful at migrating through 1 and 2- $\mu\text{m}$  wide constrictions than their less metastatic counterparts (Fig 4.10A). The basal-like cell line, MDA-MB-468, was successful at migrating through

confined constrictions  $15.13 \pm 2.356$  % (Fig 4.10A), despite its high lamin A expression. In contrast, the HER2+ cell lines struggled to migrate through constrictions, with SK-BR-3 cells successfully migrating through a 1- or 2- $\mu\text{m}$  constriction only  $3.75 \pm 2.848$ % of the time. Despite multiple attempts, BT474 cells never successfully crossed the 1- or 2- $\mu\text{m}$  constrictions, resulting in 0% successful migration (Fig. 4.10A\*).

Luminal A cell lines also struggled to successfully migrate through constrictions, with T47D cells being successful only  $2.439 \pm 2.439$  % of the time. Although slow, MCF7 cells were more successful migrating through confined spaces than T47D, ultimately being successful  $10.92 \pm 2.955$  % of the time.

Migration success rates through 15- $\mu\text{m}$  wide control migration channels revealed similar results. Claudin-low cell lines were much more likely to successfully migrate, when compared to luminal A or HER2+ cell lines (Fig. 4.10B). However, the basal-like cell line, MDA-MB-468, was just as successful at migrating through control 15 $\mu\text{m}$  spacing, as claudin-low cell lines (Fig. 4.10). These findings may explain why MDA-MB-468 cells lines are metastatic, despite their high lamin A expression. Specifically, MDA-MB-468 did not easily migrate through confined spaces; however, when given the opportunity to migrate without the need for major nuclear deformation, the cells were over three times more likely to successfully migrate through 15  $\mu\text{m}$  constrictions than through 1- or 2- $\mu\text{m}$  wide constrictions.

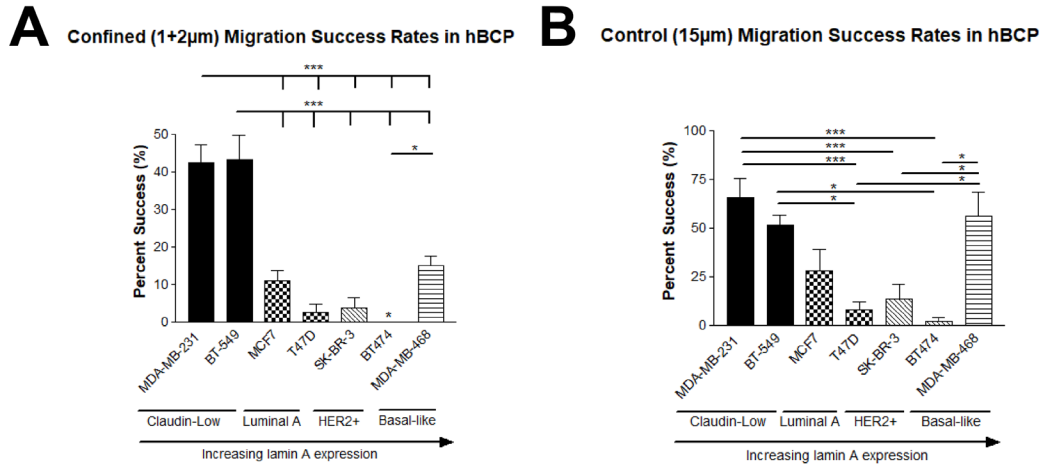


**Figure 4.10: Transit success rates for human breast cancer panel cell lines in confined and control constrictions.** Cell lines arranged in order of increasing lamin A expression. Filled black bars represent claudin-low, highly metastatic cell lines. Checker filled bars represent breast cancer luminal A sub-type cell lines, diagonal filled bars represent HER2+ cell lines, and horizontal filled bars represent basal-like cell lines. (A) Average percent of cells successfully migrating through confined constriction (1 + 2 µm width). (B) Average percent of cells successfully migrating through control constriction (15 µm width). Percent shown as mean of experimental averages ± SEM (\*,  $p < 0.05$ ; \*\*\*,  $p < 0.001$ , by one-way ANOVA with Bonferroni’s multiple comparison test.) Data from at least three independent experiments per cell line.

*Transit Time and Success Rate does not vary in 4T1 Models based on Lamin A Expression:*

Although differences in transit time were associated with altered lamin A expression in the polyoma middle T model, and the human breast cancer panel, transit time and

success rate did not correlate with lamin A expression in the 4T1 isogenic progression series in either confined and control spacing (Fig. 4.11 and 4.12). The different cell lines maintained very similar transit times during both confined (1- and 2- $\mu\text{m}$  widths) and control (15- $\mu\text{m}$  width) migration.

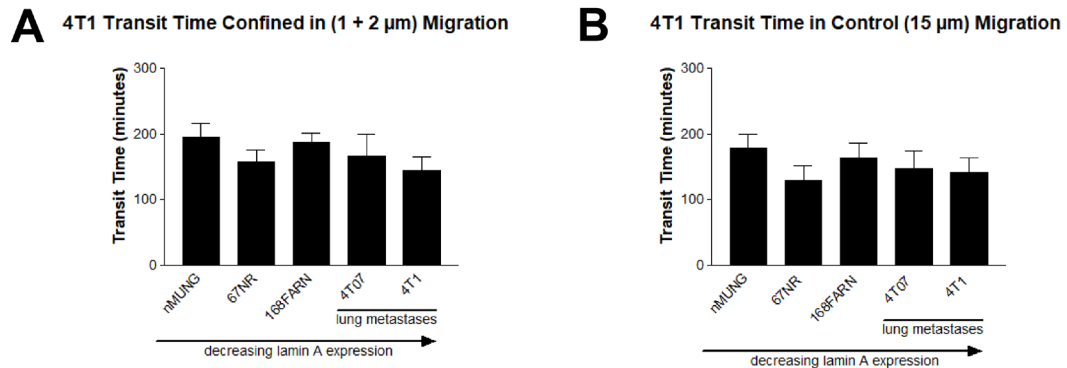


**Figure 4.11: Transit time for 4T1 mouse breast cancer model cell lines in confined and control constrictions.** Cell lines are labeled in order of decreasing lamin A expression and increasing metastatic capacity. (A) Average transit time for successful migration through confined constriction (1 + 2  $\mu\text{m}$  width). Mean  $\pm$  SEM. One-way ANOVA with Dunn's multiple comparison test;  $n \geq 30$ , from at least three independent experiments per cell line. (B) Average transit time for successful migration through control constriction (15  $\mu\text{m}$  width). Mean  $\pm$  SEM. One-way ANOVA with Dunn's multiple comparison test;  $n \geq 20$ , from at least three independent experiments per cell line.

Similarly, the transit success rates between cell lines in the 4T1 isogenic model were not statistically different (Fig. 4.12). The transit success rates through confined spaces ranged between 25-50% on average, but varied enough that differences were not statistically significant (Fig. 4.12A). During migration through  $15 \times 5 \mu\text{m}^2$  control constrictions, the success rates of the cells ranged between 55-75% success rates, with differences not being statistically significant (Fig. 4.12B).

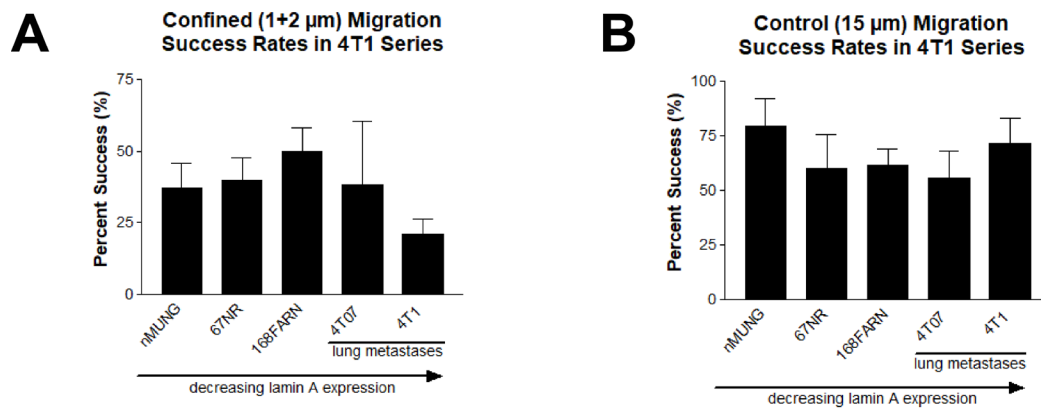


**Figure 4.12: Success rate for 4t1 mouse breast cancer model cell lines in confined and control constrictions.** Cell lines arranged in order of decreasing lamin A expression, and increasing metastatic potential. (A) Average percent of cells successfully migrating through confined constriction (1 + 2  $\mu\text{m}$ ). (B) Average percent of cells successfully migrating through control constriction (15  $\mu\text{m}$ ). Percent shown as mean of experimental averages  $\pm$  SEM. One-way ANOVA with Bonferroni's multiple comparison test, taken from at least three independent experiments per cell line.

## **Discussion**

Irregular nuclei have long been considered a hallmark of cancer diagnosis, but it is recent that the expression of nuclear lamins, which determine nuclear stability and deformation, were found to play a role in cancer (Belt et al. 2011; Bussolati et al. 2014; Hutchison et al. 2014). In breast cancer, reduced lamin A/C expression has been implicated in reduced disease free survival (Capo-chichi et al. 2011; Wazir et al. 2013). As the major determinant of nuclear deformation, and the rate-limiting step in cell migration, we examined whether differences in lamin A/C expression correlated with increased migration potential and disease progression in breast cancer. Using three independent breast cancer cell line models, we quantified lamin A/C expression and the cells respective migratory behavior.

In both the human breast cancer panel and the 4T1 mouse isogenic progression series, lamin A expression varied across cell lines (Fig. 4.7 and Fig. 4.5, respectively). In general, the more aggressive the cell line, the lower the expression of lamin A. This trend was especially obvious in the polyoma middle T model, where lamin A expression was much higher in the nonmetastatic, PyMT, cell line (Fig. 4.4). One notable exception was found in the basal-like cell lines of the human breast cancer panel. Although basal-like tumors are often considered metastatic, and have a poor prognosis, lamin A expression was highest in these cell lines (Fig. 4.7).

Because nuclear stiffness and deformation is governed mainly by lamin A/C expression, we hypothesized that cells expressing the highest levels of lamin A/C would migrate the least in constrictions smaller than the size of the nucleus. In both the polyoma middle T model and the breast cancer panel, this trend held true (Fig. 4.8 and Fig. 4.9). Cell lines such as PyMT and MDA-MB-468 were much less likely to migrate in confined spaces than their metastatic counterparts (Fig. 4.8 and Fig. 4.10, respectively). However, not all cells migrated in response to their lower lamin A levels, such as T47D and MCF7 (Fig. 4.9). Although both cell lines had lower levels of lamin A expression, they behaved more epithelial like, and did not migrate very successfully through the constrictions.

Although lamin A/C expression variability has been described previously in cells with different migratory abilities (Davidson et al. 2014), this work did not reveal many significant differences amongst cell lines migrating through confined spaces. Most interesting was that the 4T1 progression series cell lines had very little variability in transit time through specified constrictions, perhaps indicating that lamin A expression plays a role in cell migration through confined spaces, but is not the only determinant for defining migratory capacity. Cell migration is known to be influenced by many additional factors, such as migration mode of the cell (Friedl and Wolf 2003; Haeger et al. 2014), the cell cytoskeleton (Khatau et al. 2012; Petrie et al. 2014; Petrie and Yamada 2015), and biophysical cues in the tissue microenvironment such as stiffness and expression of matrix metalloproteinases (MMPs; Carey et al. 2012; Krause and Wolf 2015; Nabeshima et al. 2002; Paszek et al. 2005). Together many factors contribute to

the cell's ability to invade and metastasize throughout the body, and our work nicely illustrates the often major role that lamin expression can play in this mechanism.

## CHAPTER 5: CHARACTERIZATION OF NUCLEAR ENVELOPE RUPTURE IN BREAST CANCER PROGRESSION

### **Abstract**

Invasion of tumor cells into the surrounding tissue is a critical step in the metastatic cascade. During invasion, cancer cells often pass through interstitial spaces smaller than the cell nucleus. ‘Squeezing’ the cell nucleus through such constrictions can result in a transient loss of nuclear envelope (NE) integrity, referred to as NE rupture (Denais et al. 2016; Raab et al. 2016). Although NE rupture has been associated with increased chromatin herniation and DNA damage, the consequences of NE rupture have yet to be investigated in a range of cancer cells with increasing metastatic potential. Using two different breast cancer cell line models, we characterized the presence of NE rupture during confined migration as a function of metastatic potential. Our results indicate that NE rupture rate and duration is independent of metastatic potential. Probing for the protein machinery responsible for NE repair following NE rupture, ESCRT-III, revealed similar expression and function across various cell lines, indicating that NE repair is a highly conserved process.

### **Introduction**

Recent studies (Denais et al. 2016; Raab et al. 2016) have shown that nuclear deformation during cell migration in confined 3D environments can lead to a transient break in the NE (‘NE rupture’), resulting in the exchange of cytoplasmic and nuclear proteins. The NE is quickly resealed following NE rupture by ESCRT-III machinery,

but can result in the formation of nuclear fragmentation (Denais et al. 2016; Raab et al. 2016). Such NE rupture has been illustrated in cancer cells, fibroblasts, and immune cells (Denais et al. 2016; Raab et al. 2016); however, differences in the extent and duration of NE rupture had not yet been explored in cancer progression models. Identifying differences between cancer cells of different metastatic potential could reveal potential treatment targets for invasive cancers.

Initial results from our recent work indicated that the rate of NE rupture may correlate with lamin A/C expression (Denais et al. 2016; Raab et al. 2016). As the key regulator of nuclear stiffness, reduced lamin A/C expression often results in more successful “squeezing” through confined spaces (Davidson et al. 2014), and potentially altered nuclear morphology. Because lamin expression is known to be deregulated in many cancers, and changes in lamin expression often correlate with negative outcomes (Hutchison et al. 2014; Matsumoto et al. 2015), we hypothesized that altered nuclear morphology and deformation due to lower lamin expression in more metastatic cells may lead to higher rates of NE rupture.

To test whether NE rupture varies amongst cell lines of varying metastatic potential, two different cell line models (see Chapter 4 for details) were chosen for this study. One isogenic breast cancer model, the mouse 4T1 progression series (Aslakson et al. 1992; Dexter et al. 1978), was used to examine differences in NE rupture in cells of the same genetic lineage but with different metastatic potential. An additional model, consisting

of 7 human breast cancer cell lines from different breast cancer sub-types, including luminal, HER2+, basal-like, and claudin-low sub-types, was used to examine how NE rupture rate, duration, and repair may vary between these cell lines. Together, these two models were chosen to encompass the varying degrees of metastatic potential in breast cancer progression.

To compare such a large panel of cell lines, an experimental set-up that is precise and consistent between experiments is essential. Microfluidic devices that allow for precise control over constriction size (Davidson et al. 2015) provide an excellent platform to perform comparison studies of physical properties of cell behavior such as NE rupture. Analysis of migration through microfluidic devices was paired in this study with an automated analysis program (Elacqua et al. 2018) to enable how NE rupture rate and duration vary in large panels of cell lines.

## **Materials and Methods**

### *Cell Culture Techniques:*

4T1 mouse isogenic breast cancer series cell lines, i.e. 67NR, 168 FARN, 4T07, and 4T1, were a generous gift from Dr. Peter Friedl (St. Radboud University Nijmegen Medical Centre, University of Nijmegen, The Netherlands and MD Anderson Cancer Center, Houston, TX, USA). The Friedl lab also provided the nMUNG normal mouse epithelial cell line, which was used as an additional control. nMUNG, 67NR, 168

FARN, 4T07, and 4T1 cell lines were maintained in RPMI (Gibco) supplemented with L-glutamine (Gibco), sodium pyruvate, 10% FBS (VWR), and 1% Pen/Strep (Gibco).

Human breast cancer panel cell lines MDA-MB-231, MDA-MB-468, MCF7, SK-BR-3 were obtained from the American Type Culture Collection (ATCC), and grown in DMEM (Gibco) supplemented with L-glutamine, 10% FBS (VWR), and 1% Pen/Strep (Gibco). Human breast cancer cell lines BT-549, BT-474, and T47D were obtained from ATCC, and grown in RPMI (Gibco) medium supplemented with L-glutamine, 10% FBS (VWR), and 1% Pen/Strep (Gibco).

All cells were cultured at 37° C, and 5% CO<sub>2</sub>.

#### *Generation of Fluorescently Labelled Cell Lines:*

Retroviral vector (pQCXIP-NLS-copGFP-P2A-H2B-tdTomato-IRES-puro, System Biosciences) was used to stably modify cells to co-express NLS-GFP and H2B-tdTomato as described previously (Elacqua et al. 2018) and in Chapter 2. In brief, fluorophores attached to proteins and sequences of interest were ligated into the digested pQCXIP vector backbone. Successful colonies of interest were collected and sequenced. Retroviral particles were produced in 293-GPG cells, collected, and purified every 24 hours for 5 days following transfection. Cells of interest were transduced with viral stock and 8 µg/mL polybrene (Sigma Aldrich) every 24 hours for three days. Cells

underwent selection with puromycin three days following viral transduction, and sorted using a BD FACSAria Fusion fluorescence activated cell sorter (Cornell University Biotechnology Resource Center) for cells that expressed both fluorophores.

*Microfluidic Device Preparation:*

Microfluidic devices fabricated via 2-layer SU-8 photolithography were used to create polydimethylsiloxane (PDMS, Dow-Corning) replicates. Nanofabrication techniques to create the silicon wafer for the devices were used as described previously (Davidson et al. 2015). PDMS stamps of microfluidic devices were covalently attached to glass coverslips via plasma cleaning (Harrick Plasma), and covalent bonds were enhanced via a short 5-minute heat incubation. Devices were then washed with 70% ethanol and water, coated with 50 µg/mL rat tail collagen type I (Corning) diluted in 0.02 M glacial acetic acid (Sigma), and incubated overnight at 4°C.

Cells were seeded into the microfluidic devices on the morning of the time-lapse acquisition following a media rinse to remove any excess collagen. Cells were seeded at a density of 30,000 cells/device. Cells were allowed to attach for 2 hours, and then cell medium was changed in both reservoirs to establish a 0 to 10% FBS gradient. Prior to beginning overnight imaging cell media was changed to either FluoroBrite DMEM (Gibco) or phenol-red free DMEM medium (Gibco) to reduce background fluorescence.

### *Time-Lapse Microscopy:*

Immediately before imaging, media was changed to phenol-red free or FluoroBrite DMEM medium (Gibco) supplemented with 25 mM HEPES (Gibco) at a 0 to 10% FBS (VWR) gradient. Migration devices were sealed with a coverslip, and loaded into a custom-made holder on a laser scanning confocal microscope (LSM 700, Zeiss). Cells were maintained on a temperature-controlled stage at 37° C overnight, and images were acquired at 20× magnification (NA 0.8 air objective) every 10 minutes with a CoolSNAP EZ CCD camera (Photometrics) until at least 100 time points had been acquired. Zen software (Zeiss) was used to automate image acquisition, Images of the migration device and cells were acquired with differential interference contrast (DIC); fluorescence microscopy was used to capture the NLS-GFP signal (excitation with 450-490 nm light, collection of emission at 500-550 nm; exposure time of 75 ms), and the H2B-tdTomato signal (excitation by 550-580 nm light, collection of emission at 590-650 nm light; exposure time of 400 ms). All images were saved in the Carl Zeiss Image (.czi) format.

### *NE Rupture Analysis:*

Overnight time-lapse migration experiments were analyzed with an automated migration analysis program in MATLAB described in detail in Chapter 2 (Elacqua et al. 2018). The program outputs nuclear transit time, migration success rate, and NE rupture duration. Additional outputs, such as rate of NE rupture was derived from the automated analysis data.

*Western Blot:*

Western blots were performed using cell lysates to quantify ESCRT-III protein levels. Samples were prepared from confluent 6-well-plates, and were lysed in high salt (750mM) RIPA buffer supplemented with cOmplete, EDTA-Free proteinase inhibitor (1×; Roche). Lysed samples were vortexed, boiled, and centrifuged. Protein content was measured using standard Bradford assay techniques. Samples (25 µg protein each) were run on 10% Tricine gels (Gibco) with 10% tricine SDS running buffer (Novex) at a voltage of 95 V for 90 minutes. Following gel electrophoresis, Immobilon-FL transfer membranes (Gibco) were activated in methanol for 1 minute, neutralized in transfer buffer along with blotting paper and the gel, and assembled into a transfer sandwich. Transfers were performed on a trans-blot SD semi-dry transfer cell (Bio-Rad) for 1 hour at 16 V. Membranes were then blocked in 3% BSA in TBS-T for one hour. Primary antibodies (anti-CHMP2A, Proteintech, dilution 1:500; anti-CHMP7, Sigma, dilution 1:200; anti-histone H3, Cell Signaling, dilution 1:5000) were diluted in 3% BSA in TBST and incubated overnight at 4°C. Secondary antibodies (donkey anti-mouse 680 and donkey anti-rabbit 800, Licor dilution 1:1000) were diluted in 3% BSA in TBS-T and incubated for one hour at room temperature. All membranes were imaged and analyzed using the LI-COR Odyssey CLx. CHMP2A and CHMP7 concentrations were normalized to the histone H3 loading control, and presented relative to nMUNG control breast epithelial cell line. Mean ± standard error of the mean from three independent blots was used to perform a one-way ANOVA.

*Human Protein Atlas:*

Breast cancer data from the Human Protein Atlas were used to determine the frequency of mutations in two ESCRT-III proteins, CHMP2A and CHMP7, in cancer, and whether changes in CHMP2 and CHMP7 expression impact patient survival (Uhlen et al. 2017). The Human Protein Atlas database was used to access TCGA transcriptomics and antibody based protein data from 1075 patients with breast cancer, and was used to generate Kaplan-Meier plots based on expression levels of CHMP2A and CHMP7.

*Statistical Analysis:*

Statistical analysis was performed using GraphPad Prism software. Data of NE rupture duration were tested for Gaussian distribution, and means were then compared using the appropriate statistical test. If distributions were found to be Gaussian, a one-way ANOVA was performed with a Bonferroni multiple comparison post-test. Samples that were not normally distributed were compared using a one-way ANOVA with Dunn's multiple comparison post-test.

Protein expression in Western blots was quantified, and normalized in respect to a protein control. Differences between cell line protein expression were expressed relative to a control cell line, and differences were determined via a one-way ANOVA. All data are based on at least three independent experiments.

## Results

### *Nuclear Fragmentation Increases with an Increase in Metastatic Potential:*

Nuclear stiffness is a rate-limiting step during confined migration, and is governed by lamin expression and chromatin condensation (Dahl et al. 2004, 2005; Davidson et al. 2014; Friedl et al. 2011; Lammerding et al. 2006). Our previous work indicated that metastatic, aggressive cell lines often express lower levels of lamin A than their less metastatic counterparts (Chapter 4); however, it was not clear whether lower expression of lamin A/C increases the likelihood of NE rupture and/or nuclear fragmentation during cell migration. We hypothesized that metastatic cells may experience higher rates of NE rupture and nuclear fragmentation, resulting in increased levels of DNA damage, and ultimately more genomic mutations and malignant behavior.

Using cell lines from the mouse 4T1 isogenic breast cancer series, we studied whether the presence of nuclear fragmentation was associated with metastatic potential. The most aggressive cell line, 4T1, had over six-times times more fragmented nuclei following confined migration than its nonmalignant counterpart, 67NR ( $45.4 \pm 8.80\%$  vs.  $7.3 \pm 4.12\%$ , respectively; Fig. 5.1). Nuclear fragmentation correlated inversely with lamin A expression, with 4T1 cells having the lowest levels of lamin A expression, and nonmalignant 67NR cells the highest levels of lamin A expression in the isogenic mouse model (Fig. 4.5).

Of note, the control cell line, nMUNG, showed a similar rate of nuclear fragmentation as the most aggressive 4T1 cell line. This high rate of nuclear fragmentation could be due to a difference in genetic background of the nMUNG cells (Fig. 4.2), or provide a potential mechanism to induce cell death in the normally noncancerous, nonmigratory epithelial mNUNG cells.

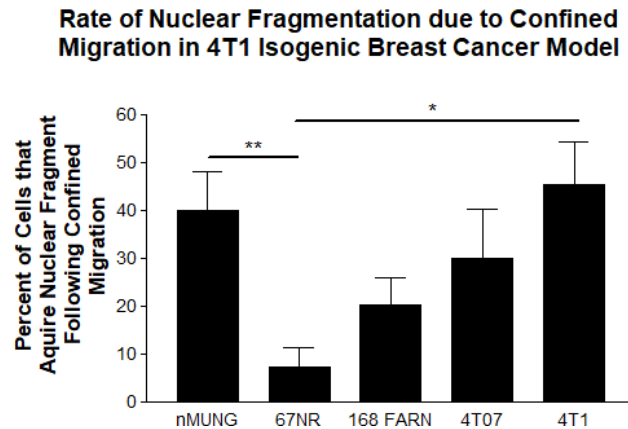


**Figure 5.1: Nuclear fragmentation due to confined migration.** Percentage of cells from 4T1 mouse breast cancer progression series that exhibit nuclear fragmentation following migration through confined constrictions. Percentage of cells with nuclear fragmentation shown as mean of experimental averages  $\pm$  SEM (\*,  $p < 0.05$ ; \*\*,  $p < 0.01$ , by one-way ANOVA with Bonferroni's multiple comparison test). Data presented are from at least three independent experiments per cell line.

*NE Rupture Rate does not Significantly Increase with Metastatic Potential and Lamin A Expression:*

Increases in nuclear fragmentation following confined migration may indicate the potential mechanical stress that nuclei experience during migration through tight spaces. Previous results indicated that increasingly metastatic cancer cells had lower lamin A expression, and exhibited higher percentages of nuclear fragmentation (Fig. 4.5 and Fig. 5.1). A growing number of studies have indicated mechanical compression of the nucleus as a major cause for NE rupture (Le Berre et al. 2012; Broers et al. 2004; Denais et al. 2016; Raab et al. 2016; Hatch and Hetzer 2016).

Similar to nuclear fragmentation, we observed an increase in the rate of NE rupture when cells migrated through confined spaces. However, the differences in NE rupture rate between cells with variable lamin A expression or metastatic potential were not statistically significant (Fig. 5.2). A lack of differences in NE rupture rate in increasingly metastatic cell lines could indicate that the rate and presence of NE rupture is not correlated with metastatic potential or lamin expression, but instead occurs at a predictable rate when pore size is too small for the nucleus to deform through during confined migration.

### Rupture Rate during Confined Migration (1+2 $\mu\text{m}$ ) in 4T1 Series

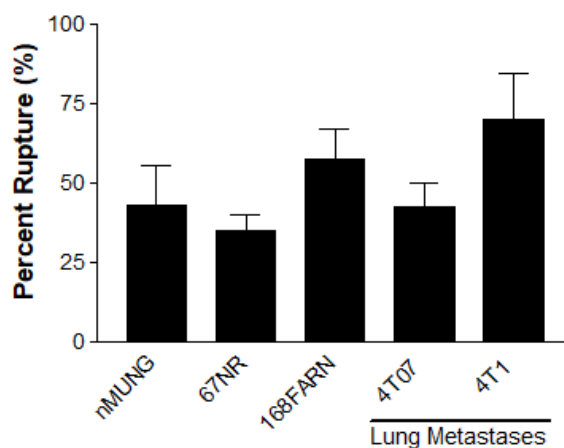


**Figure 5.2: Rate of NE rupture in increasingly metastatic cell lines.** Percentage of cells from 4T1 mouse breast cancer progression series that exhibit nuclear fragmentation following migration through confined constrictions. Percentage of cells with NE rupture shown as mean of experimental averages  $\pm$  SEM by one-way ANOVA. Data shown are from at least three independent experiments per cell line.

*The duration of NE Rupture is conserved across cell lines:*

Although, the rate at which NE rupture occurred did not vary significantly between cell lines, we hypothesized that the duration of NE rupture events may depend on the metastatic potential, reflecting differences in the resealing of the nuclear membranes following NE rupture (Fig. 5.3).

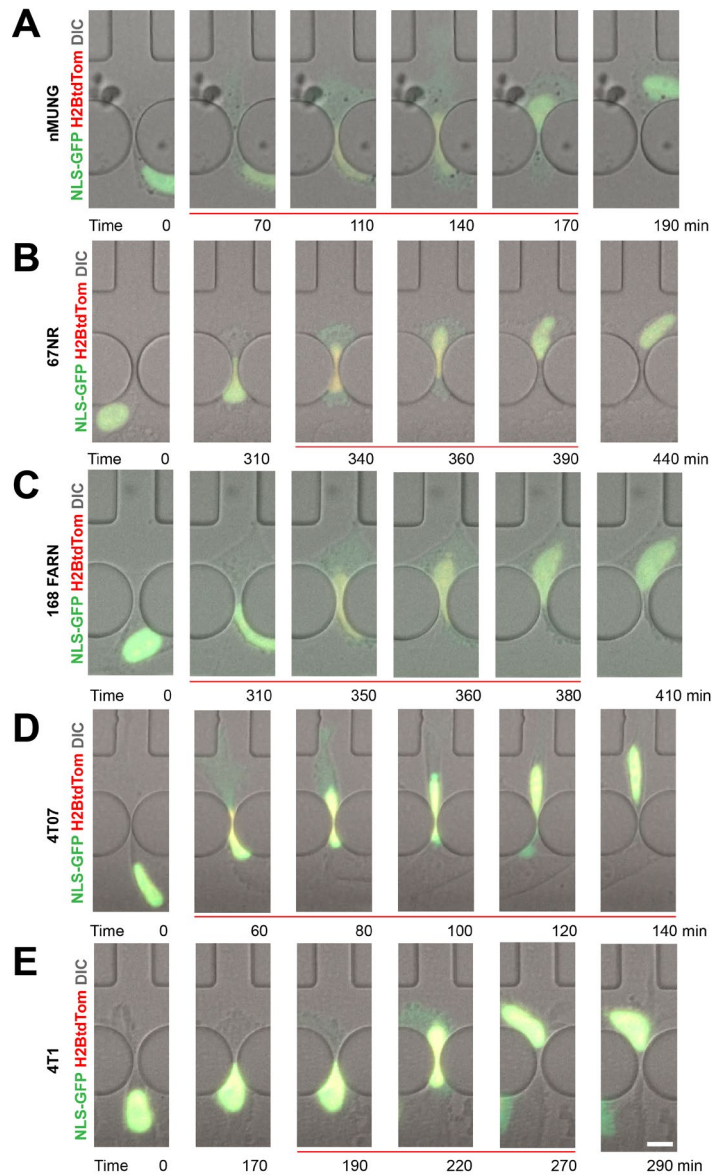


**Figure 5.3: Representative image sequences of 4T1 cell lines experiencing NE rupture during confined migration.** NLS-GFP is labeled in green, and histone H2B is labeled in red. Red line lines below frames indicate beginning and duration of NE rupture. (A, B, C, D, E) Representative examples of nMUNG epithelial (A), 67 NR nonmetastatic (B), 168 FARN (C), 4T07 (D), and 4T1 metastatic (E) exhibiting migration-induced NE rupture. Constriction size:  $2 \times 5 \mu\text{m}^2$ ; scale bar:  $20 \mu\text{m}$ .

Studies across twelve different breast cancer cell lines (Fig. 5.4) revealed similar values in NE rupture repair time across species and cell line panels, even for cells with little migratory behavior. Following an initial break in the NE, the duration of NE repair was consistent across almost all cell lines, regardless of lamin expression or metastatic potential (Fig. 5.4). On average, the duration of NE rupture lasted between 70 and 129 minutes.

The 4T1 metastatic cell line was the only cell line that had a statistically significant shorter NE rupture duration (Fig. 5.4). 4T1 NE rupture duration showed minimal variation, while most other cell lines experienced slightly larger ranges for NE rupture duration, and could be the reason for this statistical significance (Fig. 5.4A).

Interestingly, in the human breast cancer panel, the three most metastatic cell lines occasionally exhibited some extremely long NE rupture events (Fig. 5.4A, red box). It would be interesting to follow the fate of cells with extended NE rupture durations, to identify if this sub-population may be a driver for increasingly metastatic phenotypes.

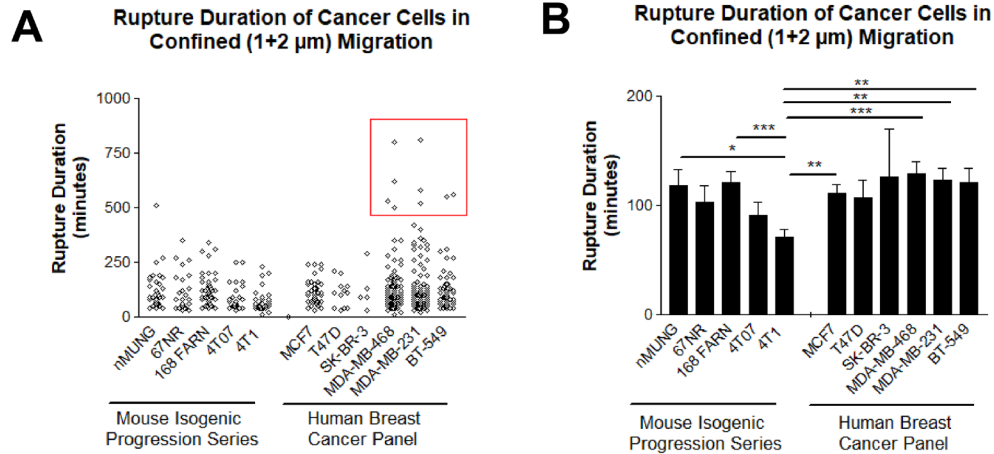


**Figure 5.4: NE rupture duration for the 4T1 mouse isogenic breast cancer cell line series and the human breast cancer cell line panel.** (A) Scatterplot of NE rupture duration across cell lines. Red box indicates significant outliers in highly metastatic cell lines MDA-MB-468, MDA-MB-231, and BT-549. (B) Bar graph of average NE rupture duration across cell lines. Mean  $\pm$  SEM (\*,  $p < 0.05$ ; \*\*,  $p < 0.01$ , \*\*\*,  $p < 0.001$ , by one-way ANOVA with Dunn's multiple comparison test;  $n = 36$  for nMUNG cells;  $n = 31$  for 67NR cells;  $n = 49$  for 168 FARN cells;  $n = 26$  for 4T07 cells;  $n = 42$  for 4T1 cells;  $n =$  for 45 MCF7 cells;  $n = 13$  for T47D cells;  $n = 5$  for SK-BR-3 cells;  $n = 115$  for MDA-MB-468 cells;  $n = 115$  for MDA-MB-231 cells;  $n = 64$  for BT-549 cells; from at least three independent experiments per cell line. ( $N = 8$  for nMUNG;  $N = 8$  for 67NR;  $N = 4$  for 168 FARN;  $N = 9$  for 4T07;  $N = 3$  for 4T1;  $N = 3$  for MCF7;  $N = 3$  for T47D (additional experiments had no successful cell migration through constrictions);  $N = 7$  for SK-BR-3;  $N = 5$  for MDA-MB-468;  $N = 5$  for MDA-MB-231;  $N = 3$  for BT-549).

Note that panels A and B represent the same data.

*ESCRT-III expression is conserved across cell lines:*

We and others have shown that ESCRT-III machinery is involved in resealing the NE following NE rupture events, and that silencing ESCRT-III proteins CHMP2A and CHMP7 using siRNA increased NE rupture duration and cell death (Denais et al. 2016; Raab et al. 2016; Elacqua et al. 2018). Our observations that NE rupture duration is conserved across almost all cell lines led us to hypothesize that ESCRT-III protein expression is also conserved across cell lines, regardless of metastatic potential. Consistent with this hypothesis, Western blot analysis revealed similar levels of CHMP2A expression across all 4T1 isogenic mouse model cell lines (Fig. 5.5). Blotting for additional ESCRT-III protein, CHMP7, did not yield reliable results, possibly due to inconsistent protein extraction or detection. The similar levels of CHMP2A expression across the 4T1 mouse isogenic breast cancer series support our interpretation that NE rupture duration is conserved among almost all cell lines, regardless of metastatic potential.

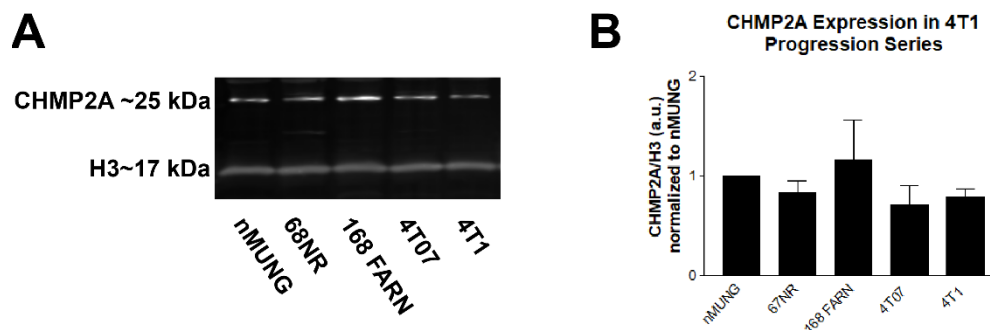


**Figure 5.5: ESCRT-III proteins are conserved across cell lines of various metastatic potential.** (A) Representative Western blot for CHMP2A, a protein part of

the ESCRT-III machinery, in the isogenic 4T1 mouse breast cancer progression series and the normal breast epithelial control cell line, nMUNG. Histone H3 was used as loading control. (B) Analysis of CHMP2A Western blot results, normalized to histone H3 loading control, and relative to the nMUNG control breast epithelial cell line. Mean  $\pm$  standard error of the mean from three independent blots. One-way ANOVA with Dunn's multiple comparison did not reveal any statistically significant differences.

To confirm that ESCRT-III machinery functioned similarly across cell lines of different metastatic potential, regardless of ESCRT-III protein expression, we performed additional experiments observing the rate of NLS repackaging into the nucleus following cell division. Our results indicated that NLS-GFP repackaging duration following mitosis was similar within and across cell lines (Fig. 5.6).

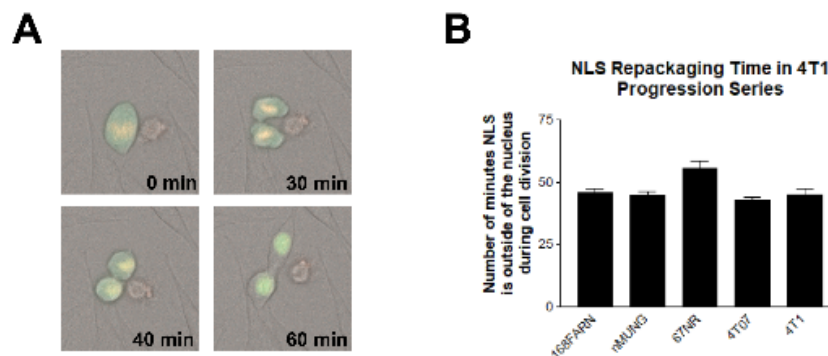


**Figure 5.6: Rate of NLS-GFP repackaging following cell division is conserved across cell lines of various metastatic potential.** (A) Representative image of cell undergoing cell division. NLS-GFP repackaging duration was measured from the first

timeframe where NLS-GFP became cytoplasmic. Repackaging was considered complete once two separate daughter cells formed, and the NLS-GFP signal had become completely nuclear again. (B) Analysis of NLS-repackaging rate across cell lines. Mean  $\pm$  standard error of the mean from three independent experiments per cell line. One-way ANOVA with Dunn's multiple comparison did not reveal any statistically significant differences.

*Altered Expression of ESCRT-III Proteins Results in Decreased Survival Rate:*

According to data from the Human Protein Atlas (Uhlen et al. 2017), there are significant differences in the survival rate of patients dependent on the expression levels of ESCRT-III machinery (Fig. 5.7). Specifically, when samples expressed low levels of either CHMP2A or CHMP7, the survival rate of the patient dropped significantly compared to samples with higher expression of ESCRT-III proteins. This indicates that changes to ESCRT-III machinery can have an impact how aggressive a cancer cell can be.

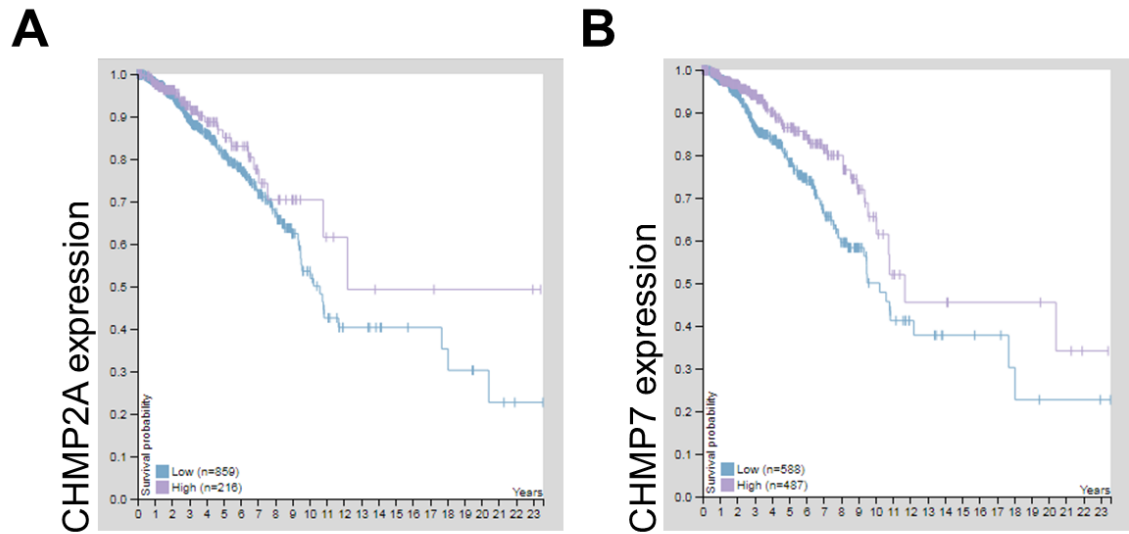


**Figure 5.7: Kaplan-Meier plots for patients with high and low expression of the ESCRT-III proteins, CHMP2A (A) and CHMP7 (B).** Blue line represents survival curve for low expression of ESCRT-III protein CHMP2A ( $n = 859$ ; A) and CHMP7 ( $n = 588$ ; B). Purple line represents survival curve for high expression of ESCRT-III protein CHMP2A ( $n = 216$ ; A) and CHMP7 ( $n = 487$ ; B). Plots created using microarray data from the Human Protein Atlas (Uhlen et al. 2017).

## Discussion

Mislocalization of organelles, chromatin herniation, entry of cytoplasmic nucleases, increased DNA damage, and nuclear fragmentation have all been associated with NE rupture (Hatch 2018; De Magistris and Antonin 2018; Shah et al. 2017). However, previous work did not examine how NE rupture rate and duration is altered in cells with variable metastatic potential. We hypothesized that malignancy and NE integrity are

related, in that metastatic breast cancer cells have weaker nuclei due to lower lamin A/C expression, resulting in higher rates of NE rupture during extensive nuclear deformation required for successful confined cell migration.

Initial results revealed that nuclear fragmentation, a potential indicator of NE rupture, increased in cells with higher levels of metastatic potential. (Fig. 5.1). However, because nuclear fragmentation can occur in the context of NE rupture, but can also form for other reasons, we followed-up these studies with the direct observance of NE rupture during confined migration. These experiments did not reveal differences in the rate of NE rupture with increasing metastatic potential (Fig. 5.2). A lack of differences in NE rupture rate in increasingly metastatic cell lines potentially indicates that the rate and presence of NE rupture is not correlated with metastatic potential or lamin expression, but instead occurs when the nucleus must deform through pore sizes smaller than a certain ratio of the nucleus' diameter during confined migration (Wolf et al. 2013).

Although there were no differences detected in the rate of NE rupture, we predicted that there may be differences in the resealing of the NE following NE rupture due to differences in expression of ESCRT-III proteins. Specifically, we hypothesized that increased migration of metastatic cells through confined environments could result in cells developing more efficient repair mechanisms. However, we found that the duration of NE rupture was consistent amongst almost all cell lines regardless of metastatic potential (Fig. 5.4). Additional experiments probing for CHMP2A ESCRT-III protein

expression via Western blot revealed conserved levels of CHMP2A expression across the cell lines (Fig. 5.5). Although CHMP2A expression was conserved across our model, it was essential to confirm that ESCRT-III machinery also functioned similarly across the cell lines in resealing the nuclear envelope. One important function of the ESCRT-III machinery is to repair the NE following cell division, in addition to repairing the NE following NE rupture. Therefore, we measured the time needed to re-establish nuclear NLS-GFP signal following cell division (Fig. 6.6). Again, all cell lines showed similar efficiency in resealing the NE following cell division. Together, our results indicate that NE rupture duration and the machinery needed to repair NE rupture are conserved across cell lines regardless of their metastatic capacity, likely due to the high evolutionary pressure imposed by the requirement to reseal the nuclear envelope following mitosis. These results indicate that it may be challenging to target nuclear envelope repair as a target for metastatic cancer cell therapies as it would likely similarly affect normal cells too.

Data from the Human Protein Atlas revealed that ESCRT-III proteins were mutated in less than one percent of breast cancers, and that higher expression of CHMP2A and CHMP7 proteins resulted in longer patient survival (Fig. 6.7). Previous work in pancreatic cancer has also shown that overexpression of CHMP1A, an additional ESCRT-III machinery protein, results in chromatin condensation, p53 phosphorylation, and cell growth inhibition; ultimately leading to increased cell death in PANC-1 cancer cells (Manohar et al. 2011). CHMP7 overexpression in Arabidopsis plants has also been

shown to cause plant dwarfism and premature cell senescence (Yang et al. 2016), providing strong evidence that over-expression of ESCRT-III could be used as a therapeutic target in primary tumors to induce cell senescence and death in metastasizing tumor cells. However, because ESCRT-III plays important roles in other cellular functions, it is possible that these observed effects are not solely due to their involvement in NE repair, and should be further studied.

## CHAPTER 6: LONG-TERM CONSEQUENCES OF CONFINED CELL MIGRATION ON CANCER CELLS

### **Abstract**

The consequences of nuclear deformation and NE rupture due to confined migration include nuclear fragmentation, chromatin herniation, organelle displacement, and DNA damage. To address the long-term consequences of these events, we repeatedly let clonal MDA-MB-231 cells pass through microfluidic devices with  $1 \times 5 \mu\text{m}^2$  and  $15 \times 5 \mu\text{m}^2$  constrictions. These cells were then expanded, and characterized to determine if there were any permanent changes to cell proliferation, cell cycle progression, or genetic instability. Our results indicate that the effect varied between individual clonal cell lines. While two of the clonal MDA-MB-231 cell populations remained viable and continued to proliferate following a second round of confined migration, the other two clonal populations did not. Such differences were further observed when characterizing population doubling time and DNA damage markers following confined migration. These findings suggest that even long after cells undergo nuclear deformation due to confined migration, consequences of such migration are still present. These findings suggest that genomic alterations due to nuclear deformation during confined cell migration could be a driver for further metastatic progression in cancer cells.

### **Introduction**

Genomic instability is the alteration of the cell genome via chromosomal instability (loss or gain of a whole chromosome, partial rearrangement of a chromosome, or the

duplication/deletion of portions of a chromosome), and genetic insertions/deletions (reviewed in Sansregret et al. 2018). Genomic instability and aneuploidy can ultimately result in impaired cell signaling, altered gene expression, and changes to the cell cycle. A hallmark of cancer, genomic instability, further propagates cell mutations during cancer progression via error prone DNA damage repair mechanisms such as non-homologous end joining (NHEJ; Hanahan and Weinberg 2011). Such mechanisms help drive cancer cell aggressiveness, and it is estimated that approximately 60-80% of breast cancer tumors have aneuploidy karyotypes (Donepudi et al. 2014).

Previous work has shown the presence of chromatin herniation and nuclear fragmentation following confined cell migration, which can contribute to DNA damage (Fig. 2.4B and Fig. 5.1; Denais et al. 2016; Vargas et al. 2012). Furthermore, increased double-stranded DNA breaks following migration through confined spaces has been shown via DNA damage markers such as gamma-H2A.X (Denais et al. 2016; Irianto et al. 2016; Raab et al. 2016). This work provides the foundation for our hypothesis that confined cell migration causes permanent alterations to the cell and its genome. In this chapter, we subjected clonal MDA-MB-231 cells to multiple rounds of confined ( $1 \times 5 \mu\text{m}^2$ ) and control ( $15 \times 5 \mu\text{m}^2$ ) migration. We then characterized any changes in the clonal cell populations by cell proliferation, scratch-wound, DNA content, and immunofluorescent assays. Our results indicated that some clonal populations undergo more profound long-lasting alterations than others, with one population undergoing catastrophic cell death following additional confined migration, illustrating the

profound impact that repeated nuclear deformation can have on cells migrating through confined spaces. Future work will be directed at identifying the molecular differences between the clonal populations responsible for these characteristic differences.

## **Materials and Methods**

### *Cell Culture Techniques:*

The human breast cell line MDA-MB-231 was obtained from the American Type Culture Collection (ATCC). Cells were grown in DMEM (Gibco) supplemented with L-glutamine, 10% FBS (VWR), and 1% Pen/Strep (Gibco). All cells were cultured at 37°C and 5% CO<sub>2</sub>.

### *Establishment of Clonal Cell Lines:*

Clonal cell populations were established from heterogeneous, low-passage MDA-MB-231 triple-negative breast cancer cells (ATCC). Cells were trypsinized and counted. Cells were then diluted to single cells, and seeded into two 96 well-plates with complete DMEM (Gibco) supplemented with 25 mM sodium pyruvate (Gibco). Single clones were allowed to expand for 7 days, and wells that established colonies from a single-cell were further propagated. Each clone was grown to confluency in a 96 well-plate, and seeded into increasingly larger culture vessels until cells reached confluency in a T150 cm<sup>2</sup> flask. Nine individual MDA-MB-231 clones were generated, and were then frozen until further use. Four clones were chosen to perform selection experiments based on

similarity in growth rate to normal, heterogeneous MDA-MB-231 populations. Clonal cell line selection experiments were conducted at the lowest possible passage number to ensure minimal genomic variation between clonal cells.

*Generation of Fluorescently Labelled Cell Lines:*

Retroviral vector (pQCXIP-NLS-copGFP-P2A-H2B-tdTomato-IRES-puro, System Biosciences) was used to stably modify heterogeneous MDA-MB-231 cells to express both NLS-GFP and H2B-tdTomato as described previously (Elacqua et al. 2018). In brief, fluorophores attached to proteins and sequences of interest were ligated into the digested pQCXIP vector backbone and colonies of interest were collected and sequenced. Retroviral particles were produced in 293-GPG cells from successful clones, and collected and purified every 24 hours for 5 days following transfection. Cells were transduced with viral stock and 8 µg/mL polybrene (Sigma-Aldrich) every 24 hours for three days. Cells underwent selection with puromycin 3 days following viral transduction, and sorted using a BD FACSAria Fusion fluorescence activated cell sorter (Cornell University Biotechnology Resource Center), for cells that expressed both fluorophores.

**Cell Selection Experiments:**

*Microfluidic Device Preparation:*

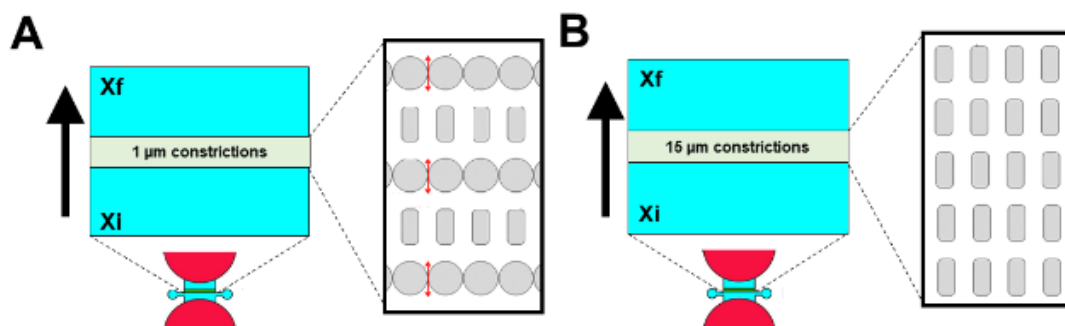


**Figure 6.1: Microfluidic device schematic.** Red half-circles indicate cell media reservoirs in microfluidic devices. Blue areas represent 200  $\mu\text{m}$  tall cell loading sections, and green areas represent 5  $\mu\text{m}$  tall sections where 1- or 15- $\mu\text{m}$  constrictions are located. Black arrows indicate the direction of cell migration. Xi represents side of microfluidic devices that cells are seeded into. Xf represents side of microfluidic devices where cells successfully migrate to. (A) Schematic of 1  $\mu\text{m}$  constriction devices. (B) Schematic of 15  $\mu\text{m}$  constriction devices.

Microfluidic devices consisting of confined constrictions ( $1 \times 5 \mu\text{m}^2$ ) or control ( $15 \times 5 \mu\text{m}^2$ ) channels were designed to enable the collection of cells following migration through specified constrictions (Fig. 6.1). These devices were fabricated via 2-layer SU-8 photolithography and deep reactive ion etching, and used to create a PDMS (Dow-Corning) replicate. This PDMS replicate was then used to create a plastic mold that was used to pattern successive PDMS stamps for the entirety of this study.

The microfluidic devices were covalently attached to glass coverslips via plasma cleaning (Harrick Plasma), and covalent bonds were enhanced via a short 5-minute heat incubation at 95° C. Devices were then washed with 70% ethanol and water, and coated with 50 µg/mL rat tail collagen type I (Corning) diluted in 0.02 M glacial acetic acid (Sigma), and incubated overnight at 4° C. At least 20 devices (5 slides) were prepared per clone and round of cell selection with 1 µm confined constrictions. An additional 20 devices (5 slides) were prepared with 15 µm confined constrictions. Large numbers of devices were prepared to ensure an adequate number of samples per clonal subpopulation following migration.

*Seeding Cells into Migration Devices:*

Following overnight collagen coating, devices were rinsed once with complete DMEM (Gibco) culture medium supplemented with 10% FBS (VWR) and 1% P/S (Gibco). The medium was aspirated out, and the entirety of the migration device was dried, ensuring that there were no air bubbles within the device. Cells diluted into cell culture media to a final concentration of 30,000 cells per 6 µl were then seeded into the inside port of the migration device (closest to the bypass channel). The devices were then placed into the incubator at 37°C. After 30 minutes of incubation, devices were checked for both initial attachment and the presence of cell in the bypass channel or crossed (Xf) side of the device (Fig. 6.1). If any cells were detected in either the bypass channel or the Xf side of the migration device, the device was excluded from the experiments. All devices successfully seeded were back flushed with cell culture media from the crossed side,

Xf, to the initial side, Xi, to avoid pushing cells through the constrictions or bypass channel (Fig. 6.1). Cells were then allowed to migrate through the microfluidic devices for 96 hours, with cell culture media changed every 48 hours. Samples were monitored daily for any samples with cells getting to Xf without migration through the constrictions.

*Trypsinization of Cells from Migration Devices:*

Following 96 hours of cell migration, cells were removed from the microfluidic devices via trypsinization. Before removal of cells, media was aspirated from migration devices, and the bypass channel reservoirs were sealed with vacuum grease to prevent the transfer of cells from Xi to Xf and vice versa during trypsinization. Blocking of the bypass channel on both the Xi and Xf side was visually confirmed using a dissection microscope, and PBS was added to side Xf to establish a temporary pressure gradient. Side Xi was rinsed with PBS, and 0.25% trypsin was added to trypsinize the cells. Cells were incubated in trypsin until rounded up, and were removed by adding concentrated complete DMEM medium supplemented with 10% FBS and 1% P/S to the Xi reservoir. Trypsinized cells were seeded directly into a well of fresh complete DMEM (Gibco) media supplemented with 25 mM of sodium pyruvate (Gibco), 10% FBS (VWR), and 1% Pen/Strep (Gibco) within a 96 well-plate. Importantly, cells were not spun down following trypsinization due to the low cell count. Devices were visually inspected for removal of all cells on the side of trypsinization. PBS was then added to side Xi, and side Xf was trypsinized following the same protocol. (Note: side Xi cells were removed

first to ensure that there was no possibility of cell wash-over from side Xi to Xf.) Cells that migrated through confined 1  $\mu\text{m}$  constrictions were pooled with cells trypsinized from additional confined 1  $\mu\text{m}$  constriction devices to provide larger numbers of cells for initial plating.

*Culture of Selected Cells following Trypsinization:*

Following trypsinization and seeding of cells from migration devices, cells were allowed to attach for at least 12 hours before media was rinsed to remove any excess trypsin and dead cells. Cells were cultured and expanded until there were enough cells to both freeze down aliquots and perform additional selection experiments—typically at least 750,000 cells per condition (Fig. 6.2). Following initial cell attachment and growth, cells that had migrated through 1  $\mu\text{m}$  confined constrictions were typically further pooled to establish higher density populations. At least 2 to 3 replicates of each condition were grown up to minimize sample loss in the case of extensive cell death.

During cell expansion, cells remained in DMEM (Gibco) supplemented with 25 mM of sodium pyruvate (Gibco), 10% FBS (VWR), and 1% Pen/Strep (Gibco) to promote cell division. Cell medium was changed every 3 days. Cells were not spun down during trypsinization until there was a high enough cell number to create a visible pellet following centrifugation—usually when seeding into a 6-well plate. During this time, culture medium was changed 12-24 hours following cell trypsinization to eliminate any cell death and excess trypsin.

*Rounds of Cell Selection:*

Each clone and a heterogeneous population of MDA-MB-231 cells were initially expected to undergo three rounds of cell selection through the migration devices (Fig. 6.2). Following each round of selection, cells were given up to 25 days to expand to a size large enough to reseed. In the case that cells were not capable of expanding sufficiently, smaller aliquots of the sample were used and frozen down.

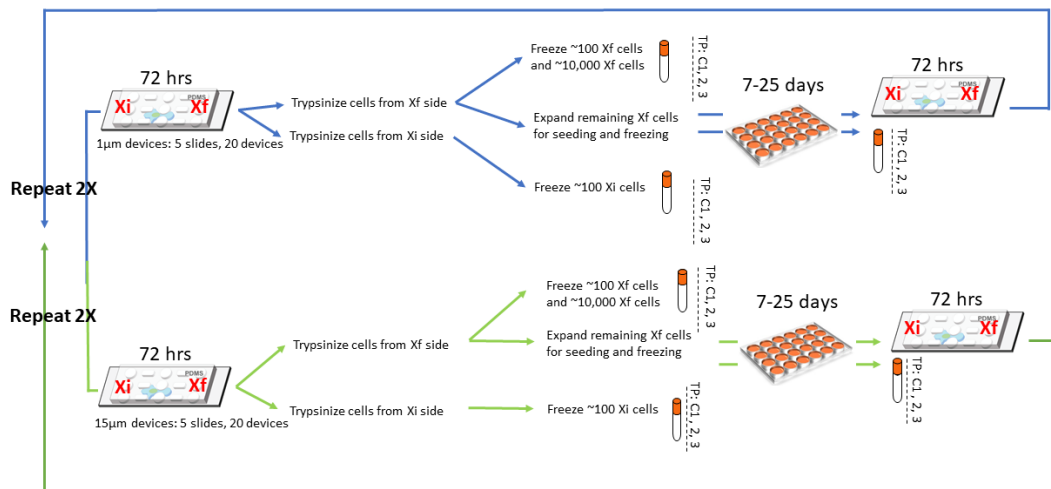


**Figure 6.2: Flow-chart of clonal selection migration experiments.** Cells were seeded at the same time point into microfluidic devices with either 1- or 15-µm constrictions. The cells were allowed to migrate for 96 hours, and trypsinized from cells that did not migrate through constrictions (Xi), and cells that successfully migrated through all three constrictions (Xf). Following trypsinization, cells were frozen either immediately following trypsinization, one day following reseeding, or 7-25 days following cell expansion. Additional cells were expanded to reseed back into constrictions. This

process was repeated three times. Note: for some clones, cells stopped proliferating after the second round of selection, and cells were thus not available for a third repeat.

### **Characterization of Clonal Cell Populations:**

Cell populations established from each round of selection in both confined 1  $\mu\text{m}$  constrictions, and control 15  $\mu\text{m}$  constrictions, along with the original clonal cell population underwent characterization for cell proliferation, cell cycle progression, migration, and senescence following selection, with the goal to elucidate any changes resulting from extended confined cell migration.

#### *Proliferation Assay:*

5,000 cells/well were seeded into 96 well-plates, and at least 8-12 wells were seeded for each clonal population per experiment. Following at least 12 hours of cell attachment, cells were placed into the Incucyte Zoom (Sartorius) and imaged at 20 $\times$  once every 1-2 hours for at least 5 days. Four images per well were taken at each time point. Incucyte Zoom (Sartorius) software was used to establish an image processing mask, and cell confluency was calculated for each well at every time point. Wells that were seeded at too high or low starting density, or were not imaged in focus, were excluded from analysis. Successful confluence percentages were exported via a .txt file, and analyzed in GraphPad Prism. Each proliferation experiment was repeated three times unless otherwise stated.

*DNA Content Assay:*

DNA content analysis was performed using a protocol adapted from (Walker et al. 1993). During cell trypsinization, at least 100,000 cells were spun down and resuspended in 1 mL of 1× PBS. 4 mL of cold, 100% ethanol was added to the cell/PBS suspension, and placed at  $-20^{\circ}\text{C}$  for at least two hours to allow for cell fixation. Following fixation, the cell suspension was spun down at 1,000 RPM for 10 minutes at  $4^{\circ}\text{C}$ . Supernatant was removed, and the cell pellet was resuspended in 300  $\mu\text{L}$  of PBS with RNase A (Sigma Aldrich) at a final concentration of 5  $\mu\text{L}$  RNase/mL. The resuspended pellet was incubated at  $37^{\circ}\text{C}$  for 30 minutes. Propidium iodide (Invitrogen, 1.0 mg/mL) was added at a 1:10 dilution and incubated for 10 minutes at room temperature. (Note: if flow cytometer was not available and/or down, samples can be stored at  $4^{\circ}\text{C}$  for up to 24 hours without change in fluorescence intensity.)

Cells were then sorted on a BD Accuri C6 Flow Cytometer. A linear gate was placed on the forward and side scatter plot, to eliminate debris and collect only intact cell data. An additional gate on a secondary graph plotting propidium iodide total fluorescence intensity area vs. height was used to exclude doublets and triplets. Samples were run at 35  $\mu\text{L}/\text{min}$ , with a core size of 16  $\mu\text{m}$ , until 100,000 gated cells were recorded. DNA content levels were recorded by plotting propidium iodide intensity vs. cell count on a linear scale. Peaks were used to estimate cell cycle phase, and cell count per phase was determined using the Accuri C6 Plus software (BD).

### *Immunofluorescence:*

Cells were seeded onto coverslips coated with 5 µg/mL fibronectin diluted in PBS (FC010 human plasma fibronectin; Millipore) at 37° C for two hours, and allowed to attach for at least two days. Samples were fixed in 4% paraformaldehyde diluted in PBS for 10 minutes at room temperature. Samples were rinsed 3-times with PBS. Samples were then permeabilized and blocked concurrently for one hour in a 3% BSA (Sigma Aldrich) solution diluted in PBS supplemented with 0.2% triton-X-100 (Sigma Aldrich) and 0.125% Tween (Sigma Aldrich) at room temperature. Primary antibody (Rabbit anti-phospho-histone H2A.X, Cell Signaling, 9718S, dilution 1:250) were diluted in 0.3% BSA (Sigma Aldrich) in PBS supplemented with 0.2% triton-X-100 (Sigma Aldrich) and 0.125% Tween (Sigma Aldrich), and incubated rocking overnight at 4°C. Samples were rinsed 3-times with PBS. Secondary antibodies (donkey anti-rabbit AlexaFluor-568, dilution 1:500) were diluted in 0.3% BSA (Sigma Aldrich) diluted in PBS supplemented with 0.2% triton-X-100 (Sigma Aldrich) and 0.125% Tween (Sigma Aldrich), and incubated rocking for 1 hour at room temperature. Samples were rinsed 3-times with PBS. Hoechst (Invitrogen, dilution 1:1000) was added to samples and incubated rocking for 30 minutes at room temperature. Samples were rinsed 3-times with PBS, mounted using Mowiol (Calbiochem), and allowed to dry for 2 hours before imaging.

### *Imaging of Fluorescent Samples:*

Z-stacks of samples were imaged on a laser scanned confocal microscope (LSM 700, Zeiss). Maximum intensity projection images of the fixed cells were used to visualize gamma-H2A.X and Hoechst fluorescence in samples. Three representative images were taken per sample in distinct areas.

*Image Analysis:*

Fluorescent images were analyzed using Fiji (Schindelin et al. 2012). For gamma-H2A.X analysis, images representing different fluorescent channels were opened separately, and the outline of each cell was traced in the red channel—using additional channels for cell location or size reference, if necessary. The average intensity of the outlined cell was recorded, and divided by the average background intensity of the red channel. All cells in each sample were analyzed, and the average was recorded for each experiment.

*Gamma-H2A.X vs. Propidium Iodide Flow Cytometry:*

During cell trypsinization, at least 100,000 cells were spun down and resuspended in 1 mL of 1× PBS. 4 mL of cold, 100% ethanol was added to the cell/PBS suspension, and placed at  $-20^{\circ}\text{C}$  for at least two hours to allow for cell fixation. Following fixation, the cell suspension was spun down at 1,000 RPM for 10 minutes at  $4^{\circ}\text{C}$ . Supernatant was removed, and the cell pellet was resuspended in 300  $\mu\text{L}$  of PBS containing 5  $\mu\text{L}/\text{mL}$  RNase A (Sigma Aldrich). The resuspended pellet was incubated at  $37^{\circ}\text{C}$  for 30

minutes. Primary anti-gamma-H2A.X antibody (Rabbit anti-phospho-histone H2A.X, Cell Signaling, 9718S, dilution 1:250) was added to the cell suspension and incubated at 4°C overnight. Following incubation, 3× rinses with PBS was performed, spinning down at 1,000 RPM for 5 minutes at 4°C each time. Secondary antibody (goat anti-mouse AlexaFluor-488, dilution 1:500; was added to cell solution and incubated for at RT for 1 hour. Following incubation, 3× rinses with PBS was performed, spinning down at 1,000 RPM for 5 minutes at 4°C each time. Propidium iodide (Invitrogen, 1.0 mg/mL) was added at a 1:10 dilution and incubated for 10 minutes at room temperature.

Cells were then sorted on a BD Accuri C6 Flow Cytometer. A linear gate was placed on the forward and side scatter plot, to eliminate debris and only collect cell data. An additional gate on a secondary graph plotting propidium iodide fluorescence intensity signal area vs. height was used to remove doublets and triplets. Cells were run at 35 µL/min, with a core size of 16 µm until 100,000 gated cells were recorded.

Cell cycle gates were determined by plotting propidium iodide intensity vs. cell count on a linear scale. Gates were then placed on plot of propidium iodide intensity vs. gamma-H2A.X fluorescent intensity to determine percent gamma-H2A.X expression throughout each phase of the cell cycle. All analysis was performed using Accuri C6 Plus software (BD).

*Scratch Wound Assay:*

50,000 cells/well were seeded into 96 well-plates, and at least 8-12 wells were seeded for each clonal population per experiment. Following at least 24 hours of cell attachment, confluent cell layers were scratched using the Wound Maker (Sartorius). (Note: cells need to be well attached and at 90% confluency before scratching to prevent mass cell lifting and uneven scratches, respectively.) Immediately following scratching, wells were rinsed with complete cell medium 2-times, replaced with fresh media, and placed into the Incucyte Zoom (Sartorius). Samples were imaged at 20× magnification once every 2 hours for at least 48 hours, or until the wound healed. 1-2 images per well were taken at each time point. Incucyte Zoom (Sartorius) software was used to establish an image processing mask, and wound density for each well at each time point was calculated. Wells with uneven scratches, low cell number, and variable density were excluded from analysis. Successful scratch wound density calculations were exported via a .txt file and analyzed in GraphPad Prism. Each experiment was repeated three times unless otherwise stated.

*Statistical Analysis:*

Statistical analysis was performed using GraphPad Prism software. Data was tested for Gaussian distribution, and means were then compared using the appropriate statistical test. If distributions were found to be Gaussian, a one-way ANOVA was performed with a Bonferroni multiple comparison post-test. Samples that were not normally distributed

were compared using a one-way ANOVA with Dunn's multiple comparison post-test. All data are based on at least three independent experiments.

## **Results**

### *Clonal populations struggled to expand following confined migration:*

Four clonal MDA-MB-231 populations were used to perform selection experiments based on their similarities in growth rate compared to the original, heterogeneous MDA-MB-231 population. All clones initially expanded normally following the first round of confined ( $1 \times 5 \mu\text{m}^2$ ) and control ( $15 \times 5 \mu\text{m}^2$ ) migration. Following the second round of confined migration, two of the clones, clone 6 and clone 8, struggled to proliferate (Fig. 6.3B). In both cell lines, cell proliferation stalled for over 50 days. In the confined clone 6 subpopulation, extensive cell death occurred after 60 days of culturing. In contrast, while the confined clone 8 subpopulation initially stalled proliferation, it began growing aggressively after approximately 57 days of culture. Of note, both clonal populations expanded normally following a second round of control ( $15 \times 5 \mu\text{m}^2$ ) migration, indicating that both clone 6 and clone 8 experienced changes in cell proliferation, possibly as a result of DNA damage or genomic instability, following the confined cell migration (Fig. 6.3B).

The other two clonal cell populations used in these experiments, clone 7 and clone 9, did not experience any difficulty expanding following a second, or third (clone 9 only), round of migration through either confined or control constrictions (Fig. 6.3).

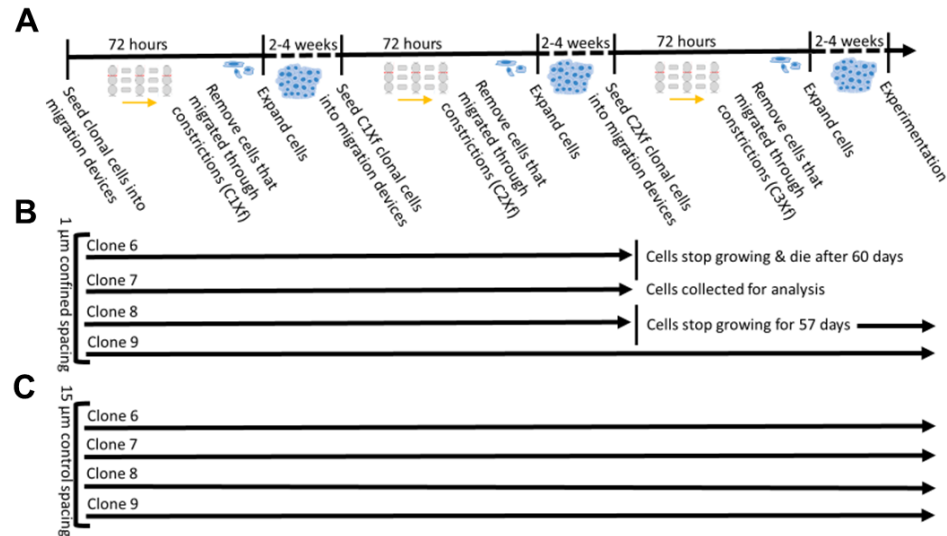


**Figure 6.3: Schematic overview of clonal cell selection experiments and outcome.**

(A) Timeline of clonal cell selection experiments. (B) Progress of each clonal population migrating through confined ( $1 \times 5 \mu\text{m}^2$ ) constrictions. (C) Progress of each clonal population migrating through control ( $15 \times 5 \mu\text{m}^2$ ) constrictions.

**Note:** Due to stalled proliferation in clones 6 and 8 following two rounds of confined cell migration, all clonal characterization assays were performed following one round of confined and control migration to provide sufficient cell densities for assays.

*Population doubling time remains unchanged in most clonal populations following confined migration:*

To better define the differences in cell proliferation following migration through selection devices, cell proliferation assays were performed following one round of migration in the clonal cell populations. Cells were seeded at equal densities, and allowed to grow for 5 days, or until confluency. Cell confluency and cell number was recorded every two hours using the Incucyte Zoom (Sartorius) incubator and software.

For clones 6, 7, and 9, the population doubling times did not change following one round of migration through confined and control constrictions (Table 6.1). In contrast, for clone 8, the population doubling time increased significantly following both confined and control cell migration (Table 6.1).

<b>Population Doubling Time (hr)</b>	<b>Original Clone</b>	<b>Crossed Control 15 <math>\mu\text{m}</math> Constrictions</b>	<b>Crossing Confined 1 <math>\mu\text{m}</math> Constrictions</b>
Clone 6	37.7 $\pm$ 0.64	36.6 $\pm$ 0.60	37.1 $\pm$ 0.32
Clone 7	27.0 $\pm$ 2.90	31.9 $\pm$ 0.64	31.4 $\pm$ 0.44
Clone 8	28.8 $\pm$ 1.17	30.0 $\pm$ 0.42 *	35.6 $\pm$ 1.59 *
Clone 9	31.7 $\pm$ 3.62	33.1 $\pm$ 2.83	30.3 $\pm$ 3.45

**Table 6.1: Population doubling time in clonal cell populations following one round of migration through confined and control constrictions.** Average population doubling time  $\pm$  SEM in hours (\*,  $p < 0.05$  compared to original clonal population; by one-way ANOVA with Dunn's multiple comparison post-hoc test). Data from three independent experiments.

*Cell cycle analysis of clonal cell populations following confined and controlled migration revealed no differences:*

The cell cycle is a tightly regulated process, that is often disrupted in cancer cells due to DNA damage, aneuploidy, and cell senescence (Sansregret et al. 2018) Because nuclear deformation has been associated with increased levels of DNA damage (Denais et al. 2016; Raab et al. 2016), cell cycle analysis was performed on clonal subpopulations following confined and controlled migration following one round of confined and control migration.

Growth inhibition was seen in clones 6 and 8 following a second round of confined migration. Furthermore, significant differences in population doubling time following only one round of migration in clone 8, indicated that there could be differences in the cell cycle following cell migration. However, none of the clones exhibited altered or disrupted cell cycles following one round of confined and control migration when compared to parental clones (Fig. 6.4).

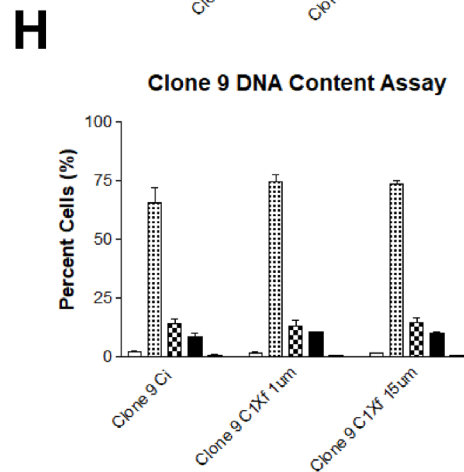
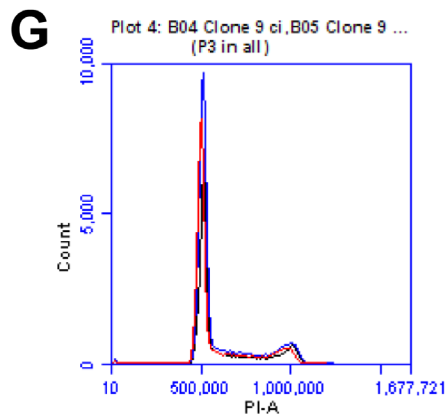
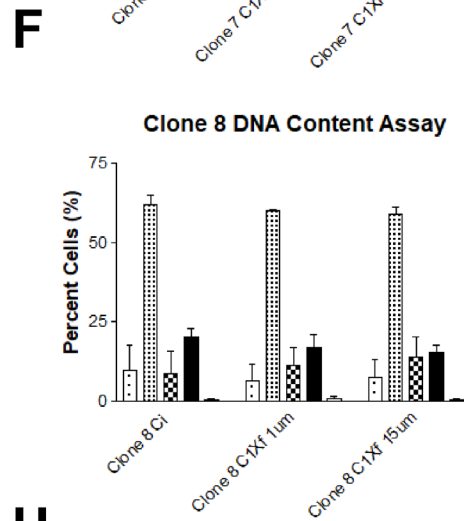
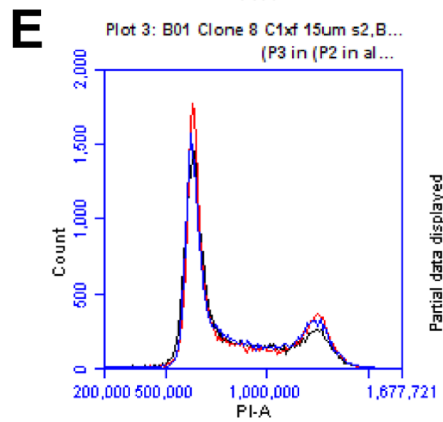
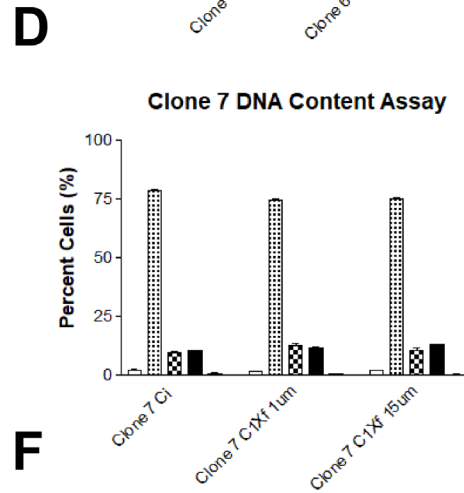
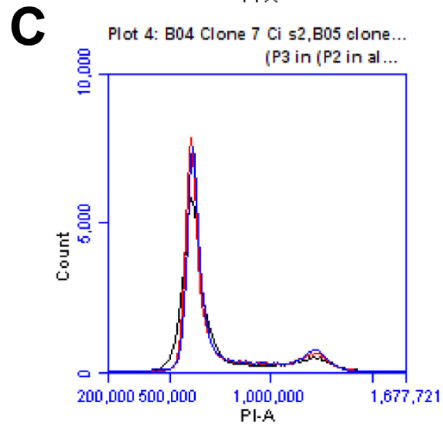
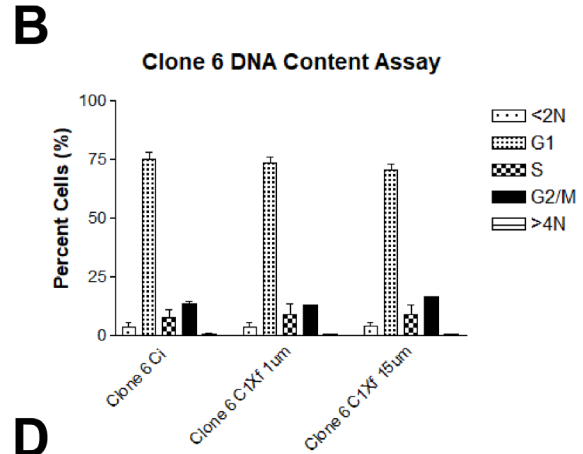
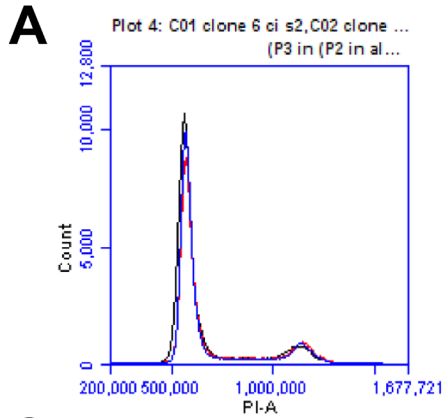


**Figure 6.4: DNA content assay comparing cell cycle following confined and control cell migration through microfluidic devices.** In (A,C,E,G), blue lines represent clonal cell populations that have migrated once through devices with  $1 \times 5 \mu\text{m}^2$  confined constrictions. Red lines represent clonal cell populations that have migrated once through devices with  $15 \times 5 \mu\text{m}^2$  control channels. Black lines indicate original clonal cell populations. PI: propidium iodine fluorescence, count: cell number (A) Representative image of clone 6 cell cycle analysis. (B) Quantified results of cell cycle analysis in clone 6 cell lines. (C) Representative image of clone 7 cell cycle analysis. (D) Quantified results of cell cycle analysis in clone 7 cell lines. (E) Representative image of clone 8 cell cycle analysis. (F) Quantified results of cell cycle analysis in clone 8 cell lines. (G) Representative image of clone 9 cell cycle analysis. (H) Quantified results of cell cycle analysis in clone 6 cell lines. Average of experimental mean  $\pm$  SEM ( $n \geq 100,000$  cells per experiments) by one-way ANOVA with Bonferroni post-hoc test did not reveal any significant differences. Data based on three independent experiments per cell line.

*Double-stranded DNA Damage Marker Gamma-H2A.X Increases Following Confined Migration in Clonal Cell Populations:*

Previous research indicated that nuclear deformation and NE rupture during confined cell migration can induce DNA damage (Denais et al. 2016; Raab et al. 2016). Following a DNA double-stranded break, histone H2A.X is phosphorylated (gamma-H2A.X) to initiate downstream signaling cascades that recruit DNA damage repair

proteins (Francisco and Francisco 2008). Because gamma-H2AX is one of the initial indicators that DNA damage has occurred, we probed for the presence of this phosphorylated protein in our clonal subpopulations following confined and control migration using both immunofluorescence (Fig. 6.5) and flow cytometry (Fig. 6.7).

Our immunofluorescence results revealed increased H2A.X phosphorylation following one round of confined and control migration in in three of the four clones (Fig. 6.5). Specifically, clone 6 and clone 8, which struggled to expand following a second round of selection in the original experiments, showed significant increases in the fluorescent intensity of gamma-H2A.X following confined migration (Fig. 6.6A, C). There was also an increase in gamma-H2A.X fluorescent intensity following control migration in clone 6 when compared to the original clonal population (Fig. 6.6A). Clone 9, which was successful at migrating through both confined and control constrictions multiple times, also displayed a significant increase in gamma-H2A.X fluorescent intensity following confined and control migration compared to its original clonal population (Fig. 6.6D). In contrast, clone 7 did not show any significant differences in gamma-H2A.X levels following confined or unconfined migration (Fig. 6.6C). These differences in fluorescent intensity of gamma-H2A.X following only one round of confined and control migration, illustrate an increase in DNA damage following migration in three out of four clones. Such damage could ultimately cause genomic rearrangements and/or aneuploidy.

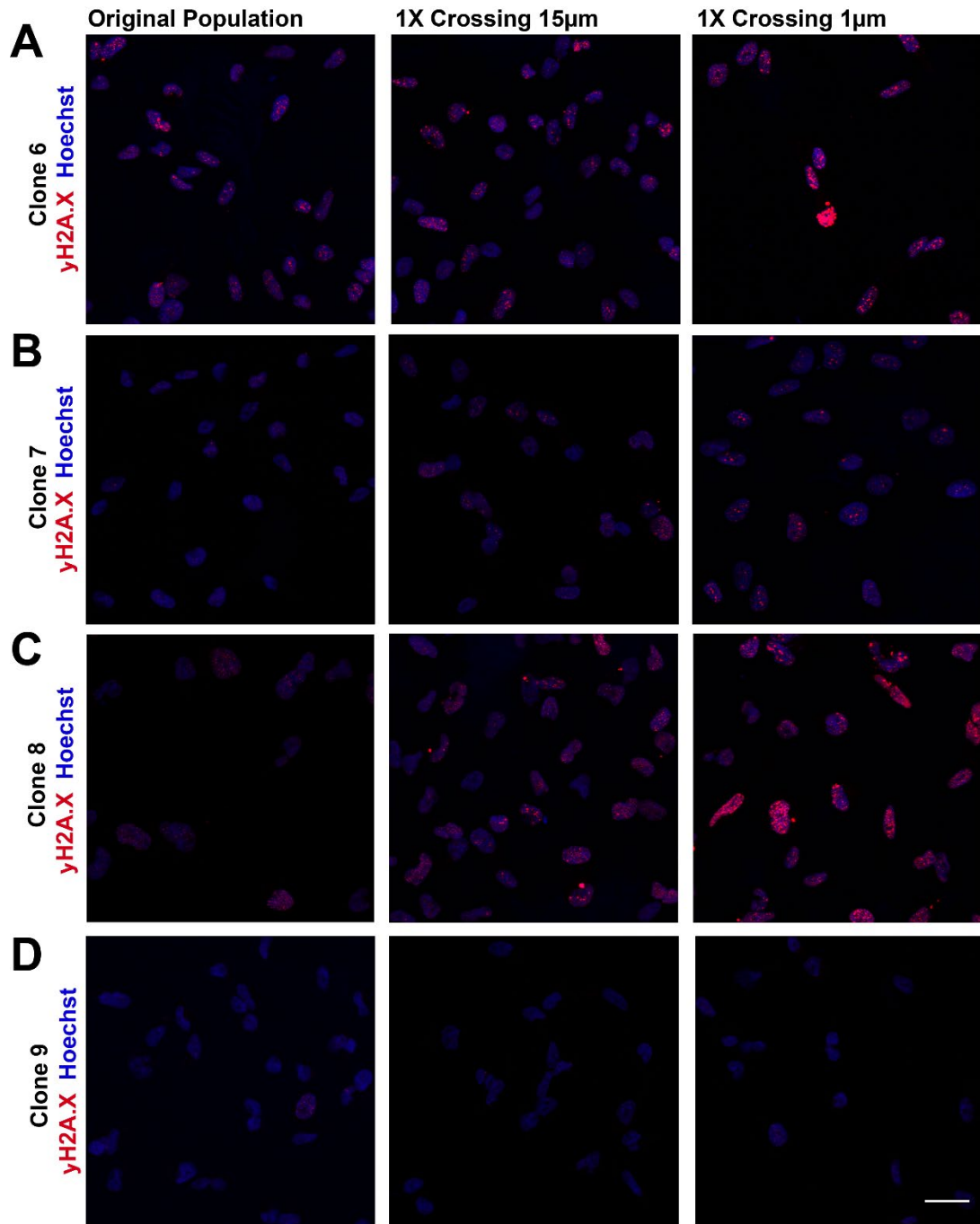


**Figure 6.5: DNA damage following clonal cell selection.** Representative images of clonal cell lines before migration (original population) and after one round of confined

( $1 \times 5 \mu\text{m}^2$ ) and control ( $15 \times 5 \mu\text{m}^2$ ) migration followed by cell expansion for 14 days. Cell DNA (Hoechst) is labeled in blue, and gamma-H2A.X in red. Representative examples of gamma-H2A.X staining in (A) clone 6, (B) clone 7, (C) clone 8, and (D) clone 9 in the original parental population (first panel), following control migration (middle panel) and confined migration (third panel). Scale bar:  $20 \mu\text{m}$ .

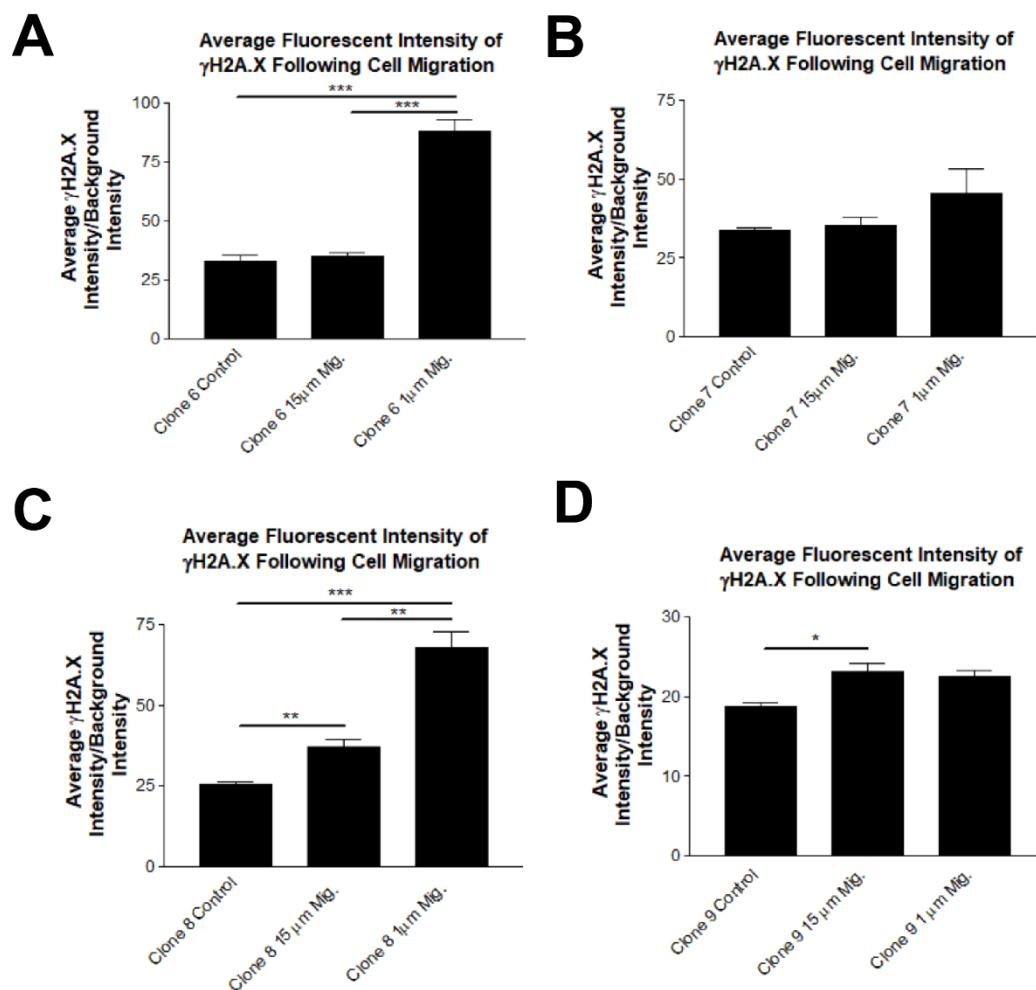


**Figure 6.6: Quantification of DNA damage following clonal cell selection.**

Quantification of gamma-H2A.X fluorescent intensity in clonal cell lines before

migration, and after one round of confined ( $1 \times 5 \mu\text{m}^2$ ) and control ( $15 \times 5 \mu\text{m}^2$ ) migration, followed by cell expansion for 14 days. (A) clone 6, (B) clone 7, (C) clone 8, and (D) clone 9. Data plotted as mean  $\pm$  SEM (\*,  $p < 0.05$ , \*\*,  $p < 0.01$ ; \*\*\*,  $p < 0.001$ ; by one-way ANOVA with Dunn's multiple comparison test;  $n \geq 198$  cells per clonal subpopulation). Data from three independent experiments.

To determine if increased DNA damage was associated with specific phases of the cell cycle or resulted in cell cycle arrest, additional flow cytometer analysis probing for both gamma-H2A.X and propidium iodide was performed (Fig. 6.7). Using cells co-stained with both a DNA content marker and gamma-H2A.X, one can detect rates of DNA damage in cells in G1, S, and G2 phases of the cell cycle. Our results indicate that following confined and control migration, some clones exhibited shifts in the amount of positive gamma-H2A.X in each phase of the cell cycle compared to the original population (Fig. 6.8). In clone 6, cells that migrated through confined and control constrictions were more likely to have cells stain positively for gamma-H2A.X than the control population in each phase of the cell cycle (Fig. 6.8A)—indicating that both confined and control migration increased the levels of DNA damage in all phases of the cell cycle. Surprisingly, in clone 8, cells that had migrated through confined constrictions had lower levels of gamma-H2A.X in G1 than the original population of cells and cells that migrated through control constrictions (Fig. 6.8C). In clone 9, the original population had less gamma-H2A.X positive cells in G1 than the clonal subpopulations that had migrated through confined or control constrictions (Fig. 6.8D).

However, in the S phase of the cell cycle, cells that had migrated through control constrictions had lower levels of gamma-H2A.X than the original population or cells that migrated through confined constrictions. Lastly, in clone 7 there were no obvious shifts in the gamma-H2A.X positive cells between the clonal subpopulations (Fig. 6.8B). This lack of differences follows the immunofluorescence staining results, which found no increase in DNA damage following either confined or control migration for clone 7 (Fig. 6.6B).

As a note of caution, the experiments did not include the appropriate negative (e.g. secondary antibody only) controls, making it difficult to positively identify cells with gamma-H2A.X staining. Future experiments should include these negative controls, as well as positive controls with cells in which DNA damage had been induced.

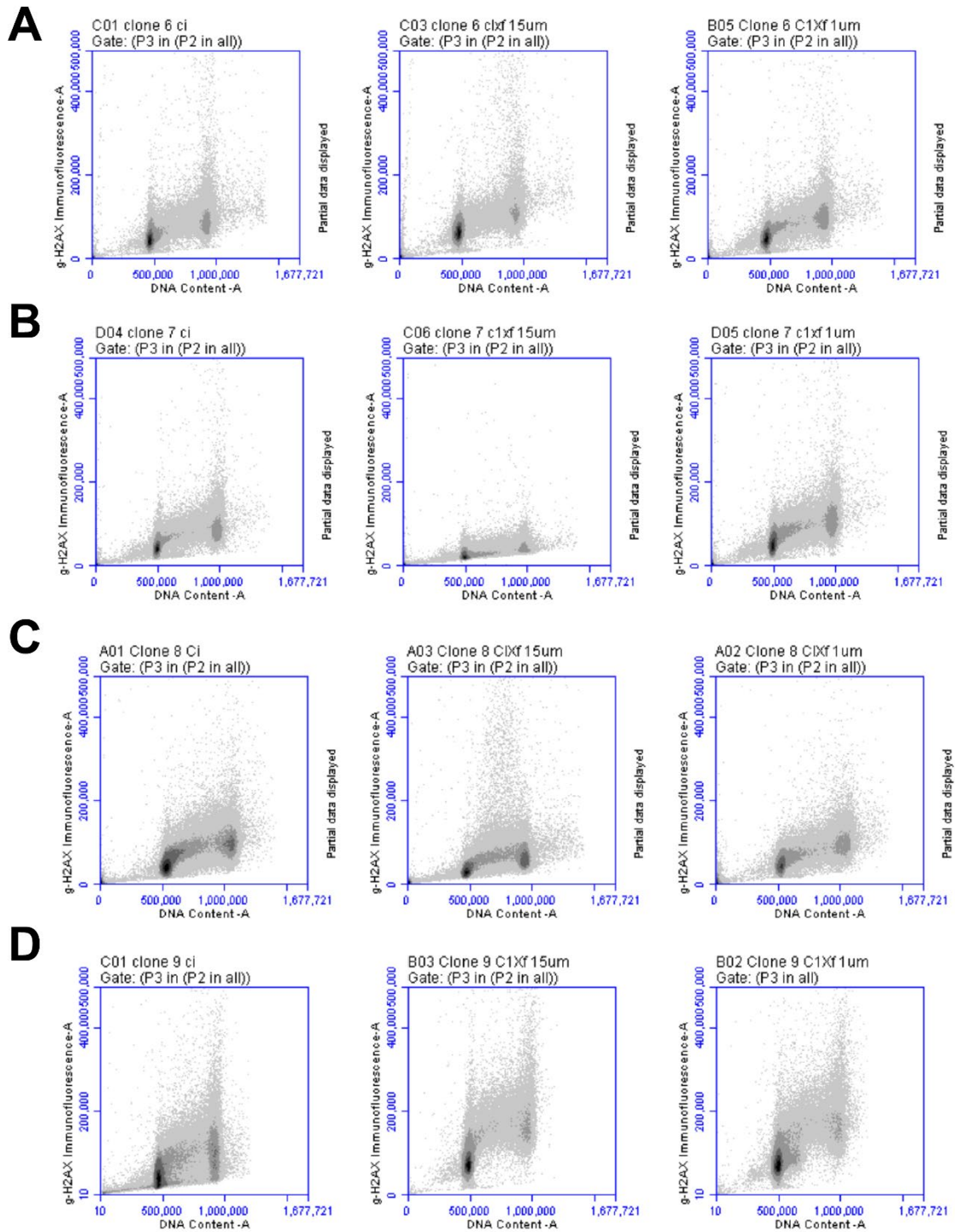


**Figure 6.7: Gamma-H2AX expression across phases of cell cycle in clonal subpopulations.** Representative distribution plots of gamma-H2A.X fluorescent

intensity vs. DNA content in (A) clone 6, (B) clone 7, (C) clone 8, and (D) clone 9. The original parental population is shown in the first panel, following control migration in the middle panel, and confined migration in the third panel. First 100,000 events shown in each plot. Data based on three independent experiments per cell line.

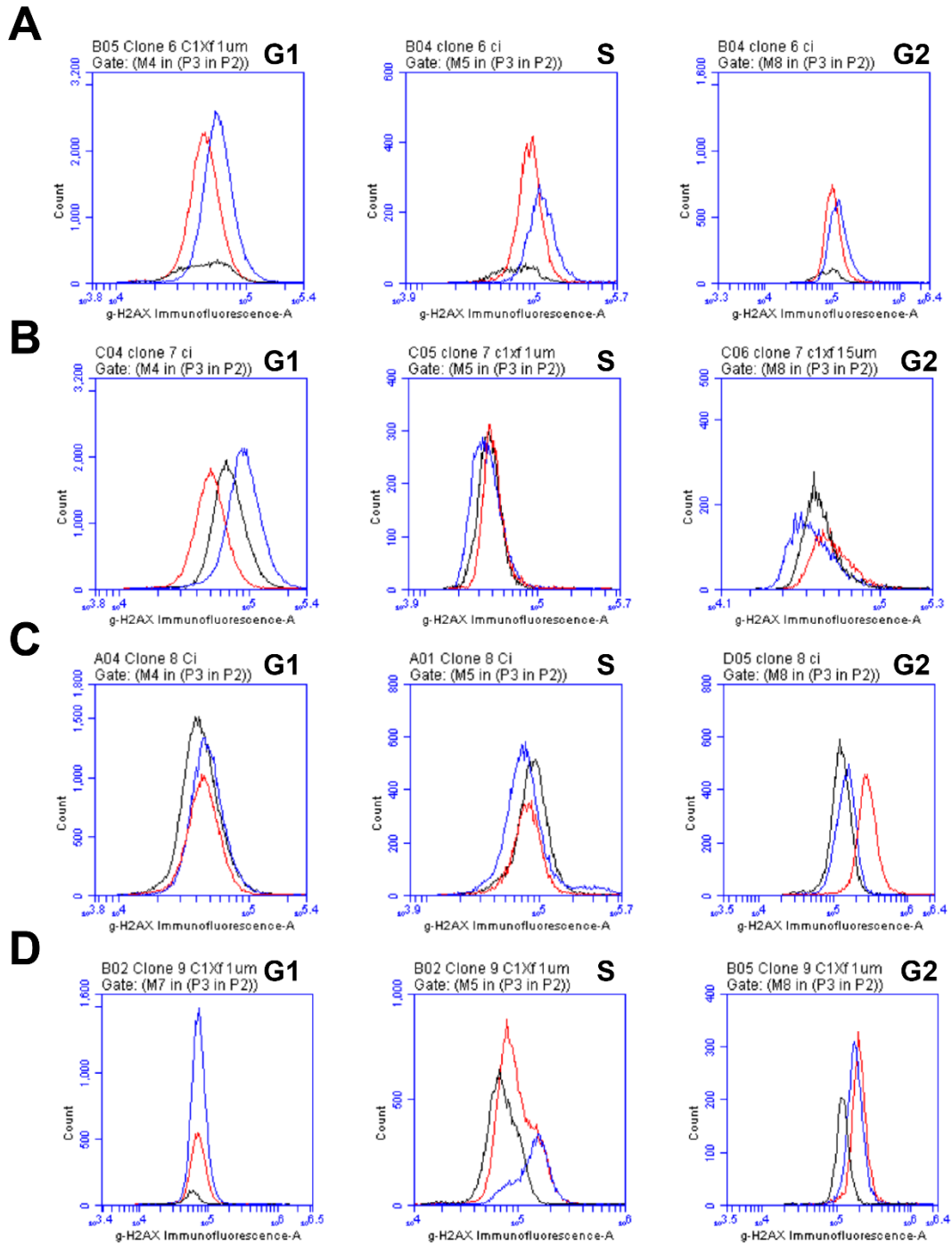


**Figure 6.8: Distribution of gamma-H2A.X expression in different cell cycle phases in clonal subpopulations.** Red lines represent clonal cell populations that have migrated once through devices with  $1 \times 5 \mu\text{m}^2$  confined constrictions. Blue lines

represent clonal cell populations that have migrated once through devices with  $15 \times 5 \mu\text{m}^2$  control constrictions. Black lines indicate original clonal cell populations. (A) Representative images of clone 6 (A), clone 7 (B), clone 8 (C), and (D) clone 9 gamma-H2A.X expression vs. cell count for each phase of the cell cycle (G1, S, and G2).

*2D Scratch Wound Healing did not Vary in Clonal Subpopulations Following Confined Migration:*

Migration through confined and control constrictions is a selective process, in which only the cells capable of migrating across multiple constrictions succeed. Characterization of these migratory cells has shown variation in population doubling time (Table 6.1) and levels of the DNA damage marker gamma-H2A.X (Fig. 6.5 and Fig. 6.6). We performed a 2D scratch wound migration assay to determine if selection of cells for confined migration established a more migratory cell population.

The slope of the scratch wound closure was used to analyze differences in the rate of migration in the 2D scratch wound assay between clones before and after confined and control migration (Table 6.2). The steeper the slope, the more quickly the cells migrated to close the wound. The statistical analysis revealed no significant differences in wound healing rates in clones 6, 7, 8, or 9 following one round of successful migration through confined ( $1 \times 5 \mu\text{m}^2$ ) constrictions (Fig. 6.9). However, in both clone 6 and clone 9, cells that migrated through control ( $15 \times 5 \mu\text{m}^2$ ) constrictions closed the wound significantly slower than the original clonal population (Fig. 6.9A, D).

<b>Rate of Wound Healing (cell density in wound/hours)</b>	<b>Original Clone</b>	<b>Crossed Control 15 <math>\mu</math>m Constrictions</b>	<b>Crossing Confined 1 <math>\mu</math>m Constrictions</b>
Clone 6	1.43 $\pm$ 0.04	1.20 $\pm$ 0.06 *	1.35 $\pm$ 0.05
Clone 7	1.01 $\pm$ 0.03	1.10 $\pm$ 0.04	1.10 $\pm$ 0.03
Clone 8	1.25 $\pm$ 0.04	1.20 $\pm$ 0.04	1.26 $\pm$ 0.04
Clone 9	1.71 $\pm$ 0.10	0.96 $\pm$ 0.05 ***	1.51 $\pm$ 0.09

**Table 6.2: Rate of Wound Healing.** The wound closure rate was determined by calculating the change in cell density within the scratch wound over time. The mean of experimental averages  $\pm$  SEM (\*,  $p < 0.05$ ; \*\*\*,  $p < 0.001$  compared to original clonal population) by one-way ANOVA with Bonferroni's multiple comparison test was used to determine any differences in rate of healing compared to other clone specific subpopulations. Data presented are from at least three independent experiments per cell line.

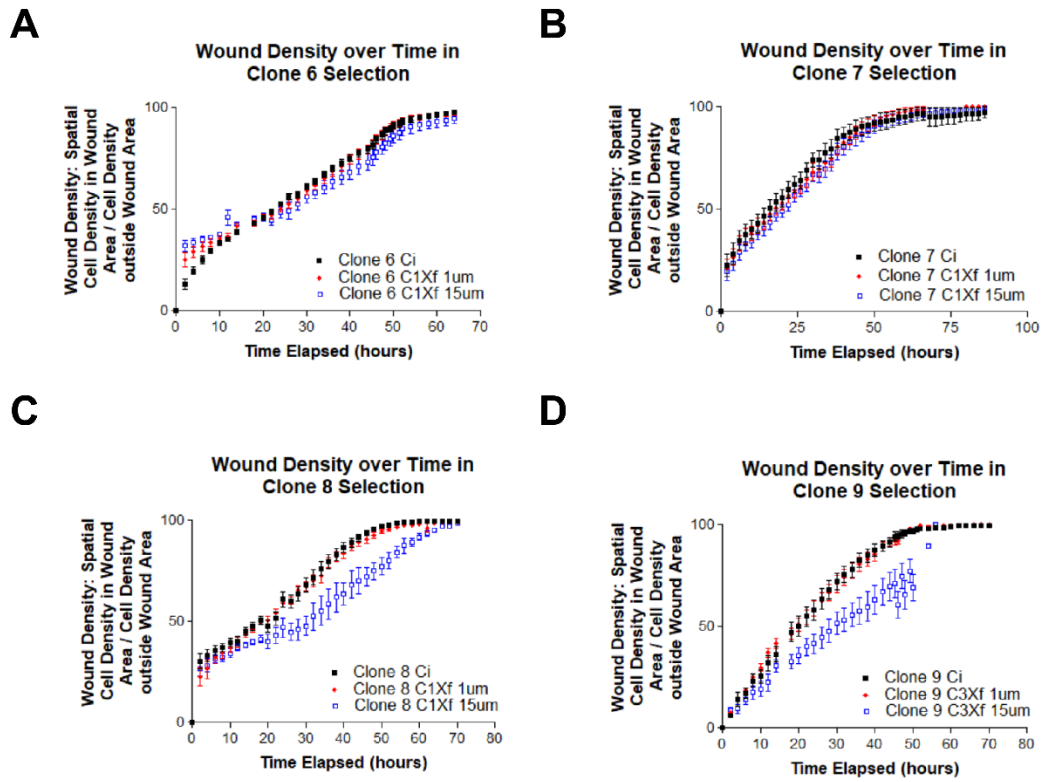


**Figure 6.9: Scratch-wound closure over time (hours).** (A-D) Closure of scratch wound over time (hours) for each individual clonal population. Original parental clones are labeled with black squares. Red diamonds represent clonal cell populations that have migrated through  $1 \times 5 \mu\text{m}^2$  confined constrictions. Unfilled blue squares represent clonal cell populations that have migrated through  $15 \times 5 \mu\text{m}^2$  control constrictions.

## Discussion

Confined cell migration is a high-stress selector of cancer cells that can drive metastatic potential through altered gene expression and changes to the cell cycle (Hanahan and Weinberg 2011). During confined migration, the nuclear stiffness of a cell determines

if a cell nucleus is capable of deforming through a tight space, and is considered a rate-limiting step in cell migration (Davidson et al. 2014; Harada et al. 2014; Wolf et al. 2013). Previous work has shown that the extreme nuclear deformation necessary for successful transit through tight spaces can pose as a substantial mechanical challenge to the integrity of the nucleus, causing NE rupture and nuclear fragmentation (Chapter 2 and 4; Denais et al. 2016; Raab et al. 2016). Both NE rupture and nuclear fragmentation are associated with chromatin herniation, organelle displacement, and DNA damage; however, the long-term consequences of these cell alterations were not yet studied.

Using microfluidic devices containing only confined ( $1 \times 5 \mu\text{m}^2$ ) or control ( $15 \times 5 \mu\text{m}^2$ ) constrictions (Fig. 6.1), we allowed clonal cells to migrate through the constrictions (one to three times), and then characterized the migratory subpopulations compared to the original clonal populations. Although each clonal population originated from the same heterogeneous MDA-MB-231 cell line, and had similar population doubling rates (Table 6.1), each clone responded differently to confined migration. In particular, following the second round of confined cell migration, clones 6 and 8 exhibited stalled cell growth not seen following migration through controlled constrictions or the original clonal populations (Fig. 6.3). In contrast, both clones 7 and 9 migrated through both confined and control constrictions at least twice without any major changes in their ability to proliferate.

Because not all clonal subpopulations were able to expand following more than one round of selection, further characterization was performed using cells that completed only one round of confined and control migration. Although there were differences in population doubling time and average DNA damage intensity in cells following confined and control migration compared to the original populations (Table 6.1 and Fig. 6.6), these differences did not correspond to the arrest in proliferation observed following the second round of confined migration. Specifically, both clone 6 and 8 exhibited significantly more DNA damage following one round of confined migration compared to the original clonal population (Fig. 6.6A, C). However, there were no significant differences in cell cycle distribution (Fig. 6.4A, C). Population doubling times, though significantly different in clone 8, did not slow to the expected rates associated with the stalled cell proliferation seen after two rounds of migration in these clones (Table 6.1).

Characterization of clone 7 and clone 9 following confined and control migration only revealed two distinct effects when compared to the original clonal population—both associated with clone 9 control migration. There was a significantly higher number of cells positive for gamma-H2A.X following control migration when compared to the original population (Fig. 6.6D), and those same cells migrated significantly slower in a 2D scratch wound assay than the original clone 9 population following one round of control cell migration (Table 6.2). Otherwise, there were no significant differences in

cells following confined and control migration when compared to the original population in doubling times, cell cycle dynamics, 2D wound healing, or DNA damage.

Our initial characterization of cells following one round of migration through confined and control constrictions revealed significant increases in the presence of DNA damage in clones 6, 8, and 9 (Fig. 6.5), suggesting that the physical barriers associated with cell migration and nuclear deformation can cause genomic alterations within clonal cell populations. However, our characterization illustrates little alteration in cell proliferation rate (Table 6.1) or cell cycle dynamics (Fig. 6.4) following confined or control migration when compared to the original clonal populations. This suggests that repeated damage, a critical threshold of damage, or the presence of additional mutations must occur in order to observe similar stalled proliferation seen in both clone 6 and clone 8 following a second round of confined cell migration (Fig. 6.3).

Interestingly, cell migration did not improve in the cells selected for confined or control migration compared to the original population. These results may be due to the differences in migration type assayed, i.e., 2D scratch wound vs. 3D migration in the selection experiments), or due to the expansion phase following the selection experiments, during which cells may have lost any selected for advantage.

## **Future Work**

Subtle differences between the clones suggest differences between isogenic subpopulations, such as acquired mutations in DNA damage response or stress response pathways, may be responsible for the differences in behavior between the clones, and future work will be directed to address these differences. To better understand the extent of genetic alteration due to nuclear deformation during confined cell migration, assays such as RNA and single-cell sequencing should be performed. Such assays may reveal differences in protein expression and provide specific detail regarding the type, and prevalence of each mutation. These assays would provide a more complete picture of the differences seen during clonal selection due to confined and control cell migration that cannot be parsed out using current assays. By illustrating more clearly what changes the cell genome is experiencing, one can better understand how the role of the nucleus as a driver for metastatic potential in cancer.

## CHAPTER 7: FROM PATIENTS TO PARTNERS: THE DEVELOPMENT OF A PARTNERSHIP BETWEEN CANCER SURVIVORS AND CANCER SCIENTISTS<sup>5</sup>

When we started graduate school 5 years ago, we were determined to learn everything we could about cancer. We spent all our time in the lab developing an arsenal of experimental techniques. However, in our daily work with Petri dishes and microscopes, we felt that something was missing. We learned all about tumor biology, but we knew very little about the human dimensions of cancer. Even though our research is far from the clinic, we believed that interacting with patients and survivors would improve our understanding of cancer and the quality of our science.

With permission from our advisers, we contacted a local cancer center to see if they might be interested in working with us. The director was enthusiastic about connecting scientists-in-training with the cancer community; in fact, he was already discussing this idea with another group on campus. Together, we started hosting monthly seminars where researchers and patients interact and learn from each other. Some months, a graduate student gives a lay-language presentation about an important aspect of cancer research. Other months, community members describe their experiences of living with cancer. We also organize informal activities that promote patient-researcher dialogue, such as lab tours, book clubs, and participation in cancer support groups. One lung cancer survivor even spent a summer conducting experiments with us. Our relationship with the cancer center created a continuous stream of new opportunities.

---

<sup>5</sup> This work was reproduced from the following publication:

McGregor, A.L. †, DelNero, P.F. †, (2017). From Patients to Partners. *Science* 358(6361), 414.

The partnership with the patient community has deeply influenced our formation as scientists. Our conversations have revealed gaps in our knowledge, exposed biases and assumptions, and even opened new paths for inquiry. We have learned about the hidden costs of cancer and the day-to-day obstacles patients face with their work, health insurance, family life, and plans for the future. We have fostered special relationships with patients and family members, and many have become our closest friends. Occasionally we come face-to-face with the devastating reality that current treatments are not good enough.

The patient-researcher partnership transformed our research from an intellectual exercise into a deeply personal endeavor. It reminds us that people with cancer are not merely cells or molecular pathways. They are neighbors, colleagues, friends, and relatives. They are valued partners in the fight against cancer. As one of our colleagues explained, “I used to care about accomplishments and great publications, but now I simply want to generate data that will be most reliable and important for improving cancer therapy.”

Early in the process, we felt nervous about taking time and energy away from our lab work to develop this program. We felt we were “breaking the rules” for graduate student conduct. But we decided to ignore this nagging anxiety and gave ourselves permission to continue our involvement. With help from a team of faculty members, it eventually turned into a formal curriculum for public engagement in cancer research. This aspect of our work became a highlight of our graduate experience.

Graduate school is a critical part of professional formation, where we begin to formulate the attitudes, priorities, and commitments that ultimately shape our careers. Our graduate training typically emphasizes technical skills and analytical thinking, but the patient-researcher partnership affirms the human aspects of cancer research. By speaking with cancer patients, we have learned to exercise openness, empathy, and reflective listening. The patient perspective gives us a more complete understanding of this disease by providing concrete knowledge of how cancer affects people's lives.

We have also learned that research is not the only way that scientists can make a positive difference in the fight against cancer. Outside of the lab, we can nurture personal relationships with individual patients, survivors, and families. Researchers are well placed to disseminate information, dispel common misconceptions, and share the scientific process with the cancer community. Most importantly, we can be good, supportive listeners. As we pursue the next phase in our research careers, we know that our patient involvement will continue. For us, it has become an integral part of what it means to be a cancer scientist.

## BIBLIOGRAPHY

- Arvold, N. D., Taghian, A. G., Niemierko, A., Abi Raad, R. F., Sreedhara, M., Nguyen, P. L., ... Harris, J. R. (2011). Age, breast cancer subtype approximation, and local recurrence after breast-conserving therapy. *Journal of Clinical Oncology : Official Journal of the American Society of Clinical Oncology*, 29(29), 3885–3891. <https://doi.org/10.1200/JCO.2011.36.1105>
- Aslakson, C. J., Miller, F. R., Simmons, J. L., Asmussen, H., Kamaraju, A. K., Hoenorhoff, M. J., ... Green, J. E. (1992). Selective events in the metastatic process defined by analysis of the sequential dissemination of subpopulations of a mouse mammary tumor. *Cancer Research*, 52(6), 1399–1405. <https://doi.org/10.1158/0008-5472.can-07-6849>
- Badve, S., Dabbs, D. J., Schnitt, S. J., Baehner, F. L., Decker, T., Eusebi, V., ... Lakhani, S. R. (2011). Basal-like and triple-negative breast cancers : a critical review with an emphasis on the implications for pathologists and oncologists, 157–167. <https://doi.org/10.1038/modpathol.2010.200>
- Balzer, E. M., Tong, Z., Paul, C. D., Hung, W. C., Stroka, K. M., Boggs, A. E., ... Konstantopoulos, K. (2012). Physical confinement alters tumor cell adhesion and migration phenotypes. *FASEB Journal*, 26(10), 4045–4056. <https://doi.org/10.1096/fj.12-211441>
- Bell, E. S., & Lammerding, J. (2016). Causes and consequences of nuclear envelope alterations in tumour progression. *European Journal of Cell Biology*, 95(11), 449–464. <https://doi.org/10.1016/j.ejcb.2016.06.007>
- Belt, E. J. T., Fijneman, R. J. A., van den Berg, E. G., Bril, H., Delis-van Diemen, P. M., Tijssen, M., ... Meijer, G. A. (2011). Loss of lamin A/C expression in stage II and III colon cancer is associated with disease recurrence. *European Journal of Cancer*, 47(12), 1837–1845. <https://doi.org/10.1016/j.ejca.2011.04.025>
- Berre, L., Liu, Y.-J., Piel, M., Le Berre, M., Lautenschlaeger, F., Maiuri, P., ... Piel, M. (2015). Confinement and Low Adhesion Induce Fast Amoeboid Migration of Slow Mesenchymal Cells. *Cell*, 160(4), 659–672. <https://doi.org/10.1016/j.cell.2015.01.007>
- Booth-Gauthier, E. a, Du, V., Ghibaud, M., Rape, A. D., Dahl, K. N., & Ladoux, B. (2013). Hutchinson-Gilford progeria syndrome alters nuclear shape and reduces cell

- motility in three dimensional model substrates. *Integrative Biology*, 5(3), 569–577.  
<https://doi.org/10.1039/c3ib20231c>
- Brandes, D., Schofield, B. H., & Anton, E. (1965). Nuclear Mitochondria? *Science*, 149(3690), 1373–1374. Retrieved from  
<http://science.sciencemag.org/content/149/3690/1373.abstract>
- Soule, H. D., Maloney, T. M., Wolman, S. R., Line, E. C., ... Brooks, S. C. (1990). Isolation and Characterization of a Spontaneously Immortalized Isolation and Characterization of a Spontaneously Immortalized Human Breast, 6075–6086.
- Broers, J. L. V., Peeters, E. A. G., Kuijpers, H. J. H., Endert, J., Bouten, C. V. C., Oomens, C. W. J., ... Ramaekers, F. C. S. (2004). Decreased mechanical stiffness in LMNA–/– cells is caused by defective nucleo-cytoskeletal integrity: implications for the development of laminopathies. *Human Molecular Genetics*, 13(21), 2567–2580.  
<https://doi.org/10.1093/hmg/ddh295>
- Bussolati, G., Maletta, F., Asioli, S., Annaratone, L., Sapino, A., & Marchio, C. (2014). Cancer Biology and the Nuclear Envelope. *Adv Exp Med Biol* (773).  
[https://doi.org/10.1007/978-1-4899-8032-8\\_5](https://doi.org/10.1007/978-1-4899-8032-8_5)
- Buxboim, A., Swift, J., Irianto, J., Spinler, K. R., Dingal, P. C. D. P., Athirasala, A., ... Discher, D. E. (2014). Matrix Elasticity Regulates Lamin-A,C Phosphorylation and Turnover with Feedback to Actomyosin. *Current Biology*, 24(16), 1909–1917.  
<https://doi.org/10.1016/j.cub.2014.07.001>
- Capo-chichi, C. D., Aguida, B., Chabi, N. W., Cai, Q. K., Offrin, G., Agossou, V. K., ... Xu, X.-X. (2015). Lamin A/C deficiency is an independent risk factor for cervical cancer. *Cellular Oncology*. <https://doi.org/10.1007/s13402-015-0252-6>
- Capo-chichi, C. D., Cai, K. Q., Smedberg, J., Azar, P. G.-A., Godwin, A. K., & Xu, X.-X. (2011). Loss of A-type lamin expression compromises nuclear envelope integrity in breast cancer. *Chinese Journal of Cancer*, 30(6), 415–425.  
<https://doi.org/10.5732/cjc.010.10566>
- Carey, S. P., Kraning-Rush, C. M., Williams, R. M., & Reinhart-King, C. (2012). Biophysical control of invasive tumor cell behavior by extracellular matrix microarchitecture. *Biomaterials*, 33(16), 4157–4165.  
<https://doi.org/10.1016/j.biomaterials.2012.02.029>
- Carey, S., Starchenko, A., McGregor, A., & Reinhart-King, C. (2013). Leading malignant cells initiate collective epithelial cell invasion in a three-dimensional

- heterotypic tumor spheroid model. *Clin Exp Metastasis*.  
<https://doi.org/10.1007/s10585-013-9565-x>
- Chaffer, C. L., & Weinberg, R. (2011). A perspective on cancer cell metastasis. *Science*, 331(6024), 1559–1564. <https://doi.org/10.1126/science.1203543>
- Chiotaki, R., Polioudaki, H., & Theodoropoulos, P. (2014). Differential nuclear shape dynamics of invasive and non-invasive breast cancer cells are associated with actin cytoskeleton organization and stability, 295(May), 287–295.  
<https://doi.org/10.1139/bcb-2013-0120>
- Chow, K.-H., Factor, R. E., & Ullman, K. S. (2012). The nuclear envelope environment and its cancer connections. *Nature Reviews Cancer*, 12(March).  
<https://doi.org/10.1038/nrc3219>
- Coffinier, C., Chang, S. Y., Nobumori, C., Tu, Y., Farber, E. a, Toth, J. I., ... Young, S. G. (2010). Abnormal development of the cerebral cortex and cerebellum in the setting of lamin B2 deficiency. *Proceedings of the National Academy of Sciences of the United States of America*, 107(11), 5076–5081.  
<https://doi.org/10.1073/pnas.0908790107>
- Cost, A.-L., Ringer, P., Chrostek-Grashoff, A., & Grashoff, C. (2015). How to Measure Molecular Forces in Cells: A Guide to Evaluating Genetically-Encoded FRET-Based Tension Sensors. *Cellular and Molecular Bioengineering*, 8(1), 96–105. <https://doi.org/10.1007/s12195-014-0368-1>
- Dahl, K. N., Engler, A. J., Pajerowski, J. D., & Discher, D. E. (2005). Power-Law Rheology of Isolated Nuclei with Deformation Mapping of Nuclear Substructures. *Biophysical Journal*, 89(4), 2855–2864. <https://doi.org/10.1529/biophysj.105.062554>
- Dahl, K. N., Kahn, S. M., Wilson, K. L., & Discher, D. E. (2004). The nuclear envelope lamina network has elasticity and a compressibility limit suggestive of a molecular shock absorber. *Journal of Cell Science*, 117(Pt 20), 4779–4786.  
<https://doi.org/10.1242/jcs.01357>
- Dai, X., Cheng, H., Bai, Z., & Li, J. (2017). Breast cancer cell line classification and Its relevance with breast tumor subtyping. *Journal of Cancer*, 8(16), 3131–3141.  
<https://doi.org/10.7150/jca.18457>
- Davidson, P. M., Sliz, J., Isermann, P., Denais, C. M., & Lammerding, J. (2015). Design of a microfluidic device to quantify dynamic intra-nuclear deformation

- during cell migration through confining environments. *Integrative Biology*, 30(7), 1534-46. <https://doi.org/10.1039/C5IB00200A>
- Dawson, P. J., Wolman, S. R., Tait, L., Heppner, G. H., & Miller, F. R. (1996). MCF10AT: a model for the evolution of cancer from proliferative breast disease. *The American Journal of Pathology*, 148(1), 313–319.
- De Magistris, P., & Antonin, W. (2018). The Dynamic Nature of the Nuclear Envelope. *Current Biology*, 28(8), R487–R497. <https://doi.org/10.1016/j.cub.2018.01.073>
- Denais, C., & Lammerding, J. (2014). Nuclear mechanics in cancer. *Advances in Experimental Medicine and Biology*, 773, 435–470. [https://doi.org/10.1007/978-1-4899-8032-8\\_20](https://doi.org/10.1007/978-1-4899-8032-8_20)
- Denais, C. M., Gilbert, R. M., Isermann, P., McGregor, A. L., Lindert, M., Weigelin, B., ... Lammerding, J. (2016). Nuclear envelope rupture and repair during cancer cell migration. *Science*, 352(6283), 353-358. <https://doi.org/10.4225/49/56DE29B278684>
- Dexter, D. L., Kowalski, H. M., Blazar, B. A., Fligiel, Z., Vogel, R., & Heppner, G. H. (1978). Heterogeneity of tumor cells from a single mouse mammary tumor. *Cancer Res*, 38(October), 3174–3181.
- Dias, K., Dvorkin-gheva, A., Hallett, R. M., Wu, Y., Hassell, J., Pond, R., ... Bane, A. L. (2017). Claudin-Low Breast Cancer. *Clinical & Pathological Characteristics*, 1–17. <https://doi.org/10.1371/journal.pone.0168669>
- Doerschuk, C. M., Beyers, N., Coxson, H. O., Wiggs, B., & Hogg, J. C. (1993). Comparison of neutrophil and capillary diameters and their relation to neutrophil sequestration in the lung. *Journal of Applied Physiology*, 74(6), 3040–3045.
- Dote, H., Burgan, W. E., Camphausen, K., & Tofilon, P. J. (2006). Inhibition of hsp90 compromises the DNA damage response to radiation. *Cancer Research*, 66(18), 9211–9220. <https://doi.org/10.1158/0008-5472.CAN-06-2181>
- Eissenberg, J. C., & Elgin, S. C. R. (2001). *Heterochromatin and Euchromatin*. John Wiley & Sons, Ltd. <https://doi.org/10.1002/9780470015902.a0001164.pub3>
- Elacqua, J. J., McGregor, A. L., & Lammerding, J. (2018). Automated analysis of cell migration and nuclear envelope rupture in confined environments, *PLoS ONE*, 13(4), e0195664.

- Fan, C., Oh, D. S., Wessels, L., Weigelt, B., Nuyten, D. S. A., Nobel, A. B., ... Perou, C. M. (2006). Concordance among Gene-Expression–Based Predictors for Breast Cancer. *New England Journal of Medicine*, 355(6), 560–569. <https://doi.org/10.1056/NEJMoa052933>
- Ferrera, D., Canale, C., Marotta, R., Mazzaro, N., Gritti, M., Mazzanti, M., ... Gasparini, L. (2014). Lamin B1 overexpression increases nuclear rigidity in autosomal dominant leukodystrophy fibroblasts. *FASEB Journal: Official Publication of the Federation of American Societies for Experimental Biology*, 28(September), 3906–3918. <https://doi.org/10.1096/fj.13-247635>
- Fisher, D. Z., Chaudhary, N., & Blobel, G. (1986). cDNA sequencing of nuclear lamins A and C reveals primary and secondary structural homology to intermediate filament proteins. *Proceedings of the National Academy of Sciences of the United States of America*, 83(17), 6450–6454. <https://doi.org/10.1073/pnas.83.17.6450>
- Francisco, S., & Francisco, S. (2008).  $\gamma$ -H2AX – A Novel Biomarker for DNA Double-strand Breaks, 310, 305–309.
- Friedl, P., & Wolf, K. (2003). Tumour-cell invasion and migration: diversity and escape mechanisms. *Nature Reviews Cancer*, 3(5), 362–374. <https://doi.org/10.1038/nrc1075>
- Friedl, P., Wolf, K., & Lammerding, J. (2011). Nuclear mechanics during cell migration. *Current Opinion in Cell Biology*, 23(1), 55–64. <https://doi.org/10.1016/j.ceb.2010.10.015>
- Fu, Y., Chin, L. K., Bourouina, T., Liu, A. Q., & VanDongen, A. M. J. (2012). Nuclear deformation during breast cancer cell transmigration. *Lab on a Chip*, 12(19), 3774. <https://doi.org/10.1039/c2lc40477j>
- Furukawa, K., Inagaki, H., & Hotta, Y. (1994). Identification and cloning of an mRNA coding for a germ cell-specific A-type lamin in mice. *Experimental Cell Research*, 212(2), 426–430. <https://doi.org/10.1006/excr.1994.1164>
- Gardel, M. L., Schneider, I. C., Aratyn-Schaus, Y., & Waterman, C. M. (2010). Mechanical integration of actin and adhesion dynamics in cell migration. *Annual Review of Cell and Developmental Biology*, 26, 315–333. <https://doi.org/10.1146/annurev.cellbio.011209.122036>
- Greiner, A. M., Jäckel, M., Scheiwe, A. C., Stamow, D. R., Autenrieth, T. J., Lahann, J., ... Bastmeyer, M. (2014). Multifunctional polymer scaffolds with adjustable pore

- size and chemoattractant gradients for studying cell matrix invasion. *Biomaterials*, 35(2), 611–619. <https://doi.org/10.1016/j.biomaterials.2013.09.095>
- Guilluy, C., & Burridge, K. (2015). Nuclear mechanotransduction: Forcing the nucleus to respond. *Nucleus*, 6(1), 19–22. <https://doi.org/10.1080/19491034.2014.1001705>
- Guilluy, C., Osborne, L. D., Van, L. L., Sharek, L., Superfine, R., Garcia-Mata, R., & Burridge, K. (2014). Isolated nuclei adapt to force and reveal a mechanotransduction pathway in the nucleus. *Nature Cell Biology*, 16(1476–4679 (Electronic)), 376–381. <https://doi.org/10.1038/ncb2927>
- Gundersen, G. G., & Worman, H. J. (2013). Nuclear positioning. *Cell*, 152(6), 1376–1389. <https://doi.org/10.1016/j.cell.2013.02.031>
- Guy, C. T., Cardiff, R. D., & Muller, W. J. (1992). Induction of mammary tumors by expression of polyomavirus middle T oncogene: a transgenic mouse model for metastatic disease. *Molecular and Cellular Biology*, 12(3), 954–961. Retrieved from <https://www.ncbi.nlm.nih.gov/pubmed/1312220>
- Guzman, A., Ziperstein, M. J., & Kaufman, L. J. (2014). The effect of fibrillar matrix architecture on tumor cell invasion of physically challenging environments. *Biomaterials*, 35(25), 6954–6963. <https://doi.org/10.1016/j.biomaterials.2014.04.086>
- Haeger, A., Krause, M., Wolf, K., & Friedl, P. (2014). Cell jamming: Collective invasion of mesenchymal tumor cells imposed by tissue confinement. *Biochimica et Biophysica Acta - General Subjects*, 1840(8), 2386–2395. <https://doi.org/10.1016/j.bbagen.2014.03.020>
- Hanahan, D., & Weinberg, R. A. (2011). Hallmarks of cancer: the next generation. *Cell*, 144(5), 646–674. Retrieved from <http://www.ncbi.nlm.nih.gov/pubmed/21376230>
- Harada, T., Swift, J., Irianto, J., Shin, J.-W., Spinler, K. R., Athirasala, A., ... Discher, D. E. (2014). Nuclear lamin stiffness is a barrier to 3D migration, but softness can limit survival. *The Journal of Cell Biology*, 204(5), 669–682. <https://doi.org/10.1083/jcb.201308029>
- Hatch, E. M. (2018). Nuclear envelope rupture: little holes, big openings. *Current Opinion in Cell Biology*, 52, 66–72. <https://doi.org/10.1016/j.ceb.2018.02.001>

- Herschkowitz, J. I., Simin, K., Weigman, V. J., Mikaelian, I., Usary, J., Hu, Z., ... Perou, C. M. (2007). Identification of conserved gene expression features between murine mammary carcinoma models and human breast tumors. *Genome Biology*, 8(5), R76. <https://doi.org/10.1186/gb-2007-8-5-r76>
- Ho, C. Y., & Lammerding, J. (2012). Lamins at a glance. *Journal of Cell Science*, 125(9), 2087–2093. <https://doi.org/10.1242/jcs.087288>
- Howlader, N., Altekruse, S. F., Li, C. I., Chen, V. W., Clarke, C. A., Ries, L. A. G., & Cronin, K. A. (2014). US incidence of breast cancer subtypes defined by joint hormone receptor and HER2 status. *Journal of the National Cancer Institute*, 106(5), dju055. <https://doi.org/10.1093/jnci/dju055>
- Hutchison, C. J. (2014). Do Lamins Influence Disease Progression in Cancer? In *Cancer Biology and the Nuclear Envelope* (1st ed., Vol. 773, pp. 593–604). Springer New York. <https://doi.org/10.1007/978-1-4899-8032-8>
- Ihalainen, T. O., Aires, L., Herzog, F. A., Schwartlander, R., Moeller, J., & Vogel, V. (2015). Differential basal-to-apical accessibility of lamin A/C epitopes in the nuclear lamina regulated by changes in cytoskeletal tension. *Nature Materials*, 14(August). <https://doi.org/10.1038/nmat4389>
- Irianto, J., Pfeifer, C. R., Bennett, R. R., Xia, Y., Ivanovska, I. L., Liu, A. J., ... Discher, D. E. (2016). Nuclear constriction segregates mobile nuclear proteins away from chromatin. *Molecular Biology of the Cell*, 27(25), 4011–4020. <https://doi.org/10.1091/mbc.E16-06-0428>
- Irianto, J., Pfeifer, C. R., Ivanovska, I. L., Swift, J., & Discher, D. E. (2016). Nuclear Lamins in Cancer. *Cellular and Molecular Bioengineering*, 9(2), 258–267. <https://doi.org/10.1007/s12195-016-0437-8>
- Iyer, K. V., Pulford, S., Mogilner, a., & Shivashankar, G. V. (2012). Mechanical activation of cells induces chromatin remodeling preceding MKL nuclear transport. *Biophysical Journal*, 103(7), 1416–1428. <https://doi.org/10.1016/j.bpj.2012.08.041>
- Kaminski, A., Fedorchak, G. R., & Lammerding, J. (2014). The cellular mastermind(?)—mechanotransduction and the nucleus. *Progress in molecular biology and translational science*, 126(1), 157-203. <https://doi.org/10.1016/B978-0-12-394624-9.00007-5>

- Khan, Z. S., Santos, J. M., & Hussain, F. (2018). Aggressive prostate cancer cell nuclei have reduced stiffness. *Biomicrofluidics*, 12(1).  
<https://doi.org/10.1063/1.5019728>
- Khatau, S. B., Bloom, R. J., Bajpai, S., Razafsky, D., Zang, S., Giri, A., ... Wirtz, D. (2012). The distinct roles of the nucleus and nucleus-cytoskeleton connections in three-dimensional cell migration. *Scientific Reports*, 2, 488.  
<https://doi.org/10.1038/srep00488>
- Kohler, B. A., Sherman, R. L., Howlander, N., Jemal, A., Ryerson, A. B., Henry, K. A., ... Penberthy, L. (2015). Annual Report to the Nation on the Status of Cancer, 1975-2011, Featuring Incidence of Breast Cancer Subtypes by Race/Ethnicity, Poverty, and State. *Journal of the National Cancer Institute*, 107(6), djv048-djv048.  
<https://doi.org/10.1093/jnci/djv048>
- Krause, M., & Wolf, K. (2015). Cancer cell migration in 3D tissue: Negotiating space by proteolysis and nuclear deformability. *Cell Adhesion & Migration*, 9(5), 357–366. <https://doi.org/10.1080/19336918.2015.1061173>
- Lammerding, J. (2011). Mechanics of the nucleus. *Comprehensive Physiology*, 1(2), 783–807. <https://doi.org/10.1002/cphy.c100038>
- Lammerding, J., Fong, L. G., Ji, J. Y., Reue, K., Stewart, C. L., Young, S. G., & Lee, R. T. (2006). Lamins a and C but not lamin B1 regulate nuclear mechanics. *Journal of Biological Chemistry*, 281(35), 25768–25780.  
<https://doi.org/10.1074/jbc.M513511200>
- Lammerding, J., Schulze, P. C., Takahashi, T., Kozlov, S., Sullivan, T., Kamm, R. D., ... Lee, R. T. (2004). Lamin A/C deficiency causes defective nuclear mechanics and mechanotransduction. *Journal of Clinical Investigation*, 113(3), 370–378.  
<https://doi.org/10.1172/JCI200419670>
- Lautscham, L. A., Kämmerer, C., Lange, J. R., Kolb, T., Mark, C., Schilling, A., ... Fabry, B. (2015). Migration in Confined 3D Environments Is Determined by a Combination of Adhesiveness, Nuclear Volume, Contractility, and Cell Stiffness. *Biophysical Journal*, 109(5), 900–913. <https://doi.org/10.1016/j.bpj.2015.07.025>
- Le Berre, M., Aubertin, J., & Piel, M. (2012). Fine control of nuclear confinement identifies a threshold deformation leading to lamina rupture and induction of specific genes. *Integrative Biology*, 4(11), 1406–1414. <https://doi.org/10.1039/C2IB20056B>

- Li, Y., Chu, J. S., Kurpinski, K., Li, X., Bautista, D. M., Yang, L., ... Li, S. (2011). Biophysical regulation of histone acetylation in mesenchymal stem cells. *Biophysical Journal*, 100(8), 1902–1909. <https://doi.org/10.1016/j.bpj.2011.03.008>
- Lim, S., Quinton, R. J., Ganem, N. J., & Bement, W. (2016). Nuclear envelope rupture drives genome instability in cancer. <https://doi.org/10.1091/mbc.E16-02-0098>
- Lin, E. Y., Jones, J. G., Li, P., Zhu, L., Whitney, K. D., Muller, W. J., & Pollard, J. W. (2003). Progression to malignancy in the polyoma middle T oncoprotein mouse breast cancer model provides a reliable model for human diseases. *The American Journal of Pathology*, 163(5), 2113–2126. [https://doi.org/10.1016/S0002-9440\(10\)63568-7](https://doi.org/10.1016/S0002-9440(10)63568-7)
- Lin, F., & Worman, H. J. (1993). Structural organization of the human gene encoding nuclear lamin A and nuclear lamin C. *The Journal of Biological Chemistry*, 268(22), 16321–16326. <https://doi.org/10.1006/geno.1995.1036>
- Lin, F., & Worman, H. J. (1995). Structural organization of the human gene (LMNB1) encoding nuclear lamin B1. *Genomics*, 27(2), 230–236. <https://doi.org/10.1006/geno.1995.1036>
- Liu, Y.-J., Le Berre, M., Lautenschlaeger, F., Maiuri, P., Callan-Jones, A., Heuzé, M., ... Piel, M. (2015). Confinement and Low Adhesion Induce Fast Amoeboid Migration of Slow Mesenchymal Cells. *Cell*, 160(4), 659–672. <https://doi.org/10.1016/j.cell.2015.01.007>
- Machiels, B. M., Zorenc, A. H. G., Endert, J. M., Kuijpers, H. J. H., Van Eys, G., Ramaekers, F. C. S., & Broers, J. L. V. (1996). An alternative splicing product of the lamin A/C gene lacks exon 10. *Journal of Biological Chemistry*, 271(16), 9249–9253. <https://doi.org/10.1074/jbc.271.16.9249>
- Mak, M., Reinhart-King, C. & Erickson, D. (2013). Elucidating mechanical transition effects of invading cancer cells with a subnucleus-scaled microfluidic serial dimensional modulation device. *Lab on a Chip*, 13(3), 340–348. <https://doi.org/10.1039/c2lc41117b>
- Malboubi, M., Jayo, A., Parsons, M., & Charras, G. (2015). An open access microfluidic device for the study of the physical limits of cancer cell deformation during migration in confined environments. *Microelectronic Engineering*, 144, 42–45. <https://doi.org/10.1016/j.mee.2015.02.022>

- Manohar, S., Harlow, M., Nguyen, H., Li, J., Hankins, G. R., & Park, M. (2011). Chromatin modifying protein 1A (Chmp1A) of the endosomal sorting complex required for transport (ESCRT)-III family activates ataxia telangiectasia mutated (ATM) for PanC-1 cell growth inhibition. *Cell Cycle*, 10(15), 2529–2539. <https://doi.org/10.4161/cc.10.15.15926>
- Martins, R. P., Finan, J. D., Guilak, F., & Lee, D. a. (2012). Mechanical regulation of nuclear structure and function. *Annual Review of Biomedical Engineering*, 14, 431–455. <https://doi.org/10.1146/annurev-bioeng-071910-124638>
- Matsumoto, A., Hieda, M., Yokoyama, Y., Nishioka, Y., Yoshidome, K., Tsujimoto, M., & Matsuura, N. (2015). Global loss of a nuclear lamina component, lamin A/C, and LINC complex components SUN1, SUN2, and nesprin-2 in breast cancer. *Cancer Medicine*. <https://doi.org/10.1002/cam4.495>
- Mayr, M., Hu, Y. H., Hainaut, P., & Xu, Q. B. (2002). Mechanical stress-induced DNA damage and rac-p38MAPK signal pathways mediate p53-dependent apoptosis in vascular smooth muscle cells. *Faseb Journal*, 16(9), 1423–+. <https://doi.org/10.1096/Fj.02-0042fje>.
- McGregor, A. L., Hsia, C.-R., & Lammerding, J. (2016). Squish and squeeze—the nucleus as a physical barrier during migration in confined environments. *Current Opinion in Cell Biology*, 40, 32–40. <https://doi.org/10.1016/j.ceb.2016.01.011>
- McGuire, A., Lowery, A. J., Kell, M. R., Kerin, M. J., & Sweeney, K. J. (2017). Locoregional Recurrence Following Breast Cancer Surgery in the Trastuzumab Era: A Systematic Review by Subtype. *Annals of Surgical Oncology*, 24(11), 3124–3132. <https://doi.org/10.1245/s10434-017-6021-1>
- McKeon, F. D., Kirschner, M. W., & Caput, D. (1986). Homologies in both primary and secondary structure between nuclear envelope and intermediate filament proteins. *Nature*, 319(6053), 463–468. <https://doi.org/10.1038/319463a0>
- Mekhdjian, A. H., Kai, F., Rubashkin, M. G., Prah, L. S., Przybyla, L. M., McGregor, A. L., ... Weaver, V. M. (2017). Integrin-mediated traction force enhances paxillin molecular associations and adhesion dynamics that increase the invasiveness of tumor cells into a three-dimensional extracellular matrix. *Molecular Biology of the Cell*, 28(11), 1467–1488. <https://doi.org/10.1091/mbc.E16-09-0654>
- Metzger-Filho, O., Sun, Z., Viale, G., Price, K. N., Crivellari, D., Snyder, R. D., ... Cardoso, F. (2013). Patterns of Recurrence and outcome according to breast cancer subtypes in lymph node-negative disease: results from international breast cancer

- study group trials VIII and IX. *Journal of Clinical Oncology : Official Journal of the American Society of Clinical Oncology*, 31(25), 3083–3090.  
<https://doi.org/10.1200/JCO.2012.46.1574>
- Mitchell, M. J., Denais, C., Chan, M. F., Wang, Z., Lammerding, J., & King, M. R. (2015). Lamin A/C deficiency reduces circulating tumor cell resistance to fluid shear stress. *American Journal of Physiology - Cell Physiology*, 309(11), C736–C746.
- Moss, S. F., Krivosheyev, V., de Souza, A., Chin, K., Gaetz, H. P., Chaudhary, N., ... Holt, P. R. (1999). Decreased and aberrant nuclear lamin expression in gastrointestinal tract neoplasms. *Gut*, 45(5), 723–729.  
<https://doi.org/10.1136/gut.45.5.723>
- Munjal, A., & Lecuit, T. (2014). Actomyosin networks and tissue morphogenesis. *Development (Cambridge, England)*, 141(9), 1789–1793.  
<https://doi.org/10.1242/dev.091645>
- Nabeshima, K., Inoue, T., Shimao, Y., & Sameshima, T. (2002). Matrix metalloproteinases in tumor invasion: role for cell migration. *Pathology International*, 52(4), 255–264. Retrieved from  
<http://www.ncbi.nlm.nih.gov/pubmed/12031080>
- Pajerowski, J. D., Dahl, K. N., Zhong, F. L., Sammak, P. J., & Discher, D. E. (2007). Physical plasticity of the nucleus in stem cell differentiation. *Proceedings of the National Academy of Sciences of the United States of America*, 104(40), 15619–15624. <https://doi.org/10.1073/pnas.0702576104>
- Partridge, A. H., Hughes, M. E., Warner, E. T., Ottesen, R. A., Wong, Y.-N., Edge, S. B., ... Tamimi, R. M. (2016). Subtype-Dependent Relationship Between Young Age at Diagnosis and Breast Cancer Survival. *Journal of Clinical Oncology*, 34(27), 3308–3314. <https://doi.org/10.1200/JCO.2015.65.8013>
- Paszek, M. J., Zahir, N., Johnson, K. R., Lakins, J. N., Rozenberg, G. I., Gefen, A., ... Weaver, V. M. (2005). Tensional homeostasis and the malignant phenotype, 8(September), 241–254. <https://doi.org/10.1016/j.ccr.2005.08.010>
- Peter, M., Kitten, G. T., Lehner, C. F., Vorburger, K., Bailer, S. M., Maridor, G., & Nigg, E. a. (1989). Cloning and sequencing of cDNA clones encoding chicken lamins A and B1 and comparison of the primary structures of vertebrate A- and B-type lamins. *Journal of Molecular Biology*, 208, 393–404.  
[https://doi.org/10.1016/0022-2836\(89\)90504-4](https://doi.org/10.1016/0022-2836(89)90504-4)

- Petrie, R. J., Koo, H., & Yamada, K. M. (2014). Generation of compartmentalized pressure by a nuclear piston governs cell motility in a 3D matrix. *Science*, 345(6200), 1062–1065. <https://doi.org/10.1126/science.1256965>
- Petrie, R. J., & Yamada, K. M. (2015). Fibroblasts Lead the Way: A Unified View of 3D Cell Motility. *Trends in Cell Biology*, xx(x), 1–9. <https://doi.org/10.1016/j.tcb.2015.07.013>
- Poh, Y.-C., Shevtsov, S. P., Chowdhury, F., Wu, D. C., Na, S., Dunder, M., & Wang, N. (2012). Dynamic force-induced direct dissociation of protein complexes in a nuclear body in living cells. *Nature Communications*, 3(May), 866. <https://doi.org/10.1038/ncomms1873>
- Poste, G., & Fidler, I. J. (1980). The pathogenesis of cancer metastasis. *Nature*, 283(5743), 139–146.
- Raab, M., Gentili, M., De Belly, H., Thiam, H. R., Vargas, P., Jimenez, A. J., ... Piel, M. (2016). ESCRT III repairs nuclear envelope ruptures during cell migration to limit DNA damage and cell death. *Science*, 352(6283), 359–362. <https://doi.org/10.1126/science.aad7611>
- Rowat, A. C., Jaalouk, D. E., Zwerger, M., Ung, W. L., Eydelnant, I. A., Olins, D. E., ... Lammerding, J. (2013). Nuclear Envelope Composition Determines the Ability of Neutrophil-type Cells to Passage through Micron-scale Constrictions. *Journal of Biological Chemistry*, 288(12), 8610–8618. <https://doi.org/10.1074/jbc.M112.441535>
- Sansregret, L., Vanhaesebroeck, B., & Swanton, C. (2018). Determinants and clinical implications of chromosomal instability in cancer. *Nature Reviews Clinical Oncology*, 15(3), 139–150. <https://doi.org/10.1038/nrclinonc.2017.198>
- Santner, S. J., Dawson, P. J., Tait, L., Soule, H. D., Eliason, J., Mohamed, A. N., ... Miller, F. R. (2001). Malignant MCF10CA1 cell lines derived from premalignant human breast epithelial MCF10AT cells, 101–110.
- Schäpe, J., Prausse, S., Radmacher, M., & Stick, R. (2009). Influence of lamin A on the mechanical properties of amphibian oocyte nuclei measured by atomic force microscopy. *Biophysical Journal*, 96(10), 4319–4325. <https://doi.org/10.1016/j.bpj.2009.02.048>

- Schindelin, J., Arganda-Carreras, I., Frise, E., Kaynig, V., Longair, M., Pietzsch, T., ... Cardona, A. (2012). Fiji: an open-source platform for biological-image analysis. *Nature Methods*, 9(7), 676–682. <https://doi.org/10.1038/nmeth.2019>
- Schreiber, K. H., & Kennedy, B. K. (2013). When Lamins Go Bad: Nuclear Structure and Disease. *Cell*, 152(6), 1365–1375. <https://doi.org/10.1016/j.cell.2013.02.015>
- National Cancer Institute (2018). Cancer Stat Facts: Female Breast Cancer. Surveillance, Epidemiology, and End Results Program (SEER) 18 2008-2014, All Races, Females by SEER Summary Stage. <https://seer.cancer.gov/statfacts/html/breast.html>
- Shah, P., Wolf, K., & Lammerding, J. (2017). Bursting the Bubble: Nuclear Envelope Rupture as a Path to Genomic Instability? *Trends in Cell Biology*, 27(8), 546–555. <https://doi.org/10.1016/j.tcb.2017.02.008>
- Shimi, T., Kittisopikul, M., Tran, J., Goldman, A. E., Adam, S. A., Zheng, Y., ... Goldman, R. D. (2015). Structural organization of nuclear lamins A, C, B1, and B2 revealed by superresolution microscopy. *Molecular Biology of the Cell*, 26(22), 4075–4086. <https://doi.org/10.1091/mbc.E15-07-0461>
- Shimi, T., Pflieger, K., Kojima, S., Pack, C.-G., Solovei, I., Goldman, A. E., ... Goldman, R. D. (2008). The A- and B-type nuclear lamin networks: microdomains involved in chromatin organization and transcription. *Genes & Development*, 22(24), 3409–3421. <https://doi.org/10.1101/gad.1735208>
- Sineshaw, H. M., Gaudet, M., Ward, E. M., Flanders, W. D., Desantis, C., Lin, C. C., & Jemal, A. (2014). Association of race/ethnicity, socioeconomic status, and breast cancer subtypes in the National Cancer Data Base (2010--2011). *Breast Cancer Research and Treatment*, 145(3), 753–763. <https://doi.org/10.1007/s10549-014-2976-9>
- Solovei, I., Wang, A. S., Thanisch, K., Schmidt, C. S., Krebs, S., Zwerger, M., ... Joffe, B. (2013). LBR and lamin A/C sequentially tether peripheral heterochromatin and inversely regulate differentiation. *Cell*, 152(3), 584–598. <https://doi.org/10.1016/j.cell.2013.01.009>
- Sosa, B. a., Rothballer, A., Kutay, U., & Schwartz, T. U. (2012). LINC complexes form by binding of three KASH peptides to domain interfaces of trimeric SUN proteins. *Cell*, 149(5), 1035–1047. <https://doi.org/10.1016/j.cell.2012.03.046>

- Stephens, A. D., Banigan, E. J., Adam, S. A., Goldman, R. D., & Dunn, A. R. (2017). Chromatin and lamin A determine two different mechanical response regimes of the cell nucleus. <https://doi.org/10.1091/mbc.E16-09-0653>
- Stetler-Stevenson, W. G., Aznavoorian, S., & Liotta, L. A. (1993). Tumor cell interactions with the extracellular matrix during invasion and metastasis. *Annual Review of Cell Biology*, 9, 541–573. <https://doi.org/10.1146/annurev.cb.09.110193.002545>
- Stoitzner, P., Pfaller, K., Stössel, H., & Romani, N. (2002). A close-up view of migrating Langerhans cells in the skin. *Journal of Investigative Dermatology*, 118(1), 117–125. <https://doi.org/10.1046/j.0022-202x.2001.01631.x>
- Swift, J., Irianto, J., Shin, J. W., Spinler, K. R., Athirasala, A., ... Discher, D. E. (2014). Nuclear lamin stiffness is a barrier to 3D migration, but softness can limit survival. *Journal of Cell Biology*, 204(5), 669–682. <https://doi.org/10.1083/jcb.201308029>
- Swift, J., Ivanovska, I. L., Buxboim, A., Harada, T., Dingal, P. C. D. P., Pinter, J., ... Discher, D. E. (2013). Nuclear lamin-A scales with tissue stiffness and enhances matrix-directed differentiation. *Science (New York, N.Y.)*, 341(6149), 1240104. <https://doi.org/10.1126/science.1240104>
- Takaki, T., Montagner, M., Serres, M. P., Le Berre, M., Russell, M., Collinson, L., ... Petronczki, M. (2017). Actomyosin drives cancer cell nuclear dysmorphia and threatens genome stability. *Nature Communications*, 8, 16013. Retrieved from <https://doi.org/10.1038/ncomms16013>
- Takamasa Harada, 1 Joe Swift, 1 Jerome Irianto, 1 Jae-Won Shin, 1 Kyle R. Spinler, 1 Avathamsa Athirasala, 1 Rocky Diegmiller, 1 P.C. Dave P. Dingal, 1 Irena L. Ivanovska, 1 and Dennis E. Discher<sup>1, 2</sup>. (2014). Nuclear lamin stiffness is a barrier to 3D migration, but softness can limit survival. *The Journal of Cell Biology*, 204(5), 626–626. <https://doi.org/10.1083/jcb.2045iti2>
- Thomas, D. G., Yenepalli, A., Denais, C. M., Rape, A., Beach, J. R., Wang, Y., ... Egelhoff, T. T. (2015). Non-muscle myosin IIB is critical for nuclear translocation during 3D invasion, 1–12. <https://doi.org/10.1083/jcb.201502039>
- Tong, Z., Balzer, E. M., Dallas, M. R., Hung, W. C., Stebe, K. J., & Konstantopoulos, K. (2012). Chemotaxis of cell populations through confined spaces at Single-Cell resolution. *PLoS ONE*, 7(1), 1–10. <https://doi.org/10.1371/journal.pone.0029211>

- Uhlen, M., Zhang, C., Lee, S., Sjöstedt, E., Fagerberg, L., Bidkhori, G., ... Ponten, F. (2017). A pathology atlas of the human cancer transcriptome. *Science*, 357(6352), eaan2507. <https://doi.org/10.1126/science.aan2507>
- Vargas, J. D., Hatch, E. M., Anderson, D. J., & Hetzer, M. W. (2012). Transient nuclear envelope rupturing during interphase in human cancer cells. *Nucleus*, 3(1), 88–100.
- Voduc, K. D., Cheang, M. C. U., Tyldesley, S., Gelmon, K., Nielsen, T. O., & Kennecke, H. (2010). Breast Cancer Subtypes and the Risk of Local and Regional Relapse. *Journal of Clinical Oncology*, 28(10), 1684–1691. <https://doi.org/10.1200/JCO.2009.24.9284>
- Vorburger, K., Lehner, C. F., Kitten, G. T., Eppenberger, H. M., & Nigg, E. A. (1989). A second higher vertebrate B-type lamin. cDNA sequence determination and in vitro processing of chicken lamin B2. *Journal of Molecular Biology*, 208(3), 405–415. [https://doi.org/10.1016/0022-2836\(89\)90505-6](https://doi.org/10.1016/0022-2836(89)90505-6)
- Walker, P. R., Kwast-Welfeld, J., Gourdeau, H., Leblanc, J., Neugebauer, W., & Sikorska, M. (1993). Relationship between Apoptosis and the Cell Cycle in Lymphocytes: Roles of Protein Kinase C, Tyrosine Phosphorylation, and AP1. *Experimental Cell Research*, (207), 142–151.
- Wazir, U., Ahmed, M., Bridger, J., Harvey, A., Jiang, W., Sharma, A., & Mokbel, K. (2013). The clinicopathological significance of lamin A/C, lamin B1 and lamin B receptor mRNA expression in human breast cancer. *Cellular and Molecular Biology Letters*, 18(4). <https://doi.org/10.2478/s11658-013-0109-9>
- Weigelin, B., Bakker, G.-J., & Friedl, P. (2012). Intravital third harmonic generation microscopy of collective melanoma cell invasion. *IntraVital*, 1(1), 32–43. <https://doi.org/10.4161/intv.21223>
- Weninger, W., Biro, M., & Jain, R. (2014). Leukocyte migration in the interstitial space of non-lymphoid organs. *Nature Reviews. Immunology*, 14(4), 232–246. <https://doi.org/10.1038/nri3641>
- Willis, N. D., Cox, T. R., Rahman-Casañs, S. F., Smits, K., Przyborski, S. A., van den Brandt, P., ... Hutchison, C. J. (2008). Lamin A/C is a risk biomarker in colorectal cancer. *PloS One*, 3(8), e2988. <https://doi.org/10.1371/journal.pone.0002988>
- Wolf, K., Mazo, I., Leung, H., Engelke, K., Von Andrian, U. H., Deryugina, E. I., ... Friedl, P. (2003). Compensation mechanism in tumor cell migration: Mesenchymal-

- amoeboid transition after blocking of pericellular proteolysis. *Journal of Cell Biology*, 160(2), 267–277. <https://doi.org/10.1083/jcb.200209006>
- Wolf, K., Lindert, M., Krause, M., Alexander, S., Riet, J., Willis, A. L., ... Friedl, P. (2013). Physical limits of cell migration: Control by ECM space and nuclear deformation and tuning by proteolysis and traction force. *Journal of Cell Biology*, 201(7), 1069–1084. <https://doi.org/10.1083/jcb.201210152>
- Yang, H., Liu, J., Lin, J., Deng, L., Fan, S., Guo, Y., ... Hua, W. (2016). Overexpression of CHMP7 from rapeseed and *Arabidopsis* causes dwarfism and premature senescence in *Arabidopsis*. *Journal of Plant Physiology*, 204, 16–26. <https://doi.org/10.1016/j.jplph.2016.06.023>
- Young, S. G., Jung, H.-J., Lee, J. M., & Fong, L. G. (2014). Nuclear Lamins and Neurobiology. *Molecular and Cellular Biology*, 34(15), 2776–2785. <https://doi.org/10.1128/MCB.00486-14>

APPENDIX:

*pQCXIP-NLS-copGFP-P2A-H2B-tdTomato-puro Plasmid Sequence*

AAAAAGCTTACTGGCTTAACTATGCGGCATCAGAGCAGATTGTAAGTACTGAGAGTGCA  
CCATATGCGGTGTGAAATACCGCACAGATGCGTAAGGAGAAAATACCGCATCAG  
GCGCTCTTCCGCTTCCTCGCTCACTGACTCGCTGCGCTCGGTCGTTCCGGCTGCGGC  
GAGCGGTATCAGCTCACTCAAAGGCGGTAATACGGTTATCCACAGAATCAGGGGA  
TAACGCAGGAAAGAACATGTGAGCAAAAGGCCAGCAAAAGGCCAGGAACCGTAA  
AAAGGCCGCGTTGCTGGCGTTTTTCCATAGGCTCCGCCCCCTGACGAGCATCAC  
AAAATCGACGCTCAAGTCAGAGGTGGCGAAACCCGACAGGACTATAAAGATAC  
CAGGCGTTTCCCCCTGGAAGCTCCCTCGTGCGCTCTCCTGTTCCGACCCTGCCGCT  
TACCGGATACCTGTCCGCCTTTCTCCCTTCGGGAAGCGTGGCGCTTTCTCATAGCT  
CACGCTGTAGGTATCTCAGTTCGGTGTAGGTCGTTTCGCTCCAAGCTGGGCTGTGTG  
CACGAACCCCCGTTTCAGCCCGACCGCTGCGCCTTATCCGGTAACTATCGTCTTGA  
GTCCAACCCGTAAGACACGACTTATCGCCACTGGCAGCAGCCACTGGTAACAGG  
ATTAGCAGAGCGAGGTATGTAGGCGGTGCTACAGAGTTCTTGAAGTGGTGGCCTA  
ACTACGGCTACACTAGAAGGACAGTATTTGGTATCTGCGCTCTGCTGAAGCCAGT  
TACCTTCGGAAAAAGAGTTGGTAGCTCTTGATCCGGCAAACAAACCACCGCTGGT  
AGCGGTGGTTTTTTTTGTTTGCAAGCAGCAGATTACGCGCAGAAAAAAGGATCTC  
AAGAAGATCCTTTGATCTTTTCTACGGGTCTGACGCTCAGTGGAACGAAAATC  
ACGTTAAGGGATTTTGGTCATGAGATTATCAAAAAGGATCTTCACCTAGATCCTTT  
TAAATTAATAAATGAAGTTTTAAATCAATCTAAAGTATATATGAGTAACTTGGTC  
TGACAGTTACCAATGCTTAATCAGTGAGGCACCTATCTCAGCGATCTGTCTATTC

GTTTCATCCATAGTTGCCTGACTCCCCGTCGTGTAGATAACTACGATACGGGAGGG  
CTTACCATCTGGCCCCAGTGCTGCAATGATACCGCGAGACCCACGCTCACCGGCT  
CCAGATTTATCAGCAATAAACCAGCCAGCCGGAAGGGCCGAGCGCAGAAGTGGT  
CCTGCAACTTTATCCGCCTCCATCCAGTCTATTAATTGTTGCCGGGAAGCTAGAGT  
AAGTAGTTCGCCAGTTAATAGTTTGCGCAACGTTGTTGCCATTGCTGCAGGCATCG  
TGGTGTACGCTCGTCGTTTGGTATGGCTTCATTCAGCTCCGGTTCCCAACGATCA  
AGGGCAGTTACATGATCCCCATGTTGTGCAAAAAGCGGTTAGCTCCTTCGGTC  
CTCCGATCGTTGTCAGAAGTAAGTTGGCCGCAGTGTTATCACTCATGGTTATGGCA  
GCACTGCATAATTCTTACTGTCATGCCATCCGTAAGATGCTTTTCTGTGACTGG  
TGAGTACTCAACCAAGTCATTCTGAGAATAGTGTATGCGGCGACCGAGTTGCTCT  
TGCCCGGCGTCAACACGGGATAATACCGCGCCACATAGCAGAACTTTAAAAGTGC  
TCATCATTGGAAAACGTTCTTCGGGGCGAAAACCTCTCAAGGATCTTACCGCTGTTG  
AGATCCAGTTCGATGTAACCCACTCGTGCACCCAACCTGATCTTCAGCATCTTTTAC  
TTTACCAGCGTTTCTGGGTGAGCAAAAACAGGAAGGCAAAATGCCGCAAAAAA  
GGGAATAAGGGCGACACGGAAATGTTGAATACTCATACTCTTCCTTTTTCAATATT  
ATTGAAGCATTATCAGGGTTATTGTCTCATGAGCGGATACATATTTGAATGTATT  
TAGAAAAATAAACAAATAGGGGTTCCGCGCACATTTCCCCGAAAAGTGCCACCTG  
ACGTCTAAGAAACCATTATTATCATGACATTAACCTATAAAAATAGGCGTATCAC  
GAGGCCCTTTCGTCTTCAAGAATTAGCTTGGCCATTGCATACGTTGTATCCATATC  
ATAATATGTACATTTATATTGGCTCATGTCCAACATTACCGCCATGTTGACATTGA  
TTATTGACTAGTTATTAATAGTAATCAATTACGGGGTCATTAGTTCATAGCCCATA  
TATGGAGTTCCGCGTTACATAACTTACGGTAAATGGCCCGCCTGGCTGACCGCCC  
AACGACCCCCGCCATTGACGTCAATAATGACGTATGTTCCCATAGTAACGCCAA  
TAGGGACTTTCCATTGACGTCAATGGGTGGAGTATTTACGGTAAACTGCCCACTTG  
GCAGTACATCAAGTGTATCATATGCCAAGTACGCCCCCTATTGACGTCAATGACG

GTAAATGGCCCGCCTGGCATTATGCCAGTACATGACCTTATGGGACTTTCCTACT  
TGGCAGTACATCTACGTATTAGTCATCGCTATTACCATGGTGATGCGGTTTTGGCA  
GTACATCAATGGGCGTGGATAGCGGTTTGACTCACGGGGATTTCCAAGTCTCCAC  
CCCATTGACGTCAATGGGAGTTTGTGTTTGGCACAAAATCAACGGGACTTTCCAA  
AATGTCGTAACAACCTCCGCCCCATTGACGCAAATGGGCGGTAGGCGTGACGGTG  
GGAGGTCTATATAAGCAGAGCTCAATAAAAGAGCCCACAACCCCTCACTCGGCGC  
GCCAGTCTTCCGATAGACTGCGTCGCCCCGGGTACCCGTATTCCAATAAAGCCTCT  
TGCTGTTTGCATCCGAATCGTGGTCTCGCTGTTTCTTGGGAGGGTCTCCTCTGAGT  
GATTGACTACCCACGACGGGGTCTTTCATTTGGGGGCTCGTCCGGGATTTGGAG  
ACCCCTGCCAGGGACCACCGACCCACCACCGGGAGGTAAGCTGGCCAGCAACTT  
ATCTGTGTCTGTCCGATTGTCTAGTGTCTATGTTTGATGTTATGCGCCTGCGTCTGT  
ACTAGTTAGCTAACTAGCTCTGTATCTGGCGGACCCGTGGTGGAACTGACGAGTT  
CTGAACACCCGGCCGCAACCCTGGGAGACGTCCCAGGGACTTTGGGGGCGTTTTT  
TGTGGCCCGACCTGAGGAAGGGAGTCGATGTGGAATCCGACCCCGTCAGGATATG  
TGGTTCTGGTAGGAGACGAGAACCTAAAACAGTTCCCGCCTCCGTCTGAATTTTTG  
CTTTCGGTTTTGGAACCGAAGCCGCGCGTCTTGTCTGCTGCAGCGCTGCAGCATCGT  
TCTGTGTTGTCTCTGTCTGACTGTGTTTCTGTATTTGTCTGAAAATTAGGGCCAGAC  
TGTTACCACTCCCTTAAGTTTGACCTTAGGTCACTGGAAAGATGTCGAGCGGATCG  
CTCACAACCAGTCGGTAGATGTCAAGAAGAGACGTTGGGTTACCTTCTGCTCTGC  
AGAATGGCCAACCTTTAACGTCGGATGGCCGCGAGACGGCACCTTTAACCGAGAC  
CTCATCACCCAGGTTAAGATCAAGGTCTTTTCACCTGGCCCGCATGGACACCCAG  
ACCAGGTCCCCTACATCGTGACCTGGGAAGCCTTGGCTTTTGACCCCCCTCCCTGG  
GTCAAGCCCTTTGTACACCCTAAGCCTCCGCCTCCTCTTCCCTCCATCCGCCCCGTCT  
CTCCCCCTTGAACCTCCTCGTTCGACCCCGCCTCGATCCTCCCTTTATCCAGCCCTC  
ACTCCTTCTCTAGGCGCCGGAATTGAAGATCTGGGGGATCGATCCTCTAGAGTCC

GTTACATAACTTACGGTAAATGGCCCGCCTGGCTGACCGCCCAACGACCCCCGCC  
CATTGACGTCAATAATGACGTATGTTCCCATAGTAACGCCAATAGGGACTTTCAT  
TGACGTCAATGGGTGGAGTATTTACGGTAAACTGCCCACTTGGCAGTACATCAAG  
TGTATCATATGCCAAGTACGCCCCCTATTGACGTCAATGACGGTAAATGGCCCGC  
CTGGCATTATGCCCAGTACATGACCTTATGGGACTTTCCTACTTGGCAGTACATCT  
ACGTATTAGTCATCGCTATTACCATGGTGATGCGGTTTTGGCAGTACATCAATGGG  
CGTGAATAGCGGTTTGACTCACGGGGATTTCCAAGTCTCCACCCCATGACGTCA  
ATGGGAGTTTGTGGTGGCACAAAATCAACGGGACTTTCAAAATGTCGTAACAA  
CTCCGCCCCATTGACGCAAATGGGCGGTAGGCGTGTACGGTGGGAGGTCTATATA  
AGCAGAGCTCGTTTAGTGAACCGTCAGATCGCCTGGAGACGCCATCCACGCTGTT  
TTGACCTCCATAGAAGACACCGGGACCGATCCAGCTCCGCGGCCGGGAACGGTG  
CATTGGAACGCTGCAGGAATTGATCCGCGGCCGCACCATGACTGCTCCAAAGAAG  
AAGCGTAAGGTTCCCGGGTGTGTGCAAGAGAGCGACGAGAGCGGCCTGCCCGCC  
ATGGAGATCGAGTGCCGCATCACCGGCACCCTGAACGGCGTGGAGTTCGAGCTGG  
TGGGCGGCGGAGAGGGCACCCCCAAGCAGGGCCGCATGACCAACAAGATGAAGA  
GCACCAAAGGCGCCCTGACCTTCAGCCCCTACCTGCTGAGCCACGTGATGGGCTA  
CGGCTTCTACCACTTCGGCACCTACCCAGCGGCTACGAGAACCCTTCCTGCACG  
CCATCAACAACGGCGGCTACACCAACACCCGCATCGAGAAGTACGAGGACGGCG  
GCGTGCTGCACGTGAGCTTCAGCTACCGCTACGAGGCCGGCCGCGTGATCGGGCA  
CTTCAAGGTGGTGGGCACCGGCTTCCCCGAGGACAGCGTGATCTTCACCGACAAG  
ATCATCCGCAGCAACGCCACCGTGGAGCACCTGCACCCCATGGGCGATAACGTGC  
TGGTGGGCAGCTTCGCCCGCACCTTCAGCCTGCGCGACGGCGGCTACTACAGCTT  
CGTGGTGGACAGCCACATGCACTTCAAGAGCGCCATCCACCCAGCATCCTGCAG  
AACGGGGGCCCATGTTCGCCTTCCGCCGCGTGGAGGAGCTGCACAGCAACACCG  
AGCTGGGCATCGTGGAGTACCAGCACGCCTTCAAGACCCCATCGCCTTCGCCAG

ATCCCGCGCTCAGTCGTCCAATTCTGCCGTGGACGGCACCGCCGGA C C C G G T C C  
ACCGGATCTCGCACCGGTGGAAGCGGAGCTACTAACTTCAGCCTGCTGAAGCAGG  
CTGGAGACGTGGAGGAGAACCCTGGACCT CCTGAACCCTCTAAGTCTGCTCCAGC  
CCCTAAAAAGGGTTCTAAGAAGGCTATCACTAAGGCGCAGAAGAAGGATGGTAA  
GAAGCGTAAGCGCAGCCGCAAGGAGAGCTATTCTATCTATGTGTACAAGGTTCTG  
AAGCAGGTCCACCCCGACACCGGCATCT CATCCAAGGCCATGGGGATCATGAACT  
CCTTCGTCAACGACATCTTCGAGCGCATCGCGGGCGAGGCTTCTCGCCTGGCTCAC  
TACAATAAGCGCTCGACCATCACCTCCAGGGAGATTCAGACGGCTGTGCGCCTGC  
TGCTGCCTGGGGAGCTGGCTAAGCATGCTGTGTCCGAGGGCACTAAGGCAGTTAC  
CAAGTACACTAGCTCTTTAATTAAGGGAAGCGGAGGCGGATCCA TGGTGAGCAAG  
GGCGAGGAGGTCATCAAAGAGTTCATGCGCTTCAAGGTGCGCATGGAGGGCTCCA  
TGAACGGCCACGAGTTCGAGATCGAGGGCGAGGGCGAGGGCCGCCCTACGAGG  
GCACCCAGACCGCCAAGCTGAAGGTGACCAAGGGCGGCCCCCTGCCCTTCGCTG  
GGACATCCTGTCCCCCAGTTCATGTACGGCTCCAAGGCGTACGTGAAGCACCCC  
GCCGACATCCCCGATTACAAGAAGCTGTCCTTCCCCGAGGGCTTCAAGTGGGAGC  
GCGTGATGAACTTCGAGGACGGCGGTCTGGTGACCGTGACCCAGGACTCCTCCCT  
GCAGGACGGCACGCTGATCTACAAGGTGAAGATGCGCGGCACCAACTTCCCCCC  
GACGGCCCCGTAATGCAGAAGAAGACCATGGGCTGGGAGGCCTCCACCGAGCGC  
CTGTACCCCCGCGACGGCGTGCTGAAGGGCGAGATCCACCAGGCCCTGAAGCTGA  
AGGACGGCGGCCACTACCTGGTGGAGTTCAAGACCATCTACATGGCCAAGAAGCC  
CGTGCAACTGCCCGGCTACTACTACGTGGACACCAAGCTGGACATCACCTCCAC  
AACGAGGACTACACCATCGTGGAACAGTACGAGCGCTCCGAGGGCCGCCACCAC  
CTGTTCCCTGGGGCATGGCACCGGCAGCACCGGCAGCGGCAGCTCCGGCACCGCCT  
CCTCCGAGGACAACAACATGGCCGTCACTCAAAGAGTTCATGCGCTTCAAGGTGGC  
CATGGAGGGCTCCATGAACGGCCACGAGTTCGAGATCGAGGGCGAGGGCGAGGG

CCGCCCCTACGAGGGCACCAGACCGCCAAGCTGAAGGTGACCAAGGGCGGCC  
CCTGCCCTTCGCCTGGGACATCCTGTCCCCCAGTTCATGTACGGCTCCAAGGCGT  
ACGTGAAGCACCCCGCCGACATCCCCGATTACAAGAAGCTGTCCTTCCCCGAGGG  
CTTCAAGTGGGAGCGCGTGATGAACTTCGAGGACGGCGGTCTGGTGACCGTGACC  
CAGGACTCCTCCCTGCAGGACGGCACGCTGATCTACAAGGTGAAGATGCGCGGCA  
CCAACTTCCCCCGACGGCCCCGTAATGCAGAAGAAGACCATGGGCTGGGAGGC  
CTCCACCGAGCGCCTGTACCCCCGCGACGGCGTGCTGAAGGGCGAGATCCACCAG  
GCCCTGAAGCTGAAGGACGGCGGCCACTACCTGGTGGAGTTCAAGACCATCTACA  
TGGCCAAGAAGCCCGTGCAACTGCCCGGCTACTACTACGTGGACACCAAGCTGGA  
CATCACCTCCCACAACGAGGACTACACCATCGTGGAACAGTACGAGCGCTCCGAG  
GGCCGCCACCACCTGTTCCCTGTACGGCATGGACGAGCTGTACAAGGAGAACGCAA  
ACAGCTAAGAATTCCGCCCCTCTCCCTCCCCCCCCCTAACGTTACTGGCCGAAGC  
CGCTTGAATAAGGCCGGTGTGCGTTTGTCTATATGTTATTTCCACCATATTGCC  
GTCTTTTGGCAATGTGAGGGCCCGGAAACCTGGCCCTGTCTTCTTGACGAGCATTC  
CTAGGGGTCTTTCCCCTCTCGCCAAAGGAATGCAAGGTCTGTTGAATGTCGTGAA  
GGAAGCAGTTCCTCTGGAAGCTTCTTGAAGACAAACAACGTCTGTAGCGACCCTT  
TGCAGGCAGCGGAACCCCCACCTGGCGACAGGTGCCTCTGCGGCCAAAAGCCAC  
GTGTATAAGATACACCTGCAAAGGCGGCACAACCCAGTGCCACGTTGTGAGTTG  
GATAGTTGTGGAAAGAGTCAAATGGCTCTCCTCAAGCGTATTCAACAAGGGGCTG  
AAGGATGCCCAGAAGGTACCCCATTTGTATGGGATCTGATCTGGGGCCTCGGTGCA  
CATGCTTTACATGTGTTTAGTCGAGGTTAAAAAACGTCTAGGCCCCCCGAACCAC  
GGGGACGTGGTTTTCTTTGAAAAACACGATGATAAGCTTGCCACAACCCACAAG  
GAGACGACCTTCATGACCGAGTACAAGCCACGGTGCGCCTCGCCACCCGCGAC  
GACGTCCCCGGGCCGTACGCACCCTCGCCGCCGCGTTCGCCGACTACCCGCCA  
CGCGCCACACCGTCGACCCGGACCGCCACATCGAGCGGGTCACCGAGCTGCAAG

AACTCTTCCTCACGCGCGTCGGGCTCGACATCGGCAAGGTGTGGGTTCGCGGACGA  
CGGCGCCGCGGTGGCGGTCTGGACCACGCCGGAGAGCGTCGAAGCGGGGGCGGT  
GTTCGCCGAGATCGGCCCGCGCATGGCCGAGTTGAGCGGTTCCCGGCTGGCCGCG  
CAGCAACAGATGGAAGGCCTCCTGGCGCCGCACCGGCCCAAGGAGCCCGCGTGG  
TTCCTGGCCACCGTCGGCGTCTCGCCCGACCACCAGGGCAAGGGTCTGGGCAGCG  
CCGTCGTGCTCCCCGGAGTGGAGGCGGCCGAGCGCGCCGGGGTGCCCGCCTTCCT  
GGAGACCTCCGCGCCCCGCAACCTCCCCTTCTACGAGCGGCTCGGCTTCACCGTC  
ACCGCCGACGTCGAGTGCCCGAAGGACCGCGCGACCTGGTGCATGACCCGCAAG  
CCCGGTGCCTGACGCCCCGCCACGACCCGCAGCGCCCGACCGAAAGGAGCGCA  
CGACCCCATGGCTCCGACCGAAGCCGACCCGGGCGGCCCGCCGACCCCGCACCC  
GCCCCGAGGCCACCGACTCTAGTCGAGGGCTGCAGCGCTGCAGAGGCCGAGTG  
CAGAACTGCTCCAAAGGGACCTCAAGGCTTTCCGAGGGACACTAGGCTGACTCCA  
TCGAGCCAGTGTAGAGATAAGCTTATCGATTAGTCCAATTTGTAAAGACAGGAT  
ATCAGTGGTCCAGGCTCTAGTTTTGACTCAACAATATCACCAGCTGAAGCCTATA  
GAGTACGAGCCATAGATAAAAATAAAAGATTTTTATTTAGTCTCCAGAAAAAGGGGG  
GAATGAAAGACCCACCTGTAGGTTTGGCAAGCTAGCTTAAGTAACGCCATTTTG  
CAAGGCATGGAAAAATACATAACTGAGAATAGAGAAGTTCAGATCAAGGTCAGG  
AACAGATGGAACAGGGTCGACCCTAGAGAACCATCAGATGTTTCCAGGGTGCCCC  
AAGGACCTGAAATGACCCTGTGCCTTATTTGAACTAACCAATCAGTTCGCTTCTCG  
CTTCTGTTCGCGCGCTTCTGCTCCCCGAGCTCAATAAAAAGAGCCCACAACCCCTCA  
CTCGGGGCGCCAGTCCTCCGATTGACTGAGTCGCCCGGGTACCCGTGTATCCAAT  
AAACCCTCTTGAGTTGCATCCGACTTGTGGTCTCGCTGTTCTTGGGAGGGTCTC  
CTCTGAGTGATTGACTACCCGTCAGCGGGGGTCTTTCATTTGGGGGCTCGTCCGGG  
ATCGGGAGACCCCTGCCAGGGACCACCGACCCACCACCGGGAGGTAAGCTGGC  
TGCCTCGCGCGTTTTCGGTGATGACGGTGAAAACCTCTGACACATGCAGCTCCCGG

AGACGGTCACAGCTTGTCTGTAAGCGGATGCCGGGAGCAGACAAGCCCGTCAGG  
GCCGTCAGCGGGTGTGGCGGGTGTGGGGCGCAGCCATGACCCAGTCACGTAG  
CGATAGCGGAGTGTAGATCCGGCTGTGGAATGTGTGTCAGTTAGGGTGTGGAAAG  
TCCCAGGCTCCCAGCAGGCAGAAGTATGCAAAGCATGCATCTCAATTAGTCAG  
CAACCAGGTGTGGAAAGTCCCAGGCTCCCAGCAGGCAGAAGTATGCAAAGCA  
TGCATCTCAATTAGTCAGCAACCATAGTCCCGCCCCTAACTCCGCCCATCCCGCCC  
CTAACTCCGCCAGTTCCGCCATTCTCCGCCCATGGCTGACTAATTTTTTTTATT  
TATGCAGAGGCCGAGGCCGCCTCGGCCTCTGAGCTATTCCAGAAGTAGTGAGGAG  
GCTTTTTTGGAGGCCTAGGCTTTTGC

README file for running Automated Analysis Program

*Download program at the following URL: <https://github.com/Lammerding/>*

*MATLAB-Cell Tracking.*

In order to read \*.czi files, the Bio-Formats MATLAB Toolbox must be downloaded from the Open Microscopy Environment website (<https://www.openmicroscopy.org/bio-formats/>) and added to the MATLAB search path.

*Instructions for example data:*

1. Run the "AutomatedMigrationAnalyzer2.m" script in MATLAB.
2. Select "MDA-MD-468 NLS-copGFP H2B-tdTomato 0to10FBS 2umConstrictions 10minPerImage.czi" from the file explorer GUI

3. Select a folder to save the results to. For the example, "...\Program Example\" is a good location.
4. Choose to analyze every position of a migration device or a subset of positions. The example file has only one position.
5. Enter the constriction sizes of the migration device positions being analyzed. For this example, the size is 2 (microns).
6. Select in which direction cells migrate. In the example, cells migrate from bottom to top.
7. Select the order of the fluorescent channels being used. In this example, H2B-tdTomato is in the first channel, so enter 1, and NLS-copGFP is in the second channel, so enter 2. The order of the channels can be viewed by opening the .czi file in Zen.
8. Wait a few seconds for the program to automatically rotate the image sequence and locate the constrictions.
9. Verify the constriction location worked properly.
10. Wait for the program to analyze the image sequence.
11. Run "MigrationAnalysisVerification2.m"
12. Navigate to the folder that was chosen when running AutomatedMigrationAnalyzer2.m and select the newly created folder containing the migration tracking results.
13. Select the migration device position to begin verifying the tracking results. The example has only one position, so choose 1.

14. Fix any tracking errors if necessary (see below). The provided example should not contain any tracking errors.
15. Close the window with the tracking results to save data on constriction transit and nuclear envelope rupture duration.
16. View the results saved in the \*.csv files.

*Visual verification of tracking results:*

To scroll through the video of the tracked nuclei, use the scroll bar at the bottom of the window, the mouse wheel, or the arrow keys. Errors can be fixed by clicking on individual nuclei. Use the right mouse button to start or cancel rupture events. Left click two different cells or the same cell twice to fix other errors.